KfK 4566
März 1989

The Quantitative Microstructure-Field Property Correlation of Multiphase and Porous Materials

G. Ondracek
Institut für Material- und Festkörperforschung

Kernforschungszentrum Karlsruhe

KERNFORSCHUNGSZENTRUM KARLSRUHE

Institut für Material- und Festkörperforschung

KfK 4566

The Quantitative Microstructure-Field Property Correlation of Multiphase and Porous Materials

G. Ondracek *

*jetzt: Institut für Gesteinshüttenkunde
Rheinisch-Westfälische Technische Hochschule
Aachen

Kernforschungszentrum Karlsruhe GmbH, Karlsruhe

VOL. 3, Nos. 3–4 1987

REVIEWS ON

POWDER METALLURGY AND PHYSICAL CERAMICS

TABLE OF CONTENTS

The Quantitative Microstructure-Field Property Correlation of Multiphase and Porous Materials

Gerhard Ondracek
Rheinisch-Westfälische Technische Hochschule Aachen
and
Kernforschungszentrum Karlsruhe
Mauerstr. 5
D - 5100 Aachen

CONTENTS

ABSTRACT

The treatment of the microstructure-property interrelationship in the literature either provides empirical or semiempirical correlations, which cannot be generalized for practical use, or - being theoretically rigorous solutions - do not meet the needs with respect to an engineering approach and use by its formulations and theoretically limiting conditions. To overcome this gap from an engineering point of view is the deliberate objective of this presentation. Proceeding from expressions given in the literature for the theoretical relationship between microstructure and field properties according to the bound and model concepts, field property bound equations as well as microstructure-field property equations are derived in the first part of this article, enabling the field properties of two-phase materials to be calculated from their microstructural data. To satisfy the demand of maximum reliability from a theoretical as well as practical point of view no fitting parameters are allowed to appear in these equations. - The determination of microstructural parameters such as the number of phases, the type of microstructure as well as the concentration, shape and orientation factors by quantitative microstructural analysis is described in the second part, whilst calculated and measured electrical and thermal conductivities of two-phase metals, ceramics and composites as well as porous materials are compared in the final part.

1. Introduction: Definition and Premises

The following presentation refers to what has been published already as an introductory review concerning the problem [205] but leads into the detail of the correlation between microstructure and field properties. -

According to Fig. 1 the structure of materials may be subdivided into 4 groups, the sequence of which is characterized by increasing linear dimensions. The subject of these considerations will be the interrelationship between the microstructure of multiphase materials and their field properties, where the term "multiphase materials" is understood as set out in Fig. 2. As a special case porous materials are considered to be composed of - at least - one solid phase and a gaseous phase ($\doteq$ pores).

The properties of multiphase materials depend on the properties of their phases as well as on the geometry and geometrical arrangement of these phases within the material, i.e. on its microstructure.

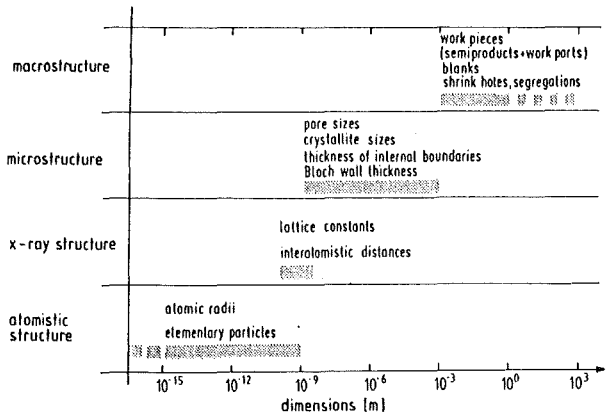

Fig. 1: Subdivision of materials structure.

In this context the properties of a material are understood to mean the measurable parameters for characterizing the behavioural modes of the material under given conditions of state. These can then be combined into groups from the point of view of the microstructure- property relationship on the basis of analogies and having certain things in common [206] (see Fig. 3). Thus, for example, the field properties group characterizes the behaviour of materials when electrical, magnetic and temperature field are set up and even when they have a combined effect (electromagnetic fields → optical properties).

The common bond between field properties is here based on:

- the analogy of the field equations for fields of this type [208] which, unlike mechanical stress-strain fields, are not bound to matter and can also exist in a vacuum;
- the derivation of the effective properties for multiphase materials by linear combination of vectors.

As the following treatment of the quantitative relationship between field properties of multiphase materials and their microstructure brings out, the microstructure of a multiphase material may be adequately taken into account by the

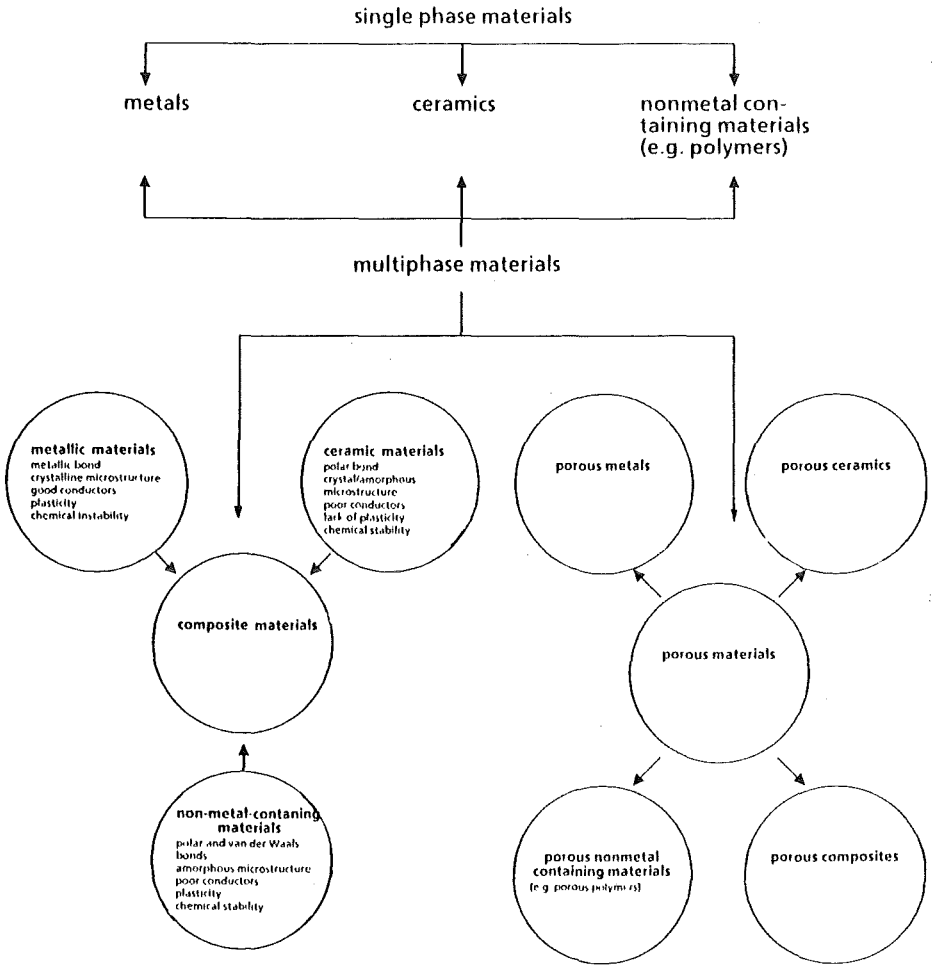

Fig. 2: Subdivision of materials

Materials
Structure and Properties

atomistic structure	thermochemical	properties
X-ray structure	field	properties
microstructure	mechanical	properties
macrostructure	technical	properties

Fig. 3: Structure and property groups.

factors summarized in Fig. 4 [194,195,206,219] supposing, that three presuppositions are fulfilled:

- the equilibrium premise
- the continuum premise
- the mean value premise

Equilibrium in this context concerns the state of thermochemical equilibrium where the microstructure does not change with time but is stable.

The continuum principle implies a macroscopically homogeneous material referring to a microscopically quasihomogeneous local distribution of the microstructural constituents between which - at the phase boundaries - a continuous interface bonding exists.

implicit parameters	1. number of phases	e.g. two-, three-, multiphased premise: thermochemical equ librium
	2. type of microstructure matrix phase microstructure interconnecting phase microstructure	premise: continuum principle
explicit parameters	3. volume fraction of phase (concentration factor) volume x number of the phase particles	premise: spheroidal model mean values
	4. shape of phase particles (shape factor)	
	5. orientation of phase particles (orientation factor)	

Fig. 4: Characteristics of microstructure.

By the mean value premise, which is explained under chapter 2.3 in detail, it is assumed, that mean values for the shape and orientation of the phase particles may fictitiously substitute for the real data, being a distribution function of axial ratios and orientation angle.

2. *On the Theory about the Relationship between Microstructure and Field Properties*

2.1 Expressions in the literature

For more than a hundred years numerous correlations have been advanced in the literature which, on empirical, semi-empirical or theoretical grounds are intended to account mathematically for the relationship between the microstructure and field properties of two-phase materials. In the original papers they are given for electrical resistance [171], dielectric constant [273], electrical [131] and thermal [30] conductivities, magnetic permeability [105] and optical properties [1,152] as the optical refractive index [163] or - more generalized recently - as permitivities for transport properties [27,58,72,174,175,181,182,216] including the optical absorption coefficient and refraction index [181,182]. For better comparison, numerous of these correlations were later transcribed to the electrical resistivity of two-phase materials by applying analogies of field property parameters [208], bringing out, that some of them are identical in content but different in the original form only. Their reliability from an engineering point of view was checked with plausibility criteria as boundary conditions [27,182,208]. Thus for example, the condition must be met that

- the effective field properties, e.g. conductivity, of the two-phase material becomes identical with that of one phase when the concentration of the other phase is zero; or
- a real effective conductivity must exist for such a material, even when that of one phase approaches zero (the second phase being pores); or
- the effective field property of a two-phase material has to be indentical with that of its phases, if the field properties, e.g. conductivities, of the phases are equal.

Surprisingly the number of equations reduced to a few by this procedures and it was possible to select certain reliable correlations in this way [196], for which two methods of theoretical derivation have been described: the bound and model concepts, respectively.

2.2 The bound concept: field property bound equations

Considering the interaction between a "primary" field and a material introduced into this field, field equations as correlation functions provide the combination of primary field parameters, such as the external field strength, with the field para-

meters in the material resulting from interaction [105]. These correlation functions comprise the specific characteristic field parameters of the material, such as the thermal or electrical conductivity, dielectric constant or magnetic permeability and for a homogeneous single-phase material, enable to calculate the energy introduced into the material by interaction with the field.

In case of the bound concept the constituents of the two-phase material are considered separately in the respective electrical, magnetic or temperature field as shown in Fig. 5.

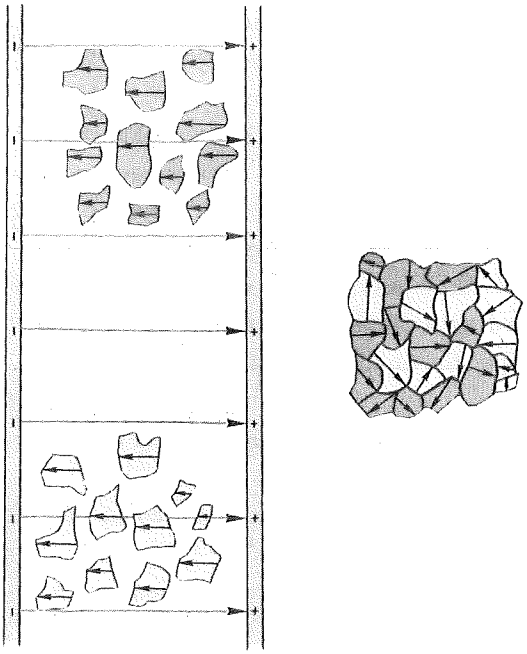

Fig. 5: Bound concept schematically.

By field influence the phases (or constituents) take up field energy, where these energy terms behave additively, when composing the constituents to one piece. The resulting energy equation provides two solutions for the effective field property; the solutions themselves depend on the microstructural information to be available or assumed to be correct as limiting conditions:

for example supposing or knowing nothing more, than that the material is two-phased one obtains an utmost upper ($\phi^{I}C$) and a lower value (ϕ_{IC}) bounding all possible property quantities in between I. order bounds (Fig. 6, equations 1a and 1b) so called for referring to one single assumption: the

number of phases. These I. order bound equations (≙ I. order engineering approach) correspond formally to the well-known Kirchhoff laws for series and parallel arrays of the phases, although the derivation does not prescribe such an arrangement of the phases but accepts it as one of various possibilities. As the physical-mathematical derivation implies, the I. order bounds are the ultimate bounds for the field properties of a two-phase material stating, that no values may exist outside the bounds!

	lower bounds	upper bounds
I. order	(1a) $\varphi_{IC} = \frac{\varphi_1 \varphi_2}{c_2\varphi_1 + (1-c_2)\varphi_2}$	(1b) $\varphi^{I}_{C} = c_2\varphi_2 + (1-c_2)\varphi_1$
II. order	(2a) $\varphi_{IIC} = \varphi_1 \frac{3\varphi_2 + 2(1-c_2)(\varphi_1-\varphi_2)}{3\varphi_1 - (1-c_2)(\varphi_1-\varphi_2)}$	(2b) $\varphi^{II}_{C} = \varphi_2 \frac{3\varphi_1 + 2c_2(\varphi_2-\varphi_1)}{3\varphi_2 - c_2(\varphi_2-\varphi_1)}$
	$\varphi_1 < \varphi_2$	
III. order	(3a) $1-c_D = \frac{\varphi_{IIIC} - \varphi_D}{\varphi_M - \varphi_D} \frac{\varphi_M + 2\varphi_D}{\varphi_{IIIC} + 2\varphi_D}$	(3b) $1-c_D = \frac{\varphi^{III}_{C} - \varphi_D}{\varphi_M - \varphi_D} \sqrt[3]{\frac{\varphi_M}{\varphi^{III}_{C}}}$
	$\varphi_D < \varphi_x$	

Fig. 6: Bound equations of field properties (ϕ_1, ϕ_2 = field property values of phase 1,2; ϕ_M, ϕ_D = field property values of phase M,D; c_1, c_2, c_D = volume content of phase 1, 2, D).

- another couple of equations represents closer II. order bounds (ϕ^{II}_C, ϕ_{IIC}) being valid for materials with two microstructural items of information: the material is two-phased and the material is isotropic (statistical orientation; II. order engineering approach).

- finally knowing that the material is two-phased, isotropic and that one phase serves as a continuous matrix-phase, whilst the other is included discontinuously we get even closer III. order bounds (ϕ^{III}_C, ϕ_{IIIC}) due to three microstructural assumptions: the number of phases to be two; the type of microstructure to be a matrix phase type; the orientation of phases to be statistical, representing an isotropic material without definite information on concentration and shape of the phases (compare Fig. 4).

In the meantime, these bound equations have been confirmed by different ways of derivation [24,26,27,28,181,182] as the finite element approach [58] and bounding equations of higher order have been derived [182] also for other than field properties [144,145,149]. But despite this success and despite the fact, that equations (1) and (2) are derived rigorously according to theory, they are still inadequate for the following reasons:

- the lower bounds disappear when pores are the second phase ($\phi_2 \rightarrow 0$);
- the range of variation is too large, even between the II. order bounds, when the field-property values for the phases of a two-phase material are very different (compare Fig. 7);
- the bounds do not permit any feedback to the technological question important for "constructing taylor-made engineering materials", how microstructure effects the property variation between them; in other words (compare Fig. 8): the question is open how to move the property of an in-situ produced two-phase material between the bounds (circled in Fig. 8) either at constant composition to "better" values (e.g. technically) or at constant property to most efficacious ($\doteq$ least expensive, most economical or ecological by saving rare or risky components etc) phase concentrations by optimized microstructures.

Since the scientific principle considers "knowing" and "knowing better" to be anyway better than "not knowing" or "knowing less" and since - also from a technological point of view - an even better insight into the microstructure-property correlation could provide closer bounds or even singular values, where sufficient microstructural information is available, efforts were therefore made to develop the microstructure field-property correlation further, by an alternative method requiring the mathematical treatment of a model structure which approximately characterizes that of the real material.

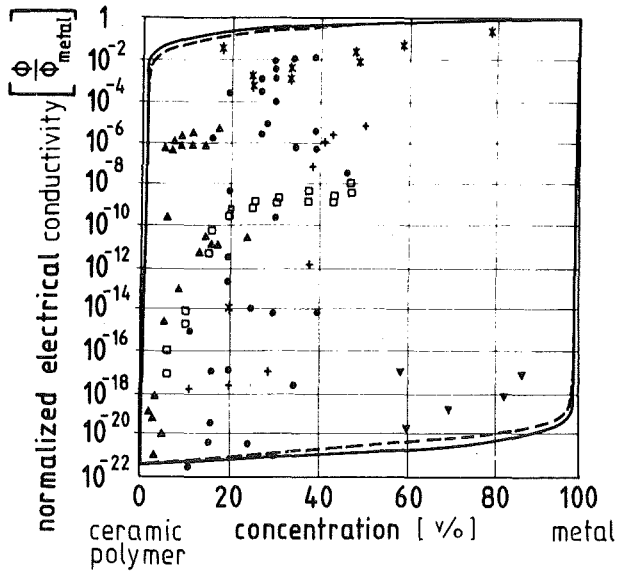

Fig. 7.: Electrical conductivity of composites at room temperature: Al_2O_3-Ag [35,195,] (*) bakelite-Ag [101] (+), polyethylen ($CH_2 = CH_2)_n$-Ni [169] (●), PVC-Cu [32,64] ( ), resin-Cu [104] ( ), resin-Fe (□); I. order bounds (–), II. order bounds (---).

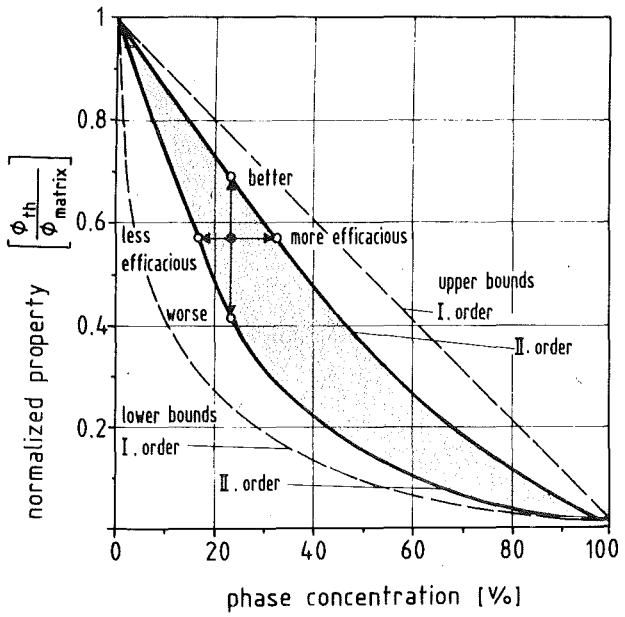

Fig. 8: Bounds and tayloring materials.

2.3 The model concept: microstructure-field property equations

This exact characterization of a fictitious model always gives an inexact description of the real material, but its physical and engineering quality can be checked firstly by comparison with rigorous theoretically derived equations (1) and (2) and secondly by comparison with experimental values.

The chosen model proceeds from a real two-phase material, the microstructure of which consists of a continuous (matrix) phase in which the particles of the other (inclusion) phase are embedded discontinuously but macroscopically quasi-homogeneously. These particles which are normally irregularly shaped in real materials are replaced by spheroids, i.e. particles with a regular mathematically-definable geometry and geometric arrangement within the material, having a unique mean form, size and orientation (mean value premise; fig. 9).

The mean form is given by the ratio of the rotational (z) axis to the minor (x) axis of the speroid substituting the real particles. To obtain this, each real particle is considered to be replaced by a spheroid having the same surface-to-volume ratio

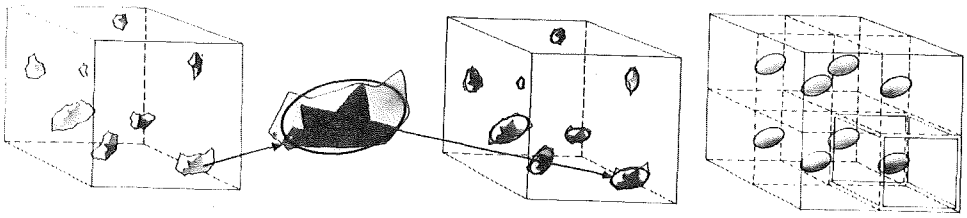

Fig. 9: Model concept - mean value premise.

as the real particle and therefore a specific axial ratio. The mean value of the axial ratios of all the particles (n)

$$\overline{\left[\frac{z}{x}\right]} = \frac{\sum_{i=1}^{n} \left|\frac{z}{x}\right|_i}{n} \tag{4}$$

corresponds to the axial ratio of the spheroid by which the real particles are replaced in the model. It is found in chapter 3 of this publication that for a given axial ratio there are two alternatives for substituting the real particles of the inclusion phase, namely either by an oblate spheroid or a prolate one. Stereologically, one actually obtains two axial ratios for each of the two types, hence a total of four from which, however, one can normally be selected preferentially for substituting the real particles.

The mean size of the spheroids substituted for the real included particles is determined by their number and the volume concentration of the inclusion phase;

and

the mean orientation is determined by the orientation of the rotational axes of the substituting spheroids to the field strength gradient's direction (Fig. 10).

A comparison of these modelling assumptions, namely:

- two-phase stable nature (≙ number of phases in equilibrium)
- matrix structure (≙ arrangement of phases) with macroscopically homogeneous distribution and continuous phase boundary (continuum premise) and
- characterization of the form, orientation and size of the particles of the inclusion phase by uniform spheroids (spheroidal mean value premise).

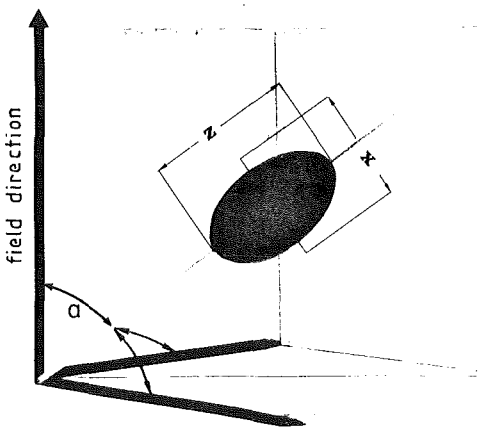

Fig. 10: Model concept - orientation angle (α) of a substituting spheroid.

with the five essential parameters given in Fig. 4 for the quantitative characterization of microstructure, shows that instead of the volume content of the phases in the model, the mean size of the phase particles (not accurately defined) and their number appear in the first instance. This is explained by the fact that instead of the five parameters given in Fig. 4 actually seven quantitative microstructural parameters would be required for the complete characterization of the microstructure of a two-phase material [194], which are

- the number of phases
- the arrangement of phases
- the shape of inclusions
- the orientation of inclusions
- the size of inclusions
- the local distribution of inclusions

Because of the continuum premise, the distribution parameter can be dispensed since the local distribution is assumed statistically homogeneous, whilst, as is shown later (chapter 3), the size and number of included phase particles can be combined in one microstructural parameter: the phase concentration factor.

Spheroidal characterization of the inclusion phase particles, and only this, offers certain advantages:

- high adaptability to real irregular geometries by continuously changing the axial ratio whose extreme cases include disc-shaped ([z/x] → 0; platelets) and

cylindrical inclusions ([z/x] → ∞; fibres) and the special case of which ([z/x] = 1) corresponds to spherical inclusion phase particles (Fig. 11).

- there are no points of discontinuity such as corners and edges, which could represent barriers for the mathematical treatment of the field potential of interfaces in two-phase materials;

the substituting spheroid best-suited to a real structure can be determined by quantitative microstructural analysis, by means of available stereological functions (see chapter 3).

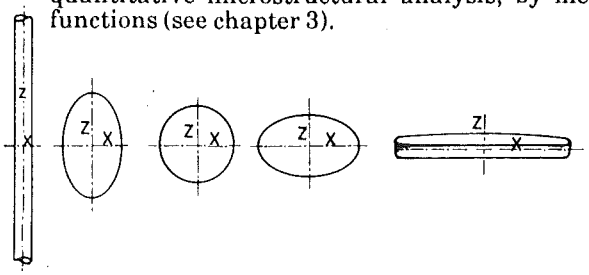

Fig. 11: Spheroidal shape variation.

Theoretical treatment of the model begins with the characterization of the homogeneous field in the single-phase material by its field equation. Including spheroids into the single-phase material which, in fact, substitutes the real inclusions, leads to an interference ("stray") field being generated by electrostatic induction and superimposed on the original field, which depends on shape and orientation (Fig 12).

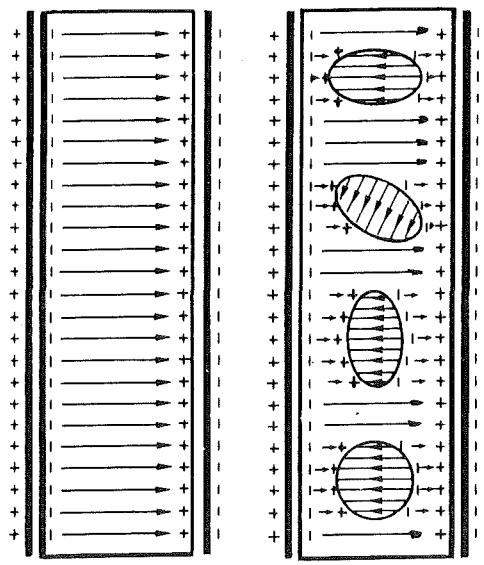

Fig. 12: Field superposition (schematic) in two-phase a material.

The field equation can be written for both fields and the resultant field is given by superposition of the homogeneous primary field and the induced interference field, as will now be exemplified by an electrical field:

The field strength within an spheroidal particle (E_D) located in a homogeneous external field (matrix field ≙ primary field; field strength E_M) is given by [126,219,249,273]:

$$\frac{E_D}{E_M} = \sum_{i=x}^{z} \frac{\varepsilon_M \cos^2 \alpha_{iD}}{\varepsilon_M + (\varepsilon_D - \varepsilon_M) F_{iD}} \tag{5}$$

where:

F_{iD} = de-electrification or depolarization factor, referred to the i = x,y,z axis of the included ellipsoidal phase particle

$\varepsilon_M, \varepsilon_D$ = dielectric constants of matrix and inclusion phases, respectively

α_{iD} = angle of orientation of the i = x,y,z axis of the ellipsoidal particle of the inclusion phase, with respect to field strength gradient direction (Fig. 10).

and where

$$\sum_{i=x}^{z} F_{iD} = 1 \tag{6}$$

and

$$\sum_{i=x}^{z} \cos^2 \alpha_{iD} = 1 \tag{7}$$

For ellipsoids of revolution (≙ spheroids; axis of rotation z, minor axis x = y), one gets in accordance with equation (6)

$$F_{zD} = 1 - 2F_{xD} \tag{8}$$

so that F_{zD} can always be expressed by F_{xD}. In the following derivation, therefore, only $F_{xD} = F_D$ is used as shape factor for the inclusion phase, where [208,244,273]:

$$F_{xD} = F_D = \frac{x^2 z}{2} \int_{w=0}^{\infty} \frac{dw}{(x^2 + w)^2 \sqrt{z^2 + w}} \tag{9a}$$

which results

- for prolate spheroids in

$$F_D = \frac{x}{2z\left(1 - \left|\frac{x}{z}\right|^2\right)}\left\{\frac{1}{\frac{x}{z}} + \frac{x}{2z\sqrt{1 - \left|\frac{x}{z}\right|^2}} \ln \frac{1 - \sqrt{1 - \left|\frac{x}{z}\right|^2}}{1 + \sqrt{1 + \left|\frac{x}{z}\right|^2}}\right\} \tag{9b}$$

- for oblate spheroids in

$$F_D = \frac{x}{2z\left(1 - \left|\frac{z}{x}\right|^2\right)}\left\{\frac{1}{\frac{z}{x}} + \frac{z}{2x\sqrt{1 - \left|\frac{z}{x}\right|^2}} \ln \frac{1 - \sqrt{1 - \left|\frac{z}{x}\right|^2}}{1 + \sqrt{1 + \left|\frac{z}{x}\right|^2}}\right\} \tag{9c}$$

In equation (9) only the axial ratio [x/z] occurs, but not the axial lengths (x,z) alone. Accordingly, this is only a shape factor, for which the size of the particle is of no importance!

With equation (7) ($\cos^2\alpha_D = \cos^2\alpha_{zD}$) (8) and (9) ($F_D = F_{xD}$) one obtains from equation (5)

$$\frac{E_D}{E_M} = \frac{\varepsilon_M (1 - \cos^2\alpha_D)}{\varepsilon_M + (\varepsilon_D - \varepsilon_M) F_D} + \frac{\varepsilon_M \cos^2\alpha_D}{\varepsilon_M + (\varepsilon_D - \varepsilon_M)(1 - 2F_D)} \tag{10}$$

In accordance with the assumption made for equation (5), namely that a spheroidal phase particle exists in a homogeneous primary field, equation (10) applies only as long as the primary matrix field (E_M, ε_M) remains homogeneous and constant. An interference field is now induced in and around the included particle and the effect of this field on the field in the matrix phase can be considered negligible providing the concentration of included phase particles is small; i.e. the greater part of the field in the matrix phase remains undisturbed. Equation (10), applied to a two-phase material with matrix structure, is therefore only valid for low concentration of the inclusion phase.

On the other hand, the effective field strength (E_C) of a two-phase material (and also its dielectric displacement D_D) can be calculated from the corresponding parameters of its phases (E_M, E_D and E_M, D_D, respectively) and their respective volumes in accordance with Wiener's mean value theorems [274]:

$$E_C = c_M E_M + c_D E_D \tag{11}$$

$$D_C = c_M D_M + c_D D_D \tag{12}$$

(c_D = volume content of the inclusion phase; $c_M = 1 - c_D$ = volume content of matrix phase) with

$$D_i = E_i \varepsilon_i \tag{13}$$

($i \doteq C,M,D$). It follows from equation (11) that

$$\frac{E_D}{E_M} = \frac{E_C - c_M E_M}{c_D E_M} \tag{14}$$

which leads with equations (12) and (13) to

$$\frac{E_D}{E_M} = \frac{c_M}{c_D} \frac{\varepsilon_M - \varepsilon_C}{\varepsilon_C - \varepsilon_D} \tag{15}$$

Comparison of equations (15) and (10) provides

$$\frac{c_M}{c_D} \frac{\varepsilon_M - \varepsilon_C}{\varepsilon_C - \varepsilon_D} = \varepsilon_M \left| \frac{1 - \cos^2 a_D}{\varepsilon_M + (\varepsilon_D - \varepsilon_M) F_D} + \frac{\cos^2 a_D}{\varepsilon_M + (\varepsilon_D - \varepsilon_M)(1 - 2F_D)} \right| \tag{16}$$

If in accordance with a field equation analogy [208], a general field property parameter (ϕ_i) is used substituting the dielectric constants (ε_i) in equation (16) and if equation (16) is solved for the effective field property of the two-phase material (ϕ_C), one obtains

the microstructure field-property correlation for two-phase materials with matrix microstructure at low concentrations of the inclusion phase:

$$\phi_C = \phi_M \frac{1 - c_D + c_D \phi_D \left| \frac{1 - \cos^2 a_D}{\phi_M + (\phi_D - \phi_M) F_D} + \frac{\cos^2 a_D}{\phi_M + (\phi_D - \phi_M)(1 - 2F_D)} \right|}{1 - c_D + c_D \phi_M \left| \frac{1 - \cos^2 a_D}{\phi_M + (\phi_D - \phi_M) F_D} + \frac{\cos^2 a_D}{\phi_M + (\phi_D - \phi_M)(1 - 2F_D)} \right|} \tag{17}$$

or rewritten

$$\Phi_C = \Phi_M \frac{1 + \frac{c_D}{c_M}\Phi_D\left[\frac{1-\cos^2\alpha_D}{\Phi_M + (\Phi_D - \Phi_M)F_D} + \frac{\cos^2\alpha_D}{\Phi_M + (\Phi_D - \Phi_M)(1-2F_D)}\right]}{1 + \frac{c_D}{c_M}\Phi_M\left[\frac{1-\cos^2\alpha_D}{\Phi_M + (\Phi_D - \Phi_M)F_D} + \frac{\cos^2\alpha_D}{\Phi_M + (\Phi_D - \Phi_M(1-2F_D)}\right]} \tag{18}$$

For the spherical form of the included phase particles, ($F_D = 0.33$; $\cos^2\alpha_D = 0.33$; compare chapter 3), the equation (18) is identical with the Maxwell equation derived for this case [171], which in turn is approximately the same as the corresponding equation form by Niesel [188,210].

The limitation of equation (18) to low concentrations of the inclusion phase can be clearly understood in the physical sense when it is considered that only superposition of the homogeneous primary field and induced interference field within the included spheroidal particles was taken into account in the derivation, but not superposition of the homogeneous primary field and the induced external interference field around the different particles of the inclusion phase. In other words: field interference in the matrix phase has been neglected assuming that the majority of the primary field remains undisturbed. This is roughly true as long as the mean interparticle distance (λ) between the inclusion phase particles is bigger than about four times the range of an interference field. Since according to the Fullman equation [265]:

$$\bar{\lambda} = \bar{L}_3 \frac{1 - c_D}{c_D} \tag{19}$$

this mean distance (λ) depends not only on the volume concentration of the inclusion phase (c_D) but also on the size of its particles (L_3 = mean spatial intercept length); mutual superposition of primary field and of interference fields only comes into effect at the higher concentrations of inclusion phase, which vary according to particle size. This interaction of primary and interference fields in the matrix phase is taken into account in the derivation continued below by the "self consistent scheme method", which as will be shown, is proper for an engineering approach but is not mathematically exact and physically rigorous: It is assumed that the two-phase material with a low concentration of inclusion phase can be considered a quasi-homogeneous matrix phase, in which particles of

the inclusion phase are again introduced in low concentration (dc_D) [42,43]. The effective field property can therefore again be determined by means of microstructure field-property correlation (18) already derived for low concentration of the inclusion phase, with

$$\Phi_M \doteq \Phi_C \text{ and } c_M + c_D + dc_D = 1 \tag{20}$$

one obtains from equation (18)

$$\Phi_C + d\Phi_C = \Phi_C \frac{1 + \frac{dc_D}{1 - c_D - dc_D}\Phi_D \left| \frac{1 - \cos^2\alpha_D}{\Phi_C + (\Phi_D - \Phi_C)F_D} + \frac{\cos^2\alpha_D}{\Phi_C + (\Phi_D - \Phi_C)(1 - 2F_D)} \right|}{1 + \frac{dc_D}{1 - c_D - dc_D}\Phi_C \left| \frac{1 - \cos^2\alpha_D}{\Phi_C + (\Phi_D - \Phi_C)F_D} + \frac{\cos^2\alpha_D}{\Phi_C + (\Phi_C - \Phi_M)(1 - 2F_D)} \right|} \tag{21}$$

and by rearrangement (see also equation (16)

$$\frac{dc_D}{1 - c_D - dc_D} = \frac{d\Phi_C}{\Phi_C(\Phi_D - \Phi_C - d\Phi_C) \left| \frac{1 - \cos^2\alpha_D}{\Phi_C + (\Phi_D - \Phi_C)F_C} + \frac{\cos^2\alpha_D}{\Phi_C + (\Phi_D - \Phi_C)(1 - 2F_D)} \right|} \tag{22}$$

With the simplifying relationship

$$dc_D \ll (1 - c_D) \text{ and } d\Phi_C \ll \Phi_C \tag{23}$$

one gets the approximate form

$$\frac{dc_D}{1 - c_D} = \frac{d\Phi_C}{\Phi_C(\Phi_D - \Phi_C) \left| \frac{1 - \cos^2\alpha_D}{\Phi_D + (\Phi_D - \Phi_C)F_D} + \frac{\cos^2\alpha_D}{\Phi_C + (\Phi_D - \Phi_C)(1 - 2F_D)} \right|} \tag{24}$$

the integration of which - on the left-hand side between the (concentration) limits 0 and c_D, on the right-hand side between the (field property) limits Φ_M and Φ_C - gives the general microstructure field-property correlation for two-phase materials with no limitation on the phase concentration. In accordance with an earlier suggestion [209,243], equation (24) can be integrated by breaking the right-hand side down into partial fractions; by rearrangement one obtains

$$\frac{dc_D}{1-c_D} = d\Phi_C \frac{2F_D(1-F_D)\Phi_C^2+(1-3F_D+4F_D^2)\Phi_C\Phi_D+F_D(1-2F_D)\Phi_D^2}{\Phi_C(\Phi_D-\Phi_C)\{\Phi_C[2F_D+\cos^2\alpha_D(1-3F_D)]+\Phi_D[1-2F_D-\cos^2\alpha_D(1-3F_D)]\}} =$$

$$= d\Phi_C \frac{Q(\Phi_C)}{P(\Phi_C)} \tag{25}$$

with - according to the rule of the partial fraction method [40] -

$$\frac{Q(\Phi_C)}{P(\Phi_C)} = \frac{R}{\Phi_C-\Phi_{C1}} + \frac{S}{\Phi_C-\Phi_{C2}} + \frac{T}{\Phi_C-\Phi_{C3}} \tag{26}$$

The solutions of the denominator function P (Φ_C) in equations (25) and (26) are

$$\Phi_{C1} = 0;\ \Phi_{C2} = \Phi_D;\ \Phi_{C3} = \Phi_D\left[1 - \frac{1}{2F_D+\cos^2\alpha_D(1-3F_D)}\right] \tag{27}$$

and

$$R = \frac{Q(\Phi_{C1})}{P'(\Phi_{C1})} = \frac{F_D(1-2F_D)}{1-2F_D-\cos^2\alpha_D(1-3F_D)} \tag{28}$$

$$S = \frac{Q(\Phi_{C2})}{P'(\Phi_{C2})} = -1 \tag{29}$$

$$T = \frac{Q(\Phi_{C3})}{P'(\Phi_{C3})} = \frac{F_D(1-2F_D)}{1-2F_D-\cos^2\alpha_D(1-3F_D)} + \frac{2F_D(1-F_D)}{2F_D+\cos^2\alpha_D(1-3F_D)} - 1 \tag{30}$$

Taking equations (26) to (30) into account and introducing the integrals, one obtains from equations (25)

$$\int_0^{c_D}\frac{dc_D}{1-c_D} = \int_{\Phi_M}^{\Phi_C}\frac{R\,d\Phi_C}{\Phi_C} - \int_{\Phi_M}^{\Phi_C}\frac{d\Phi_C}{\Phi_C-\Phi_D} + \int_{\Phi_M}^{\Phi_C}\frac{T\,d\Phi_C}{\Phi_C-\Phi_D\left[1-\frac{1}{2F_D+\cos^2\alpha_D(1-3F_D)}\right]} \tag{31}$$

Another derivation of equation (31) by partial fractions and the method of indeterminate coefficients has already been demonstrated explicitly elsewhere [243]. As already reported [195,209,215,243], its integration gives a (model) microstructure-field property correlation with no limitation on phase concentration:

$$1 - c_D = \frac{\Phi_D - \Phi_C}{\Phi_D - \Phi_M} \left| \frac{\Phi_M}{\Phi_C} \right|^R \left| \frac{\Phi_C + \Phi_D \left\{ 1 - \frac{1}{2F_D + \cos^2 a_D (1 - 3F_D)} \right\}}{\Phi_M + \Phi_D \left\{ 1 - \frac{1}{2F_D + \cos^2 a_D (1 - 3F_D)} \right\}} \right|^T \qquad (32)$$

where

Φ	=	field property
D, M, C	=	indices for the inclusion phase D, matrix phase M and two-phase material C
c_D	=	volume content of inclusion phase
	=	phase concentration factor
F_D	=	shape factor
$\cos^2 a_D$	=	orientation factor
R, T	=	exponents in accordance with equations (28) and (30)

As this derivation shows, the effect of microstructure on the field properties of two-phase materials with (model) matrix microstructure is completely taken into account by three microstructural parameters relating to the inclusion phase, which enter the microstructure field-property correlation as:

- phase concentration factor (c_D),
- shape factor (F_D) and
- orientation factor ($\cos^2 a_D$).

The phase concentration factor (c_D) corresponds to the volume content of the inclusion phase (see chapter 3) and is subject to the condition that $0 \leq c_D \leq 1$ and incorporates the two microstructural parameters enumerated at the beginning, namely the "size" and "number" of particles of the included phase particles; since, if, for example, one specifies the size of an oblate or prolate spheroid with the

same ratio of major-to-minor axes (e.g. $[a/b]_{\perp} = [a/b]_{\parallel} = 2$) over its mean intercept length (L_3), one obtains for an oblate spheroid /44/:

$$\overline{L_3} = 1.278\, a \tag{33a}$$

$$V_a = 1.006\,(\overline{L_3})^3 \tag{33b}$$

$$V_M + N_D \cdot V_a = V_M + N_D \cdot 1.006\,(L_3)^3 = V \doteq 1 \text{(unit volume)} \tag{33c}$$

$$c_D = \frac{N_D \cdot 1.006\,(\overline{L_3})^3}{V_M + N_D \cdot 1.006\,(\overline{L_3})^3} \doteq N_D \cdot 1.006\,(\overline{L_3})^3 \tag{33d}$$

or for a prolate spheroid respectively

$$\overline{L_3} = 1.46\, b \tag{34a}$$

$$V_g = 2.69\,(\overline{L_3})^3 \tag{34b}$$

$$c_D = \frac{N_D \cdot 2.69\,(\overline{L_3})^3}{V_M + N_D \cdot 2.69\,(\overline{L_3})^3} \doteq N_D \cdot 2.69\,(\overline{L_3})^3 \tag{34c}$$

and hence:

$$c_D = f(L_3, N_D, V_M) \tag{35}$$

where

$V_{a,g}$ = volume of single oblate or prolate spheroid
N_D = number of spheroidal particles of inclusion phase in the total volume
V_M = volume of matrix phase

Size and number as microstructural parameters for the particles of the inclusion phase are accordingly not independent of each other, but may only be varied in combination, via the phase concentration factor. This is an understandable consequence of the self consistent scheme method, which formally and descriptively

takes account of interference field superpositions at all concentrations, although they become negligibly small at low concentrations. Really effective interference field superpositions in the matrix phase therefore only begin above a certain concentration of the inclusion phase, depending on the size of its particles. The onset of interference field superposition and hence the effect of particle size as an independent variable, is irrelevant for the result of equation (32).

The shape factor in equation (32) corresponds to the depolarization or de-electrification factor and is given by the ratio of the axis of revolution to the minor axis of the spheroid substituted for the real particles. It can be calculated in accordance with equation (9) for every axial ratio /8,39/ and is subject to the condition $0 \leq F_D \leq 0.5$ with $F_D = 0.33$ for spherical particles of the inclusion phase. The result of this calculation is shown graphically in Fig. 13 (compare also chapter 3).

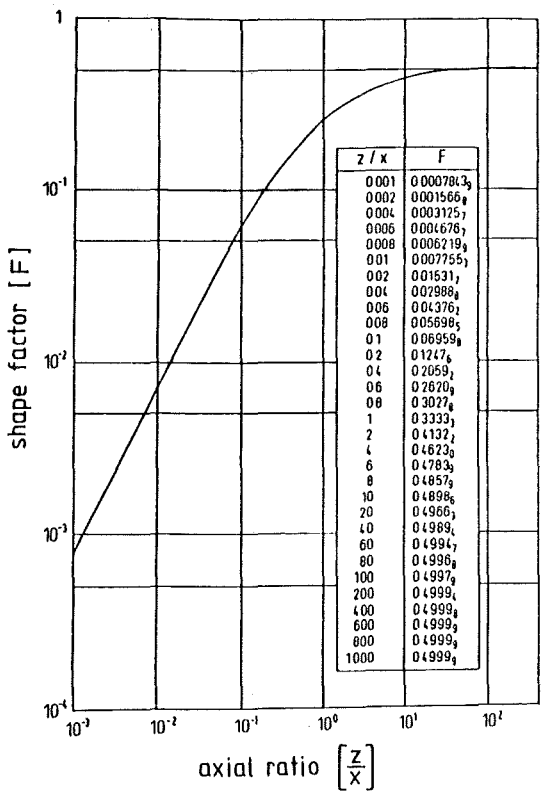

Fig. 13: Depolarization factor ≙ shape factor as function of the axial ratio of spheroids.

Finally, the orientation factor is given in accordance with the derivation by the cosine squared of the angle formed by the axis of revolution of the substituted spheroid and the field strength gradient direction (Fig. 10); it is subject to the condition $0 \leq \cos^2 a_{I)} \leq 1$ with $\cos^2 a_{I)} = 0.33$, for statistical orientation, i.e. randomly oriented or isotropic inclusion of the particles of the inclusion phase (see chapter 3).

2.4 *Convergence between bound concept and model concept*

The model on which equation (32) is based and the - mathematically inexact - derivation of the correlation by the self-consistent scheme method make its physical and engineering "quality control" an absolute necessity from the point of view of reliability and hence usefulness. This can be achieved physically by ensuring that equation (32) leads to the same results when applying the boundary conditions used for deriving the equations by the the bound concept.

The bounding equations of the I. order correspond to the Kirchhoff laws for parallel and series arrangement of the two phases, where the upper bound values refer to parallel, the lower to series arrays. In the spheroidal microstructural model, parallel arrangement of the phases may be represented by two equally justifiable cases:

- discs oriented perpendicularly to the direction of the field strength gradient ($\cos^2 a_{I)} = 0$; $\lim z/x = 0 \rightarrow F_{I)} = 0$, comp. Fig. 13)
- cylinders oriented parallel to the direction of the field strength gradient ($\cos^2 a_{I)} = 0$; $\lim z/x = \infty \rightarrow F_{I)} = 0.5$, comp. Fig. 13).

On the other hand, series arrangement of the phases with regard to the spheroidal microstructural model may be realized only by discs oriented parallel to the direction of the field strength gradient.

From the conventional, macroscopical consideration according to Kirchhoff's laws follows the imagination, that the discs are realized stereologically in the model concept, when the minor axis is "infinite" compared to the finite axis of revolution ($\lim z/x = 0$) whilst cylinders correspond to "infinite" fibres, having an "infinite" axis of revolution compared to their finite minor axis ($\lim z/x = \infty$). In this context "infinite" means a dimension analogous to the dimension of the two phase materials specimen. This imagination does not judiciously agree with the supposition

of a matrix microstructure, made for the derivation in the model concept. It is, however, possible stereologically to realize discs (lim z/x = 0) and by assuming an "infinite" small axis of revolution compared with a finite minor axis and to assume a finite axis of revolution compared with an "infinite" small minor axis in the case of cylinders ("short fibres"). Both cases are totally equally justified to the ones described first but fit with the assumption of discs and cylinders included in a matrix phase as made for the model concept.

Applying these boundary conditions to equation (32) and substituting the indices (M,D $\doteq$ 1,2) provides equations (1a) and (1b) for I. order bounds (Fig. 6).

A second "physical quality control" of equation (32) is given by the boundary condition which follows from the II. order bounds (equations (2a) and (2b), Fig. 6) for the model, namely "statistical orientation". Substituting the corresponding orientation factor ($\cos^2\alpha_D = 0.33$) in equation (32) and varying the shape factor ($0 \leq F_D \leq 0.5$), as well as assuming first the phase with the higher field property parameter (e.g. higher conductivity $\phi_M = \phi_2 > \phi_D = \phi_1$, see Fig. 14a) as the particular matrix phase and then the phase with the lower field property parameter (e.g. lower conductivity: $\phi_M = \phi_1 > \phi_D = \phi_2$, see Fig. 14b) as the model concept requires results in upper and lower bounds in each case. In order to eliminate the assumption of a particular phase as the matrix, the highest and lowest of the 4 bounds thus obtained must be considered the II. order bounds for two-phase isotropic microstructure. Superposition of the bounding curves for a matrix phase with higher field property parameters, with those for a matrix phase with lower parameters provides graphically the extreme bound plots for the isotropic two-phase model microstructure (see Fig. 14c). Here surprisingly, the upper bound curve corresponds to a model structure in which the phase with the lower field property forms the matrix phase in which randomly oriented disc-shaped particles of the inclusion phase with the lower field property parameter are embedded discontinuously ($\cos^2\alpha_D = 0.33$, $F_D = 0$). On the other hand, the lower bound curve applies for a model structure in which the phase with the higher field-property parameter forms the matrix phase, in which (randomly oriented) disc-shaped particles of the phase with the lower field property parameter are discontinuously included ($\cos^2\alpha_D = 0.33$, $F_D = 0$). Applying the corresponding orientation and form factors ($\cos^2\alpha_D = 0.33$, $F_D = 0$) in equation (32) and substituting the indices (M = 2, D = 1 for $\phi_D < \phi_M$, M = 1, D = 2, for $\phi_D > \phi_M$), results in equation (3a) and (3b) for II. order bound (Fig. 6).

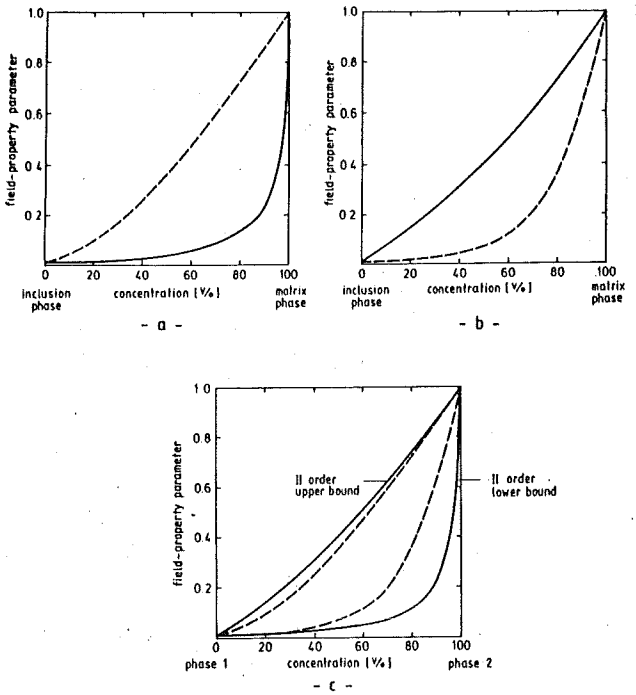

Fig. 14: III. (a,b) and II. order bounds (c).

Convergence between the bound and model concepts is therefore demonstrated physically. This is why now equation (32) resulting from the model concept can be used for deriving bound equations of higher order for two-phase materials (≙ number of phases). With known matrix phase (≙ arrangement of phases) and isotropic microstructure (≙ orientation factor), hence, three defined preconditions for microstructure, "closer" bounding equations of the III. order (3a, 3b; Fig. 6) follow from equation (32), whereby equation (3a) characterizes the lower bound when the matrix phase has the higher field-property value as compared with that of the inclusion phase ($\phi_M > \phi_D$; Fig. 14). With respect to the model concept the lower bound equation reflects statistically oriented disc-shaped inclusion ($\cos^2\alpha_D = 0.33$; $F_D = 0$), whilst the upper bound refers to spherical inclusion ($\cos^2\alpha_D = 0.33$; $F_D = 0.33$), both in a matrix phase which has the higher field property.

Equation (3a) becomes the upper bound equation, if the matrix phase has the lower field property compared to the inclusion phase ($\phi_M < \phi_D$) and - ficticiously

in the model concept - the lower bound then refers to spherical inclusion and the upper bound represents statistically oriented disc-shaped inclusions.

It is noteworthy that equation (3a) becomes identical with equation (2a) ($\phi_M \doteq \phi_2$; $\phi_D \doteq \phi_1$), if the matrix phase has the higher field property compared with that of the inclusion phase ($\phi_M > \phi_D$) and that for the reverse case ($\phi_M < \phi_D$) equation (3a) becomes identical with equation (2b) ($\phi_M \doteq \phi_1$; $\phi_D \doteq \phi_2$).

In Fig. 14c the II. order bounding curves were obtained by superposition of two pairs of curves, one of which applied to a matrix phase with the higher field parameter (Fig. 14a) and the other to one with the lower field parameter (Fig. 14b). These two pairs of curves correspond to the III. order bounds for the two-phase isotropic material.

Also the remaining findings on convergence between the bound and model concepts can be demonstrated graphically by way of a representative example. This is shown in Fig. 15 for the function $\phi_C = f(F_D)$ in accordance with equation (32), firstly for isotropic two-phase material ($\cos^2 a_D = 0.33$) with a higher field property ratio between matrix phase and inclusion phase ($\phi_M/\phi_D = 100$) and secondly for similar material with a lower field property ratio ($\phi_M/\phi_D = 0.01$) at constant phase concentration ($c_D = 0.5$). As results from Fig. 15 the two field property values for the shape factor $F_D = 0$ include the field property values for all other form factors and therefore represent II. order bounds. Here, surprisingly, as already mentioned, the lower bound corresponds to a matrix phase whose field property parameter is higher than that of the inclusion phase, whilst the reverse applies for shape factors between the points of intersection of the two curves. In practice this would mean for example that a two-phase isotropic material whose matrix phase has the lower conductivity, exhibits a higher effective conductivity for specific shape factors for the particles of the inclusion phase, than the corresponding two-phase material with the same microstructure, but higher conductivity of the matrix phase. It is an open question how to explain this result and, for instance, whether it is associated with the simplified approximate relationships in the derivation of equation (32). Theoretical and experimental verifications of these findings are necessary.

Different bounds are obtained when the data on microstructure, especially those concerning shape and orientation of the inclusion phase, are derived from measurements on real microstructures. Since, as already mentioned at the outset,

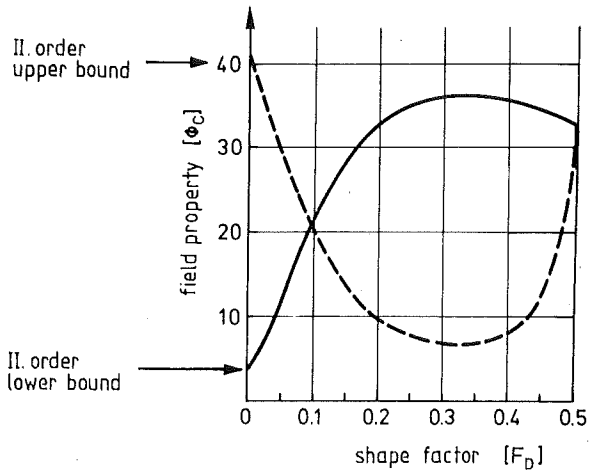

Fig. 15: Field property of a two-phase isotropic material with matrix microstructure and matrix phase with higher (—) and lower (---) field-property parameters, as a function of shape factor.

characterization of shape in accordance with a model is usually ambiguous, two equations result from equation (32) for each of two shape factors which are equally justifiable.

If, with the help of measurement,

- the two-phase state has been established (≙ number of phases)
- the matrix phase has been defined (≙ arrangement of phases)
- the limits have been defined for the shape via defined limits for the ratio of the axis of revolution to the minor axis of the spheroid substituting the particles of the inclusion phase (≙ shape factor) and
- the orientation has been defined of the spheroid substituting the particles of the inclusion phase (≙ orientation factor),

this would be equations presupposing 4 known items of information and, hence determining bounding curves of the IV. order. Obviously the bounds become closer and closer with increasing order or - alternatively expressed - with increasing microstructural information. If, finally, total information would be available about all parameters given in Fig. 4 the upper and lower bounds would converge into each other providing one "singular" curve or function, respectively.

Vice versa, it is also possible to demonstrate the convergence between the bound concept and the model concept by varying the microstructural factors in the model concept as done schematically in Fig. 16 resulting in a steadily shifting of the field property values from one bound to the other.

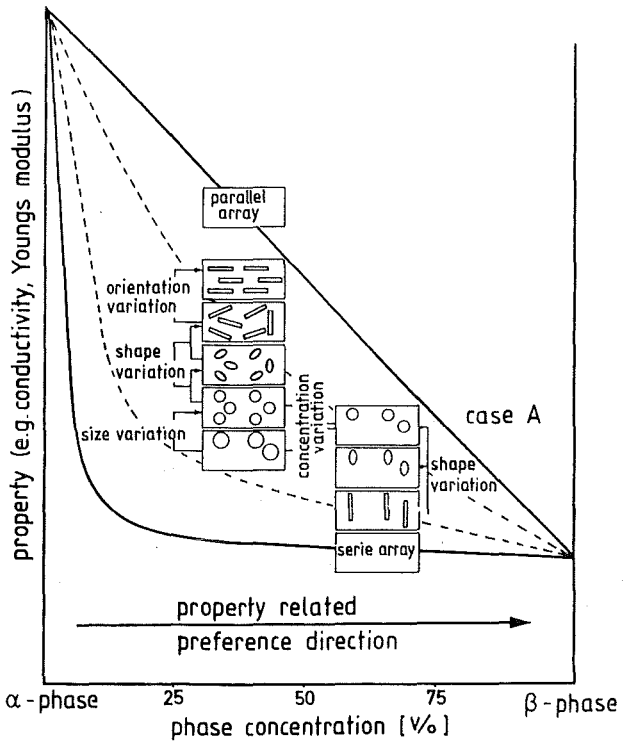

Fig. 16. Schematic bound-model convergency.

2.5 *Matrix and interconnection microstructure*

The correlation found between the bound and model concepts shall now be used to draw another generalized conclusion on plausibility considerations: fundamentally, two microstructures can be distinguished in multiphase microstructures, namely matrix and interconnection microstructures [194,195] (Fig. 17). Matrix microstructure exists when at least one phase (inclusion phase) is included discontinuously in at least one other continuous phase (matrix phase). The inclusion phase can be present throughout in higher concentration than the matrix (Fig. 18). On the other hand, interconnection microstructure exists when

all the phases appearing in the material occur continuously. This is quite generally the case when the phases penetrate three-dimensionally in the form of sponge-like lattice structures. There are transitions between the two microstructural types. Thus, with increasing agglomeration of particles of the inclusion phase and increasing concentration of this phase, there is a steady transition of the matrix microstructure with a specific matrix phase to interconnecting microstructure. Further increase leads through interconnecting microstructure to the formation of a matrix structure, in which the original matrix becomes the inclusion phase. These considerations also make that special case abundantly clear in which all or individual phases occur continuously in multiphase materials only one- or two-dimensionally. Such a material possibly has an interconnecting microstructure in one direction and a matrix microstructure in another and is anisotropic (e.g. parallel or series arrangement of the phases).

In the derivation of equations (1) and (2) for I. and II. order bounds, no assumption is made as to whether the microstructure has a matrix or interconnecting form. The bounds accordingly include not only the field-property values of the two-phase material with matrix microstructure but also those of the two-phase material with interconnecting microstructure. Since these bounds also follow from equation (32) for the model microstructure with the corresponding boundary conditions, it may be assumed that an equation which can be derived by the model concept for the field properties of two-phase materials with interconnecting microstructure, meets the condition that field-property values calculated with it always lie between the corresponding bounds, which follow from bounding equations.

In order to derive such an equation it is assumed that in the interstices of a continuous skeleton of spheroids of one phase, other spheroids of another phase fit so well that they also touch and only negligibly small interstices are still left over. To this quasi-homogeneous two-phase material with interconnecting microstructure (phases m, k) a small quantity of spheroids of the one phase (m) is added only. The change in field property then occurring can be characterized with the known equation for two-phase materials with a matrix microstructure (equation 18) considering the original material consisting of two continuous phases as a quasi-homogeneous matrix phase. This results in an equation with two unknowns, namely the field property parameter of quasi-homogeneous "matrix phase" and the effective field property after addition of a small quantity of the one phase.

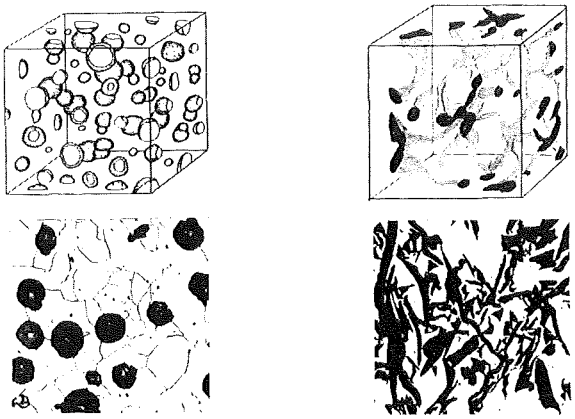

Fig. 17: Matrix and interconnecting phase microstructures.

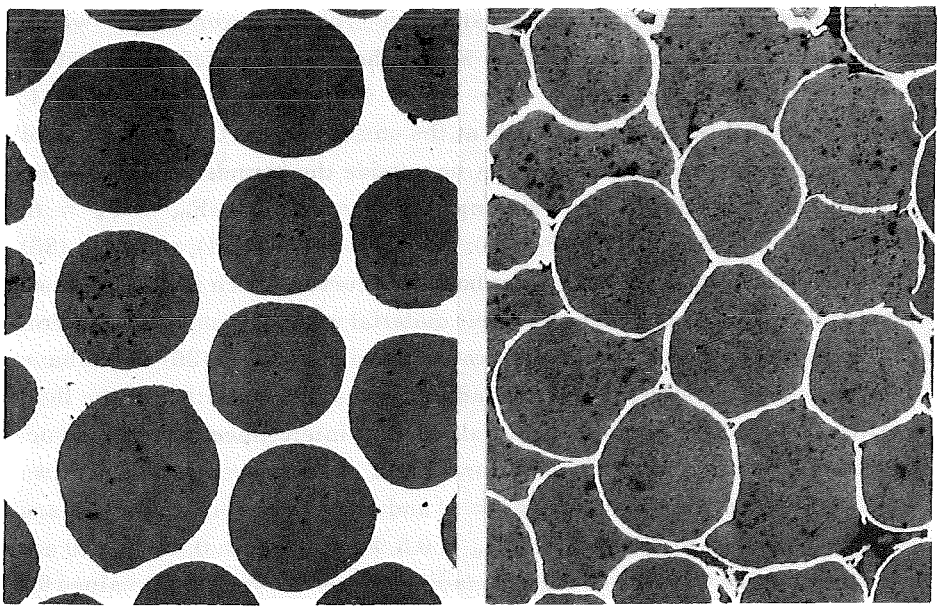

Fig. 18: "Idealized" cermet microstructures (metallic matrix phase, white, ≤ 10 vol.%; ceramic inclusions, dark).

Considering - in this notional experiment - the newly created two-phase material as a quasi-homogeneous matrix phase and adding again a small quantity of the other phase (k), for which the change in field property can be calculated with the equation (18) for a matrix microstructure and low concentration of the inclusion

phase, the effective field property now becomes equally large in the opposite direction. The change in field property caused by the initial addition of phase m is therefore compensated by adding phase (k) and the field property of the new two-phase material must then be identical with that of the two-phase material originally present with a model interconnecting microstructure. With this boundary condition a general microstructure-field property correlation for two-phase materials with interconnecting microstructure follows from the system of equations thus obtained [188,208,243,244]:

$$(1 - c_k)(\phi_m - \phi_C)\left|\frac{1 - cos^2a_m}{\phi_C + (\phi_m - \phi_C)F_m} + \frac{cos^2a_m}{\phi_C + (\phi_m - \phi_C)(1 - 2F_m)}\right| =$$

$$= c_k(\phi_C - \phi_k)\left|\frac{1 - cos^2a_k}{\phi_C + (\phi_k - \phi_C)F_k} + \frac{cos^2a_k}{\phi_C + (\phi_k - \phi_C)(1 - 2F_k)}\right| \qquad (36)$$

For given phase field properties (ϕ_m, ϕ_k) and various phase concentrations which are held constant in each case, one can now vary the form and orientation factors between their possible limits ($0 \leq F_m \leq 0.5$; $0 \leq F_k \leq 0.5$; $0 \leq \cos^2\alpha_m \leq 1$; $0 \leq \cos^2\alpha_k \leq 1$). If the assumption made at the outset is correct, the largest and smallest values then calculated may not lie outside the bounds defined by the bound concept. Accordingly, for bounding cases for example ($F_m = F_k = 0$; $\cos^2\alpha_m = \cos^2\alpha_k = 0$ and $F_m = F_k = 0$; $\cos^2\alpha_m = \cos^2\alpha_k = 1$), equation (36) would have to converge with the I. order bounding curves, which is also the case. Moreover, all values for two-phase isotropic material with interconnecting microstructure ($\cos^2\alpha_m = \cos^2\alpha_k = 0.33$) in accordance with equation (36) would have to lie within the calculable II. order bounding curves. The variation of the field properties of two-phase isotropic materials having interconnecting microstructures ($\cos^2\alpha_m = \cos^2\alpha_k = 0.33$), as a function of phase concentration, for two assumed field properties ($\phi_m = 100$, $\phi_k = 1$) and extreme combinations of shape factor ($F_m = F_k = 0$; $F_m = F_k = 0.5$; $F_m = 0.5$, $F_k = 0$; $F_m = 0$, $F_k = 0.5$) are compared in Fig. 19 with the II. order bounding curves. As shown, all values for interconnecting microstructure lie within these bounds. Apart from that no mathematical demonstration on this subject yet exists, for the reason that preference has been given so far to matrix microstructures. Considering the slope of field properties versus phase concentration for both matrix and interconnection microstructure as shown in Fig. 20 for the electrical conductivity of cermets, it comes out that small changes in phase concentrations result in conductivity alterations only, which do not essentially lie outside the scatter region for

measured values as long as a matrix microstructure exists. In the region of interconnecting microstructure, however - hatched in Fig. 20 - almost "virtual" changes in the phase concentration may cause property drops over orders of magnitudes. Such a sensitivity does not meet the aim testing the quality of

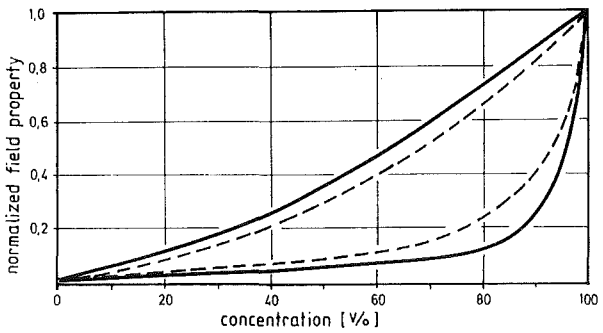

Fig. 19: II. order bounds (—) and calculated extreme-value curves for interconnection microstructure (---).

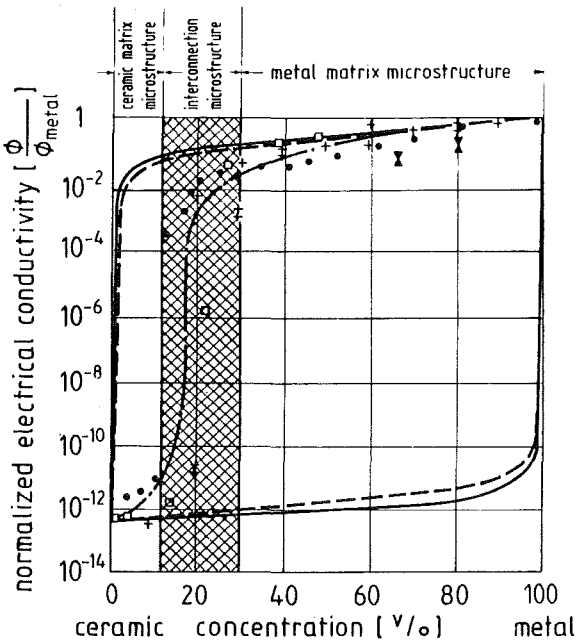

Fig. 20: Electrical conductivity of Al_2O_3-Mo cermets (□) [71], earthenware-Fe cermets (●) [76], $Ba_{2.5}Ca_{0.5+x}WO_6$-W cermets (+) [241] at room temperature and experimental slope (-·-), I. order bounds (—) and II. order bounds (---).

theoretical equations by experimental data. Furthermore in practice it cannot guarantee any acceptable reproducibility due to technological conditions, which neither permit one to fix phase concentrations so accurately nor allow one to realize interconnection microstructures defined in such detail. This is why - apart from the existing equation (36) - the treatment of the relationship between matrix microstructures and field properties deserves priority so far.

2.6 *Special and exceptional cases of the constitutive microstructure-field property equation for two-phase materials*

There are a few special cases of microstructures given by definite orientation factors and shape factors, which lead via equation (32) to the solutions given in Fig. 21.

F_D \ $\cos^2\alpha_D$	0 orientation perpendicular to the field direction	0,33 orientation statistical (isotropic) to the field direction	1 orientation parallel to the field direction
0 cylindrical disc	$1-c_D = \frac{\varphi_D-\varphi_C}{\varphi_D-\varphi_M}$ (37) (≙ I. order upper bound)	$1-c_D = \frac{(\varphi_D-\varphi_C)}{(\varphi_D-\varphi_M)} \cdot \frac{(\varphi_M+2\varphi_D)}{(\varphi_C+2\varphi_D)}$ (38) (≙ II. order bounds for $\varphi_D > \varphi_M$ or $\varphi_D < \varphi_M$)	$1-c_D = \frac{\varphi_D-\varphi_C}{\varphi_D-\varphi_M} \cdot \frac{\varphi_M}{\varphi_C}$ (39) (≙ I. order lower bound)
0,33 sphere	$1-c_D = \frac{\varphi_D-\varphi_C}{\varphi_D-\varphi_M}\left(\frac{\varphi_M}{\varphi_C}\right)^{\frac{1}{3}}$ (40) (≙ III. order upper bound)		
0,5 cylindrical fiber	$1-c_D = \frac{\varphi_D-\varphi_C}{\varphi_D-\varphi_M}\left[\frac{\varphi_M}{\varphi_C}\right]^{\frac{1}{2}}$ (41)	$1-c_D = \frac{\varphi_D-\varphi_C}{\varphi_D-\varphi_M}\left[\frac{\varphi_M+\frac{1}{5}\varphi_D}{\varphi_C+\frac{1}{5}\varphi_D}\right]^{\frac{2}{5}}$ (42)	$1-c_D = \frac{\varphi_D-\varphi_C}{\varphi_D-\varphi_M}$ (43)

Fig. 21: Table of special solutions of the model concept.

These cases are (compare Fig. 21)

- for the orientation of the inclusion:

  statistical orientation; no privileged angle exists between field direction and axis of revolution of the substituting spheroids ($a_D \approx 57°$; $\cos^2 a_D = \frac{1}{3}$; compare chapter 3);

  complete orientation in field direction; all axes of revolution of the substituting spheroids are oriented parallel to the field direction ($a_D = 0°$; $\cos^2 a_D = 1$);

  complete orientation perpendicular to the field direction; all axes of revolution of substituting spheroids are oriented perpendicular to the field direction ($a_D = 90°$; $\cos^2 a_D = 0°$);

for the shape of the inclusions:

cylindrical discs (lim z/x = 0), either formed by a definite minor axis (x) but an indefinite small axis of revolution (z) or formed by definite axis of revolution (z) and by an indefinite large minor axis (x) ($F_D = 0$);

spheres (z/x = 1) formed by equiaxed spheroids ($F_D = \frac{1}{3}$)

cylindrical fibres (lim z/x = ∞), either formed by an indefinite long axis of revolution (z) and a definite minor axis (x; "indefinite fibres") or formed by definite axis of revolution (z) and by an indefinite minor axis (x; "short fibres").

As expected equations (37) and (43) in Fig. 21 are identical to each other and correspond to parallel arrays of the phases (compare also equ. (1a), Fig. 6), whilst equation (39) corresponds to series arrays of the phases (compare equation (1b), Fig. 6). Other identities exist between equation (38) (Fig. 21) and equations (2a), (2b) or (3a) (Fig. 6) as well as equation (40) (Fig. 21) and equation (3b) (Fig. 6). Two other special cases result assuming big differences between the field properties of the phases ($\phi_M \gg \phi_D$; $\phi_M \ll \phi_D$). Taking into account limiting terms for the field properties of the phases ($\lim \phi_D/\phi_M = 0$; $\lim \phi_M/\phi_D = 0$) in equation (32) one obtains

$$\frac{\phi_D}{\phi_M} \ll 1 : \phi_C = \phi_M (1 - c_D)^{\frac{1 - \cos^2 a_D}{1 - F_D} + \frac{\cos^2 a_D}{2F_D}} \tag{44}$$

$$\frac{\phi_D}{\phi_M} \gg 1 : \phi_C = \phi_M (1 - c_D)^{\frac{\cos^2 a_D - 1}{F_D} + \frac{\cos^2 a_D}{1 - 2F_D}} \tag{45}$$

$(0 \leq c_D \leq 1; 0 \leq \cos^2 a_D \leq 1; 0 \leq F_D \leq 0.5)$.

2.7 *Porous materials*

Equation (44) provides already the model concept solution for this class of materials since for the bounds in the limiting case of pores ($\phi_2 = 0$ or $\phi_D = 0$; Fig. 6) substituting one phase (2 or D) makes all lower bound equations (1b, 2b, 3b in Fig. 6) disappear.

To understand as well as to solve this problem the model concept helps [189,190]: as has been pointed out earlier the microstructure-field property equation (32) for two-phase materials derived on the basis of the model concept provides the same

I. and II. order bound equations as the bound concept if the assumptions made in the bound concept are introduced into the model concept theory. This is why it is considered justifiable to use the microstructure- field property equation based on the model concept for trying to understand the effect of pores on the lower bounds as well as to derive the missing lower bound equations for porous materials via the model concept. Doing so it becomes immediately obvious why the lower bound equations fail in the case of pores. Usually pores can be described sufficiently well as spheroids (z = rotation axis, x = minor axis) and this has been done in the model concept. The derivation of bounds by that concept, however, results in lower bounds for porous materials with disc-shaped pores for which the relation $z/x \rightarrow 0$ applies, the solutions being obtained without preference either by $z \rightarrow 0$ or by $x \rightarrow \infty$.

Pores formed by $x \rightarrow \infty$, however, disintegrate the material - its field properties drop to zero at any porosity! To ask for the real instead of the fictitious disc-shaped - pore form, therefore, raises the question of the lower bound equations of porous materials.

The (model) microstructure-field property equation (44) for porous materials provides the effective field property ($\phi_P \doteq \phi_C$) as a function of the field property of the solid phase ($\phi_M \doteq$ field property of the nonporous material), the porosity ($P \doteq c_D$), pore shape (F_D), and pore orientation ($\cos^2\alpha_D$).

To answer the question as to the real pore shape in a practical situation, the powder technological factors which influence the formation of the pores must be considered.

In all sintering steps the driving force for materials transport is caused by the tendency to reduce the surface energy, this is the surface-to-volume ratio. To start the process it needs the activation energy for sintering (ΔG_S), which is provided by an external term transmitted as heat at elevated temperatures ($\Delta E_{ext} = \Delta Q$) and an internal term from the - external and internal - surface energy of the material ($\Delta E_{int} = \Delta G_{fg}^{Gr}$).

$$\Delta G_S = \Delta E_{ext} + \Delta E_{int} = \Delta Q + \Delta G_{fg}^{Gr} \tag{46}$$

Due to the "external" surface energy $(\Delta G_{fg}^{Gr\,ext})$ and the internal surface energy of the pores $(\Delta G_{fg}^{Gr\,int})$ the interface term in equation (46) becomes

$$\Delta G_{fg}^{Gr} = \Delta G_{fg}^{Gr\,ext} + \Delta G_{fg}^{Gr\,int} \tag{47}$$

with

$$\Delta G_{fg}^{Gr\,int} = N_p \cdot \overline{S_p} \cdot \gamma \tag{48}$$

(N_p = number of pores; S_p = average pore surface; and γ = specific surface energy, a temperature dependent materials quantity).

Since equations (32) and (44) refer to matrix phase microstructure the energy considerations focus on closed porosity.

There are two actions to be considered separately taking place by materials transport during sintering:

- the alteration of pore shape to reduce surface-to-volume ratio of the pores (reduction of internal surface energy at constant porosity)
- the reduction of overall porosity by the alteration of the number and size of the pores (shrinkage or densification $\triangleq$ reduction of internal and external surface energy)

Supposing diffusion to be the dominant mechanism of materials transport during sintering the pore shape alteration will start first because the activation energies for the three possible diffusion paths are [101]

$$\Delta G_{SD} < \Delta G_{ID} < \Delta G_{VD} \tag{49}$$

(ΔG_{SD} = activation energy for surface diffusion; ΔG_{ID} = activation energy for internal interface diffusion, e.g. grain boundary diffusion; ΔG_{VD} = activation energy for volume diffusion). This is why further considerations are focussed first on this step.

The volume (V_p) of spheroidal pores follows from

$$V_p = (\pi/6)zx^2 \tag{50}$$

whereas the surfaces (S_p) are given for lenticular pores (oblate spheroids: z/x > 1) by

$$S_p = \frac{\pi}{2}\left| x^2 + \frac{z^2}{(1-(z/x)^2)^{1/2}} \ln \frac{1+|1-(z/x)^2|^{1/2}}{z/x} \right| \tag{51}$$

and for egg-shaped pores (prolate spheroids: z/x > 1) by

$$S_p = \frac{\pi}{2}\left| x^2 + \frac{zx \arcsin\left(1-\frac{1}{(z/x)^2}\right)^{1/2}}{\left(1-\frac{1}{(z/x)^2}\right)^{1/2}} \right| \tag{52}$$

The state of minimum surface-to-volume ratio for pores and, therefore, minimum surface energy (ΔG_{fg0}^{Grint}) is obtained with spherical pores (z/x = 1). Normalizing the surface energy and surface at constant pore volume to that state provides

$$\Delta G_{fg}^{Grint}/\Delta G_{fg0}^{Grint} = S_p/S_{p0} = f(z/x) \tag{53}$$

which, using eqs. (50) and (51), results in the values given numerically in fig. 22. As the plot in fig. 23 demonstrates, changes in shape in the left region for small axial ratios cause large reduction in surface - and surface energy - ratios, respectively. The slope of the curve in that region is well approximated by the function

$$S/S_0 = 0.513\,(z/x)^{-0.662} \tag{54}$$

with high accuracy between $0.0001 < z/x < 0.1$ compared with the actual data given numerically and graphically (broad black line) in figs. 22, 23 (≤ 1 % deviation).

Heating up a porous material in a sintering process surface diffusion will start as soon as the heat transmitted to the material (ΔQ) together with the energy stored in the internal surfaces equals the activation energy for surface diffusion:

z/x	S_p/S_{p0}	z/x	S_p/S_{p0}
0.0005	79.3695	1	1
0.001	49.9999	1.01	1.00002
0.005	17.1022	1.1	1.0014
0.01	10.7778	1.5	1.0274
0.02	6.7985	2.0	1.0767
0.04	4.3017	2.5	1.1298
0.06	3.3036	3.0	1.1819
0.08	2.7487	3.5	1.2317
0.1	2.3906	4.0	1.2789
0.2	1.5988	5.0	1.3660
0.3	1.3129	10	1.7000
0.4	1.1729	20	2.1344
0.5	1.0954	50	2.8940
0.6	1.0503	100	3.6456
0.8	1.0092	200	4.5930
0.9	1.0021	1000	7.8539
0.95	1.0005	10000	16.9206
0.99	1.00002		
1	1		

Fig. 22: Numerical values of equation (53)

$$\Delta G_{SD} = \Delta Q + \Delta G_{fg}^{Gr\,int} \tag{55a}$$

At constant heat transmission the $\Delta G_{fg0}^{Gr\,int}$_term will now decrease by reduction of the surface-to-volume ratio of the pores where the axial ratio of an oblate pore for example increases. At the same time this process leads to

$$\Delta G_{SD} > \Delta Q + \Delta G_{fg}^{Gr\,int} \tag{55b}$$

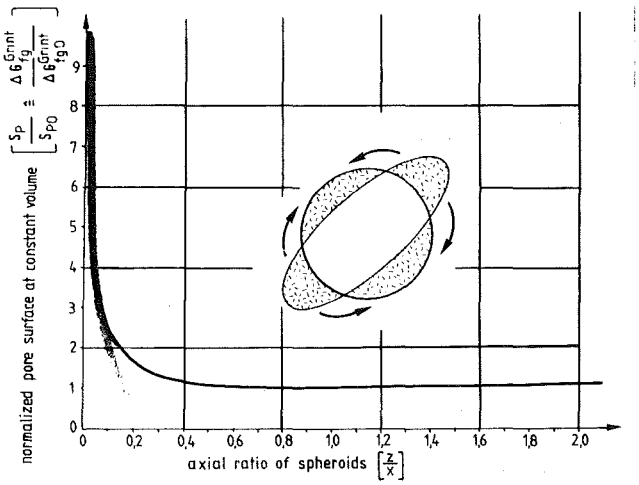

Fig. 23: Normalized pore surface and axial ratio.

and stops at a definite axial ratio of the pores. Increasing the temperature again equ. (55a) will be fulfilled again and the process runs - iteratively - until the "ideal" case - spherical pores - is obtained.

Under real technological conditions during isothermal sintering at elevated tem perature in practice, however, at least at the beginning the energy transmission will be high enough to fulfill equ. (46), so that shrinkage by volume diffusion and interface diffusion takes place parallel to surface diffusion, causing pore shape alteration. Under these circumstances it is (sintering) time which determines the pore shape that exists after stopping the process. However, since the energy release by pore shape change below axial ratios of $z/x \leq 0.1$ is extremely high (fig. 23) it is likely that in sintering processes spheroidal pore shape with axial ratios of $z/x \simeq 0.1$ may always be expected to be achieved under normal technological conditions. From this axial ratio, depending on the sintering conditions, the shape alteration process by vacancy transport (compare sketch, fig. 23) will be slowed down and will finally stop between lenticular ($z/x \ll 1$) and spherical pores ($z/x = 1$) depending on sintering time.

Investigating the slope of the S_i/S_{i0}-z/x curve by its derivation $(d(S_i/S_{P0})/d(z/x))$, it becomes obvious that energy changes $(d(\Delta G_{fg}^{Gr\,int}/\Delta G_{fg0}^{Gr\,int}) = d(S_p/S_{P0}))$, related to form alterations at axial ratios $z/x > 1$, correspond to those existing in the axial

ratio region $0.1 < z/x < 1$. This is why quasi-cylindrical pores (pore channels) must be considered to be as stable as lenticular pores ($0.1 < z/x < 1$).

If therefore $z/x = 0.1$ is considered to be the minimum axial ratio to be reached in real sintering procedures, the respective minimum shape factor for pores is $F_D = 0.0696$ (compare fig. 13).

Using this shape factor together with the respective orientation factors for I. order bounds ($\cos^2\alpha_D = 0$ or $\cos^2\alpha_D = 1$), II. order bounds ($\cos^2\alpha_D = 1/3$) and III. order bounds ($\cos^2\alpha_D = 1/3$) the lower bound equations for porous sintered materials follow from equation (44) as given in fig. 24. - It must be emphasized and not be overlooked, that the equations given in fig. 24 exceptionally refer to pores formed by a history including sintering. Otherwise - as for porosity in pellets pressed only for instance, equations (56), (57) and (58) do not apply due to the missing surface diffusion process. In these cases one has to go back to equations (1) - (3) assuming a very small but definite conductivity of the pores ($\lim \phi_D = \lim \phi_P \neq 0$; e.g. thermal conductivity of the gas filling the pores).

The equations for special cases of pore characteristics according to equations (44,45) are given in fig. 25.

	lower bounds	lower bounds
I. order	$\Phi_{I\,P} = \Phi_M (1-P)^7$ (56a)	$\phi_P^I = \Phi_M (1-P)$ (56b)
II. order	$\Phi_{II\,P} = \Phi_M (1-P)^3$ (57a)	$\phi_P^{II} = \Phi_M \frac{2(1-P)}{2+P}$ (57b)
III. order	$\Phi_{III\,P} = \Phi_M (1-P)^3$ (58a)	$\phi_P^{III} = \Phi_M (1-P)^{3/2}$ (58b)

Fig. 24: Bound equations of different order for porous materials (F = field property; P = porosity (fractional); ϕ_P = effective field property of porous material; ϕ_M = conductivity of nonporous material; $\phi_{I,II,III}$ = lower bounds for the effective field property; $\phi^{I,II,III}$ = upper bounds for effective field property

spherical pores	$\Phi_P = \Phi_M (1-P)^{3/2}$	(59)
cylindrical pores statistically directed to the field direction (pore channels in isotropic materials)	$\Phi_P = \Phi_M (1-P)^{5/3}$	(60a)
cylindrical pores oriented perpendicular ($\perp$) and parallel ($\parallel$) to the field direction (oriented pore channels)	$\Phi_{P\perp} = \Phi_M (1-P)^2$ $\Phi_{P\parallel} = \Phi_M (1-P)$	(60b) (60c)

Fig. 25: Bound equations for special pore structures (F = field property;P = porosity (fractional); Φ_P = effective field porosity of porous material; Φ_M = conductivity of nonporous material; $\Phi_{I,II,III}$ = lower bounds for the effective field property; $\Phi^{I,II,III}$ = upper bounds for the effective field property

2.8 *Extension of the theory from two-phase to multi-phase materials*

The previous theoretical treatment of the interrelationships between microstructure and field properties has been restricted to two-phase materials. In order to treat materials with more than two phases the principle of the selfconsistent scheme is applied once again.

Considering, for instance, a three phase material, the effective field property is determined first for a combination of two of its phases. The resulting two-phase material then is considered as a "fictitious (single) substituting phase", possessing the - previously calculated - effective field property and being combined now with the third phase of the three-phase system. Continued treatment assumes an apparently two-phase material formed by the fictitious substitution phase and the third phase. Applying the bound concept with that procedure to a three-phase material (phases α, β, γ; assumed phase concentrations $c_\alpha = 70$, $c_\beta = 20$, $c_\gamma = 10$ vol.%; assumed field properties of the phases $\Phi_\alpha : \Phi_\beta : \Phi_\gamma = 1000 : 10 : 1$) no preference may be given to one combination of the three possibilities in the first step: $\alpha\beta$; $\beta\gamma$; $\gamma\alpha$. According to these three different but equally justified fic-

titious substitution phases six effective properties result ($\Phi_{\alpha\beta}^{I}$, $\Phi_{\alpha\beta I}$; $\Phi_{\beta\gamma}^{I}$, $\Phi_{\beta\gamma I}$; $\Phi_{\gamma\alpha}^{I}$, $\Phi_{\gamma\alpha I}$). Combining each of them with the respective third phase 12 bound values follow, one of which provides a maximum field property and another one providing a minimum field property value. This couple bounds all other possible values of the three phase material. With the values for the assumed three-phase material given above one obtains the results given in fig. 26.

$\alpha\beta$	$\Phi_{I\alpha\beta} = 43.5$	$\Phi_{I\alpha\beta\gamma} = 8.3$	
		$\Phi^{I}_{\alpha\beta\gamma} = 39.2$	
	$\Phi^{I}_{\alpha\beta} = 782.2$	$\Phi_{I\alpha\beta\gamma} = 9.9$	upper bound of the three-phase material:
		$\Phi^{I}_{\alpha\beta\gamma} = 704.1$	704.1
$\beta\gamma$	$\Phi_{I\beta\gamma} = 2.5$	$\Phi_{I\beta\gamma\alpha} = 8.1$	
		$\Phi^{I}_{\beta\gamma\alpha} = 700.7$	
	$\Phi^{I}_{\beta\gamma} = 8.0$	$\Phi_{I\beta\gamma\alpha} = 26.3$	
		$\Phi^{I}_{\beta\gamma\alpha} = 702.4$	
$\gamma\alpha$	$\Phi_{I\gamma\alpha} = 4.3$	$\Phi_{I\gamma\alpha\beta} = 4.9$	4.9
		$\Phi^{I}_{\gamma\alpha\beta} = 5.5$	lower bound of the three phase material
	$\Phi^{I}_{\gamma\alpha} = 870.3$	$\Phi_{I\gamma\alpha\beta} = 47.8$	
		$\Phi^{I}_{\gamma\alpha\beta} = 698$	

Fig. 26: I. Order bound determination for three-phase materials.

In the first column the possible two-phase combinations are listed followed by the respective I order bounds (second column, fig. 26). In the third column of fig. 26

these bounds for each substitution phase are correlated with the field property of the respective third phase providing altogether six upper and six lower bounds, from which, by comparison, the ultimate (I. order) upper and lower bounds for the three phase material come out (fig. 26, last column). As the comparison of the maximum variable region between the pure phase field-properties ($\Delta\phi_{max} = \phi_\alpha - \phi_\gamma = 999$) and the region between the bounds for the three phase materials demonstrates, even I. order bounds, in this case, reduce the region of variation remarkably (~ 30 %). This procedure may be applied also to more than three phases and higher order bounds, if more than only one microstructural parameter (the number of phases to be three) has been fixed. Finally in the case that even detailed information is available about the microstructure (compare fig. 4), then an appropriate treatment of the microstructure-field property relationship is also possible by the model concept.

Assuming the three-phase material consists of two solid phases (M,D) and one gaseous phase (P, ≙ pores), which is included in the solid matrix phase (M), equation (44) provides

for the effective field property of the porous matrix phase (1st step)

$$\phi_{MP} = \phi_M (1-P)^{\frac{\cos^2\alpha_P - 1}{F_P} + \frac{\cos^2\alpha_P}{2F_P}} \tag{61}$$

for the effective field property of the three-phase material (2nd step)

$$\phi_C = \phi_{MP} (1-c_D)^{\frac{\cos^2\alpha_D - 1}{F_D} + \frac{\cos^2\alpha_D}{2F_D}} \tag{62a}$$

$$\phi_C = \phi_M (1-P)^{\frac{\cos^2\alpha_P - 1}{F_P} + \frac{\cos^2\alpha_P}{2F_P}} (1-c_D)^{\frac{\cos^2\alpha_D - 1}{F_D} + \frac{\cos^2\alpha_D}{2F_D}} \tag{62b}$$

(ϕ_M = field property of the compact matrix phase; ϕ_{MP} = field property of the porous matrix phase; ϕ_C = field property of the three-phase material; P = porosity as fraction; c_D = volume content of the inclusion phase; F_P = shape factor of the pores; F_D = shape factor of inclusion phase; $\cos^2\alpha_P$ = orientation factor of the pores; $\cos^2\alpha_D$ = orientation factor of the inclusion phase)

As can be concluded easily by changing the sequence of M, D and P it does not matter for the final form of equation (62b), whether one combines phase M and phase D in the first step instead of phase M and phase P. This treatment holds also true for more than three phases offering the application of the model concept also to multiphase materials.

3. *The determination of microstructural parameters by quantitative microstructural analysis*

3.1 Microstructural analysis

According to fig. 4 and equation (32) a total of 5 parameters are required in order to take complete quantitative account of the microstructure of a multiphase material in microstructure-field property equations. Two of them are implicit microstructural parameters (number of phases, type of microstructure), which govern the type of the microstructure-field property equation by appropriate suppositions but do not appear explicitly. Explicit microstructural parameters, however, are defined as factors in the equation (concentration factor, shape factor, orientation factor). - All these parameters are determined by means of quantitative microstructural analysis. The principle of this analysis is illustrated in fig. 27. Working from prepared sections through the material, micrographs are produced optically and magnified, reproduced photographically and/or electronically, magnified again and measured. The data measured in a flat plane are converted to three dimensional microstructural parameters by means of stereological equations in a primary computer program and these parameters are then used in other computer programs for determining the required microstructural factors and properties of the two-phase materials.

3.2 Implicite microstructural parameters: number of phases and type of microstructure

Determination of the data on the number of phases (fig. 4), is particularly simple, since they can be seen directly in magnified microstructural images with adequate contrast.

The data on the distinction between matrix and interconnecting microstructures is obtained from measurements of the following parameters in the micrograph:

- total number of inclusion particles (N_E),
- number of inclusion particles not making contact with other particles of the inclusion phase (N_0),

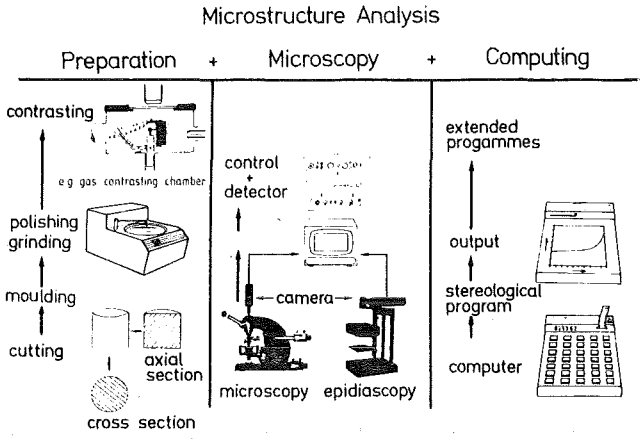

Fig. 27: Sequence of quantitative microstructural analysis (schematic) [24].

- number of contact positions between particles of the inclusion phase (n_k) related to the total number of included particles.

by means of the correlation [53]:

$$\frac{2n_k \cdot N_E}{N_E - N_0} - 1 = K \tag{63}$$

where the degree of chain formation (K) is a measure of the mean number of contacting positions with adjacent particles per particle [101,243]. The probability of interconnecting microstructure being present is shown in fig. 28 as a function of the degree of chain formation. When there is a small mean number of contacting adjacent particles, the probability of interconnecting microstructure occurring is low (e.g. zero for $K \leq 1$). This probability increases with increasing degree of chain formation from "pure" matrix ($K \leq 1$) to "pure" interconnecting microstructure ($K \geq 4$).

In quantitative microstructural analysis the precise separation between agglomerated particles and nonagglomerated particles simply by measurement is usually not possible. The analysis therefore includes

- the determination of mean cross section areas per particle in microstructures containing very low inclusion phase particles. In this case agglomeration may be neglected.
- the determination of mean cross section areas per particle in microstructures containing increasing concentration of inclusion phase particles.
- the probabilistic calculation of the terms of equation (36) from the above mentioned measurements.

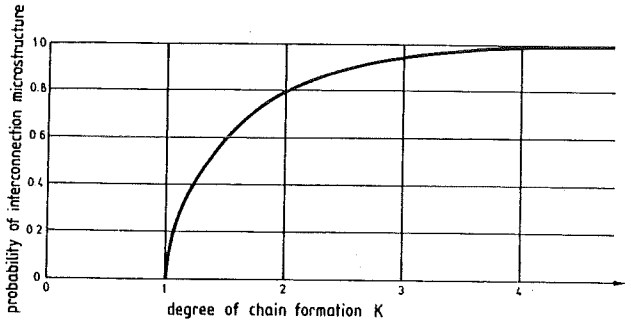

Fig. 28: Distinction of types of microstructure by the degree of chain formation.

The formation of an interconnecting microstructure will be reflected for example in field property plots versus phase concentration as already demonstrated in fig. 20, where within the hatched region the interconnecting microstructure increases starting from about 10 vol.% metal with increasing metal concentration. In this case the degree of chain formation between metal particles is considered. But also from the other side of the diagram the interconnecting microstructure increases starting from about 30 vol.% metal with decreasing metal content. In this case the degree of chain formation between ceramic particles is considered. The degree of chain formation becomes four at different phase concentrations (e.g. 15 vol.% metal $\leq c \leq$ 25 vol.% metal) marking the closer region in which "perfect" interconnecting microstructure exists. - The position of this region is variable and depends on the powder characteristics of the two phases and the materials technology. In fig. 29 it is pointed out how the change of the type of microstructure is expressed even in such a technological parameter as the pressed density of

powder technologically prepared cermets plotted versus the concentration of the phases.

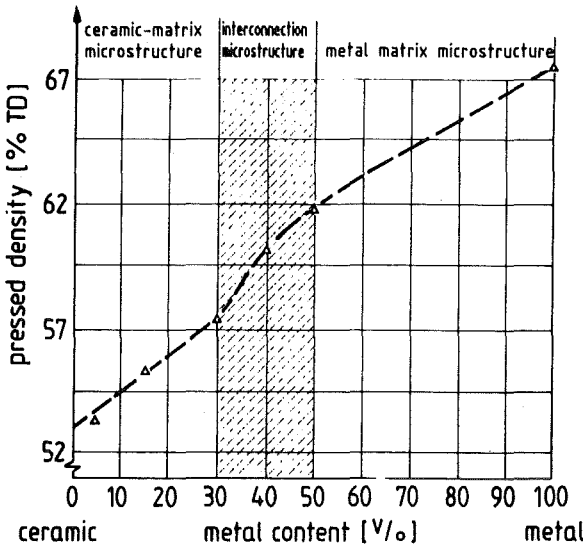

Fig. 29: Expression of microstructural types in density plots versus phase concentration (TD = theoretical density).

3.3 Explicit mictrostructural parameters: Concentration, shape and orientation factors

The three microstructural factors quantitatively characterising the concentration, shape and orientation of inclusion phase particles of a two-phase material are defined by the derivation of equation (32). They are determined for a real material by measurements made on two-dimensional micrographs, from which the microstructural factors applicable to three-dimensional material can be calculated by means of stereological equations.

The phase concentration factor follows as phase volume content directly from the mean value of the area content of the phases in micrographs originating from sections cut statistically through the material (Delesse principle) [265].

In accordance with equation (9) and fig. 13, the shape factor is a function of the ratio of the rotation axis (axis of revolution) and the minor axis of the spheroid by which the real particles of the inclusion phase in the model are replaced. The fact,

that this "spatial" axial ratio (z/x) can be determined from the (mean) "planar" axial ratio of the sectional ellipses of the spheroids substituting for the real particles of the inclusion phase by means of stereological equations, was a crucial factor in the choice of the spheroid model for characterising real material.

In practice one proceeds as follows: the area and periphery are measured for each section of an (irregularly shaped) particle of the inclusion phase in a two-dimensional micrograph and from this the axial ratio is calculated for the sectional ellipse with the same area-to-periphery ratio as the measured sectional area of the particle (fig. 30) [199,215]. Since one can form the planar axial ratios not only from "minor axis (b') to major axis (a')" but also from "major axis to minor axis", one obtains in each case two mean values of measured axial ratio of sectional ellipses:

$$\frac{\sum_{1}^{n} \frac{a'}{b'}}{n} = \overline{\left|\frac{a'}{b'}\right|} \tag{64a}$$

$$\frac{\sum_{1}^{n} \frac{b'}{a'}}{n} = \overline{\left|\frac{b'}{a'}\right|} \tag{64b}$$

For each of these axial ratios, the stereological equations provide an axial ratio for each oblate spheroid and one for each prolate spheroid [114,199,215,244], hence a total of 4 "spatial" axial ratios |z/x|:

$$\overline{\left|\frac{b'}{a'}\right|} = \left|\frac{z}{x}\right|_{=} \frac{\arcsin\sqrt{1-\left|\frac{z}{x}\right|_{=}^{2}}}{\sqrt{1-\left|\frac{z}{x}\right|_{=}^{2}}} \tag{65a}$$

$$\overline{\left|\frac{b'}{a'}\right|} = \frac{1}{2} + \frac{1}{2\left|\frac{z}{x}\right|_{\parallel}^{2}\sqrt{1-\frac{1}{\left|\frac{z}{x}\right|_{\parallel}^{2}}}} \ln\left(1+\sqrt{1-\frac{1}{\left|\frac{z}{x}\right|_{\parallel}^{2}}}\left|\frac{z}{x}\right|_{\parallel}\right) \tag{65b}$$

$$\overline{\left|\frac{a'}{b'}\right|} = \frac{1}{2} + \frac{\arcsin\sqrt{1-\left|\frac{z}{x}\right|_{=}^{2}}}{2\left|\frac{z}{x}\right|\sqrt{1-\left|\frac{z}{x}\right|_{=}^{2}}} \tag{66a}$$

$$\left|\frac{a'}{b'}\right| = \frac{1}{\sqrt{1 - \frac{1}{\left|\frac{z}{x}\right|_1^2}}} \ln\left(1 + \sqrt{1 - \frac{1}{\left|\frac{z}{x}\right|_1^2}} \cdot \left|\frac{z}{x}\right|_1\right) \qquad (66b)$$

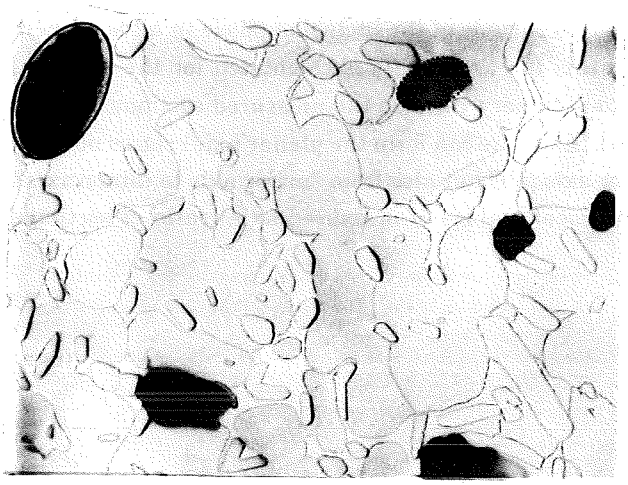

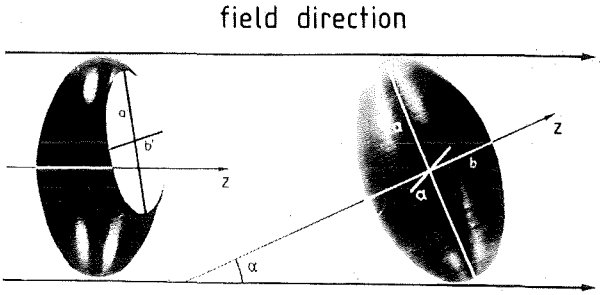

Fig. 30: Determination of axial ratios of sectional ellipses.

These equations are shown graphically in fig. 31 [199,215]. In a notional experiment, let it now be assumed that there is a two-phase material with identical prolate spheroidal particles of inclusion phase. In the sections cut statistically through it, sectional ellipses then appear whose measurement provides the two axial ratios in accordance with equation (64). From equations (65) and (66) then follow 4 axial ratios of spheroids, of which only two, namely those for prolate spheroids corresponding to the assumed model material must be identical, whilst the associated two axial ratios for oblate spheroids are not. For quantitative

microstructural analysis of a real material, this means that of the 4 axial ratios obtained from measurements for substitute spheroids, only two are approximately equal in each case for the same type of spheroid (prolate or oblate), or lie closer together than the other two. The spheroid corresponding to the approximately equal axial ratios would then be best suited for a model characterising the real particles of the inclusion phase. - In these real cases, however, where the differences between the spatial axial ratios will be so small (see fig. 31 dotted lines) that no selection is possible for practical purposes, one may either determine a mean value from each pair of axial ratios for each type of spheroid, thus obtaining two shape factors in accordance with equation (10) or fig. 13 and the corresponding bounding curves or one averages all 4 axial ratios obtaining a single mean shape factor.

In order to test the stereological equations for determing axial ratios a model experiment has been made as shown in fig. 32. Pills of equal prolate shape have been included in a resin matrix as used for mounting in metallography. Since their spatial axial ratio was known by measurement the mean axial ratio of their ellipses in sections of plane can be determined by equations (65b) and (66b) or fig. 31. Now measurements as described above have been made to determine the experimentally mean axial ratios in sections of plane. From them the most likely mean spatial axial ratio has been calculated by equations (65) and (66). In fig. 33 the values obtained from measurements are compared with the predetermined nominal values [200].

In accordance with the derivation of equation (32), the orientation factor is the cosine squared of the angle formed by the field strength gradient direction and the rotation axis of spheroids of identical form and size substituting the real particles in the model (see fig. 10). Like the shape factor, this can also be calculated from axial ratios determined by quantitative microstructural analysis. To derive the relationship, one proceeds from the following equations [114]:

for prolate spheroids

$$\left|\frac{b'}{a'}\right|_A = \sqrt{\cos^2\alpha_A + \frac{\sin^2\alpha_A}{|z/x|^2}} \qquad (67a)$$

for oblate spheroids

$$\left|\frac{a'}{b'}\right|_A = \sqrt{\cos^2\alpha_A + \frac{\sin^2\alpha_A}{|z/x|^2_=}} \qquad (68a)$$

or after transformation

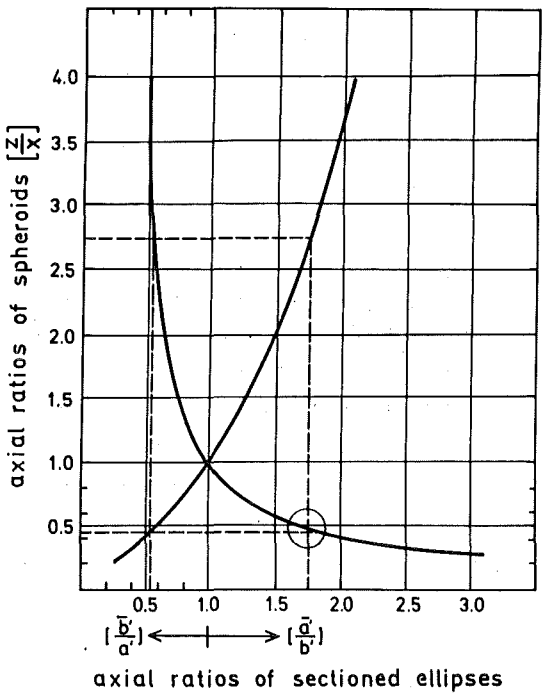

Fig. 31: "Spatial" axial ratio of spheroids as a function of "plane" axial ratio of sectional ellipses.

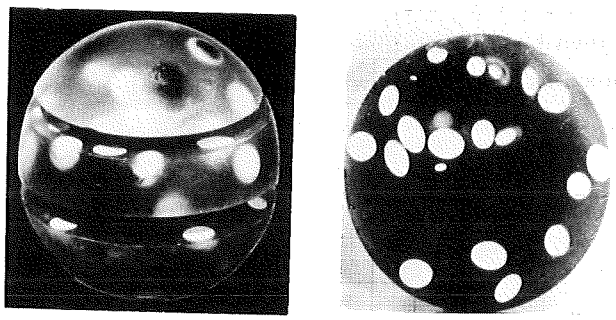

Fig. 32: Spheroids modelled by pills in a resin matrix phase.

	Quantity	Nominal	Measured	Rel. Error(%)
Mean axial ratio in the plane	$(\overline{a'/b})$	1,2494	1,2027	3,88
	$(\overline{b/a'})$	0,8119	0,8541	5,19
Volume content	V_V	0,2180	0,2212	1,46
Mean axial ratio	$(\overline{z/x})$	1,1785	1,2001	1,83

Fig. 33: Comparison of nominal and experimental axial ratios of spheroidal inclusions.

$$\cos^2\alpha_A = \frac{\left|\frac{z}{x}\right|_{\parallel}^2 \overline{\left[\frac{b'}{a'}\right]}_A^2 - 1}{\left|\frac{z}{x}\right|_{\parallel}^2 - 1} \qquad (67b)$$

and

$$\cos^2\alpha_A = \frac{\left|\frac{z}{x}\right|_{=}^2 \overline{\left[\frac{a'}{b'}\right]}_A^2 - 1}{\left|\frac{z}{x}\right|_{=}^2 - 1} \qquad (68b)$$

For these equations, the ("spatial") axial ratio of the spheroid is determined with equations (65) and (66) from the mean axial ratios of the sectional ellipses $(\overline{\left[\frac{b'}{a'}\right]}, \overline{\left[\frac{a'}{b'}\right]})$, which were measured in sections cut statistically through the material. On the other hand, the mean axial ratios of the sectional ellipses $(\overline{\left[\frac{b'}{a'}\right]}_A, \overline{\left[\frac{a'}{b'}\right]}_A)$ contained in the equations themselves, are those measured in sectional planes (A) perpendicular to the field direction (see fig. 34).

The selection procedure for evaluating a mean spatial axial ratio, as described above for the determination of the "singular" shape factor specifies which of the two equations 67b or 68b is to be used for evaluating the orientation factor. If, on the other hand, one considers the mean axial ratios for the prolate and oblate spheroids to be equally justifiable, then one obtains two - equally justifiable - orientation factors and hence one more corresponding bounding curve of higher order.

The orientation factor in accordance with equations 67 or 68 can be optimized by an additional measuring requirement. Fundamentally, of course, one may

determine the orientation of the substituted spheroid for each spatial direction, by determining the axial ratios of the sectional ellipses in all three sectional planes perpendicular to the three spatial directions (see fig. 34) and hence

$$\overline{\left|\frac{b'}{a'}\right|}_A \rightarrow \cos^2\alpha_A \qquad \overline{\left|\frac{b'}{a'}\right|}_B \rightarrow \cos^2\alpha_B \qquad \overline{\left|\frac{b'}{a'}\right|}_C \rightarrow \cos^2\alpha_C \tag{69}$$

The following mathematical boundary condition then applies

$$\cos^2\alpha_A + \cos^2\alpha_B + \cos^2\alpha_C = 1 \tag{70}$$

This boundary condition, however, is only fulfilled on the ideal model, whilst for the real case the following will apply:

$$\sum_{i=A}^{C} \cos^2\alpha_i \leqq 1 \tag{71}$$

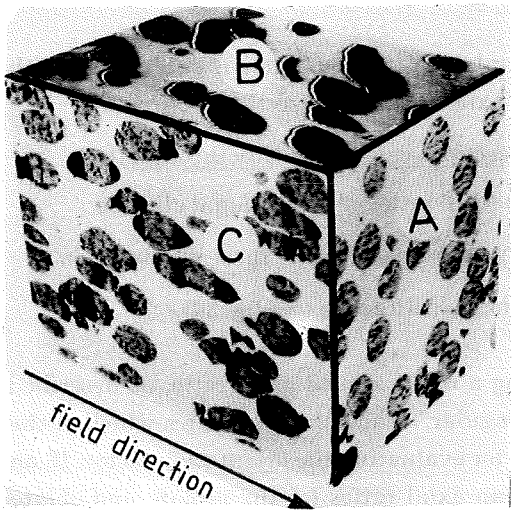

Fig. 34: Orientation factor: model explanation.

In order to adjust the model material to the real case, one sets:

$$Y\cos^2\alpha_A + Y\cos^2\alpha_B + Y\cos^2\alpha_C = Y \cdot X = 1 \tag{72}$$

with

$$Y\cos^2\alpha_A = \cos^2\alpha_D \tag{73}$$

and

$$Y = \frac{1}{\cos^2\alpha_A + \cos^2\alpha_B + \cos^2\alpha_C} \tag{74}$$

and analogous to equations (67b) and (68b):

$$\cos^2\alpha_B = \frac{\left|\frac{z}{x}\right|_{\parallel}^2 \left|\overline{\frac{b'}{a'}}\right|_B^2 - 1}{\left|\frac{z}{x}\right|_{\parallel}^2 - 1} \tag{75a}$$

$$\cos^2\alpha_B = \frac{\left|\frac{z}{x}\right|_{\parallel}^2 \left|\overline{\frac{a'}{b'}}\right|_B^2 - 1}{\left|\frac{z}{x}\right|_{=}^2 - 1} \tag{75b}$$

$$\cos^2\alpha_C = \frac{\left|\frac{z}{x}\right|_{\parallel}^2 \left|\overline{\frac{b'}{a'}}\right|_C^2 - 1}{\left|\frac{z}{x}\right|_{\parallel}^2 - 1} \tag{76a}$$

$$\cos^2\alpha_C = \frac{\left|\frac{z}{x}\right|_{=}^2 \left|\overline{\frac{a'}{b'}}\right|_C^2 - 1}{\left|\frac{z}{x}\right|_{=}^2 - 1} \tag{76b}$$

From equation (74) together with equations (67b), (75a) and (76a) follows

$$Y = \frac{\left|\frac{z}{x}\right|_{\parallel}^2 - 1}{\left|\frac{z}{x}\right|_{\parallel}^2 \left\{\left|\overline{\frac{b'}{a'}}\right|_A^2 + \left|\overline{\frac{b'}{a'}}\right|_B^2 + \left|\overline{\frac{b'}{a'}}\right|_C^2\right\} - 3} \tag{77}$$

and - also from equation (74) but with equations (68b), (75b) and (76b) follows

$$Y = \frac{\left|\frac{z}{x}\right|_{=}^2 - 1}{\left|\frac{z}{x}\right|_{=}^2 \left\{\left|\overline{\frac{a'}{b'}}\right|_A^2 + \left|\overline{\frac{a'}{b'}}\right|_B^2 + \left|\overline{\frac{a'}{b'}}\right|_C^2\right\} - 3} \tag{78}$$

The orientation factor which can be determined from analytical measurements of microstructure results then from equations (67), (68), (77), (78) and (73):

$$\cos^2\alpha_D = \frac{\left|\frac{z}{x}\right|_{\parallel}^2 \overline{\left|\frac{b'}{a'}\right|}_A^2 - 1}{\left|\frac{z}{x}\right|_{\parallel}^2 \left\{\overline{\left|\frac{b'}{a'}\right|}_A^2 + \overline{\left|\frac{b'}{a'}\right|}_B^2 + \overline{\left|\frac{b'}{a'}\right|}_C^2\right\} - 3} \tag{79}$$

$$\cos^2\alpha_D = \frac{\left|\frac{z}{x}\right|_{=}^2 \overline{\left|\frac{a'}{b'}\right|}_A^2 - 1}{\left|\frac{z}{x}\right|_{=}^2 \left\{\overline{\left|\frac{a'}{b'}\right|}_A^2 + \overline{\left|\frac{a'}{b'}\right|}_B^2 + \overline{\left|\frac{a'}{b'}\right|}_C^2\right\} - 3} \tag{80}$$

Since for example for a model material with statistical orientation of the inclusion phase particles

$$\overline{\left|\frac{b'}{a'}\right|}_A = \overline{\left|\frac{b'}{a'}\right|}_B = \overline{\left|\frac{b'}{a'}\right|}_C \tag{81}$$

or

$$\overline{\left|\frac{a'}{b'}\right|}_a = \overline{\left|\frac{a'}{b'}\right|}_B = \overline{\left|\frac{a'}{b'}\right|}_C \tag{82}$$

must apply, an orientation factor of

$$\cos^2\alpha_D = \frac{1}{3}$$

follows from equation (79) and (80), as expected for an isotropic material (compare page 21).

It might be mentioned in this context that an isotropic material always refers to that orientation factor, but that this orientation factor is not exclusively representative for an isotropic microstructure. It is possible to realize that special orientation factor also by definitely oriented microstructures ($\alpha_D \approx 55°$), which means, according to theory, that the field property of an unique anisotropic material should be identical with that of the same but isotropic material. Further theoretical treatment and experimental verification of this result is desired.

In general, however, as the derivation demonstrates, the microstructural factors, which according to equation (32) quantitatively correlate the microstructure of a two-phase material with its field properties, can completely be determined by quantitative microstructural analysis.

4. *Comparison between calculated and measured field properties in dependance on microstructure*

4.1 Two phase metals

Generally the comparison between measured and calculated values will start from least specified microstructures - concerning I. order bounds - and move gradually to more and more defined microstructures - say higher order bounds and "singular" values of field properties [201].

If, in the case of a metallic material, nothing more is known about its microstructure than the number of phases (compare fig. 4) to be two, then the experimental values have only to fit into first order bounds (equation (1)). As pointed out in figs. 35, 36, 37 and 38 these expectations come true, indeed, for the electrical conductivity of two-phase metal systems [201].

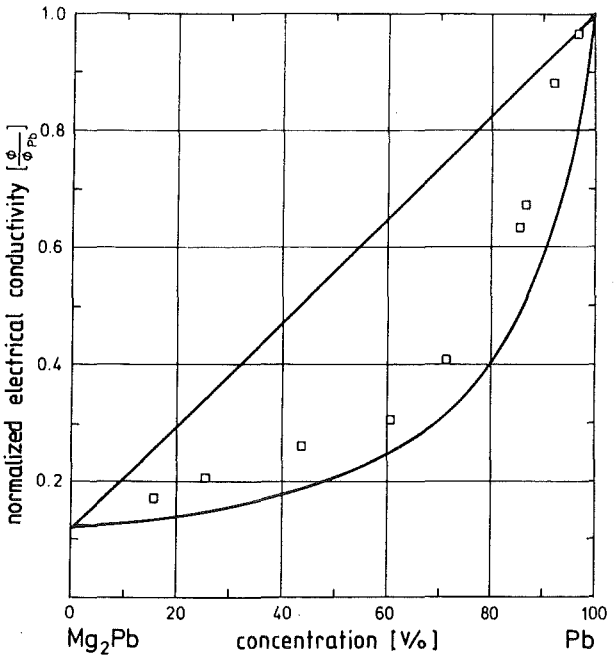

Fig. 35: Electrical conductivity of Mg_2Pb-Pb metal (□) at room temperature [150] and I. order bounds (——).

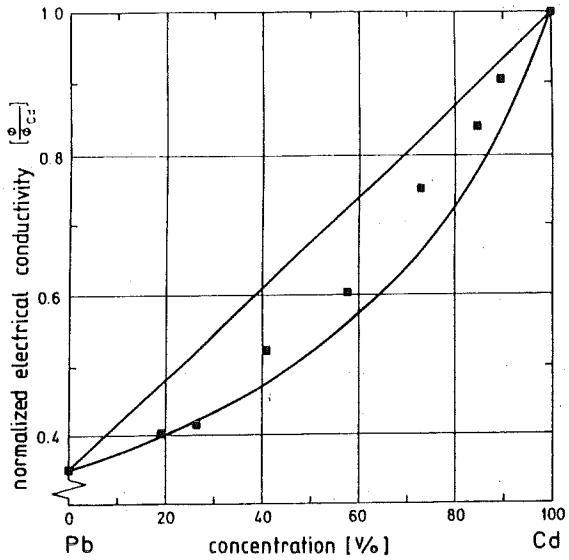

Fig. 36: Electrical conductivities of Cd-Pb metal (■) at room temperature [150] and I. order bounds (——).

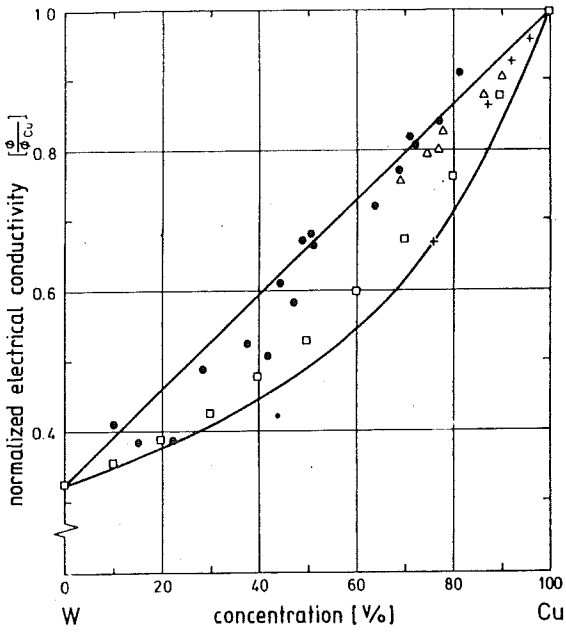

Fig. 37: Electrical conductivities of Cu-W metal (● □ + Δ) at room temperature [73,120,134,242] and I. order bounds (——).

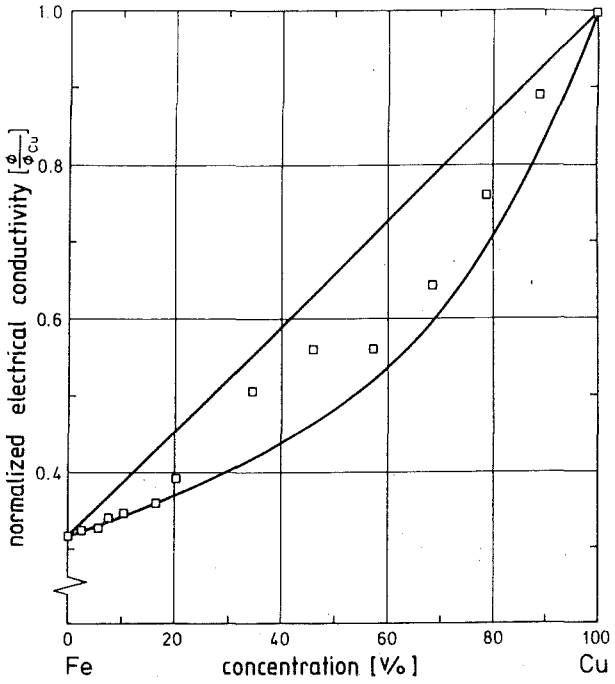

Fig. 38: Electrical conductivity of Cu-Fe metal (□) at room temperature [150] and I. order bounds (——).

Due to the fact, that, from theory, I. order bounds are ultimate bounds it is also possible conversely to confirm theoretical values by experimental data

- either to test the reliability of measured field properties of two-phase materials
- or to conclude about the bonding between the phases.

If the premise is fulfilled that bonding exists between the two phases then all measured field properties need to fit into the I. order bounds. For experimental values which lie above the upper I. order bound, as in fig. 39 for the thermal conductivity, either the accuracy of measurement for the values themselves is not sufficient or the field properties of the pure phases governing the bounds are not correct. If, for instance, the conductivity of tungsten would be somewhat higher more measured values of the two-phase material would be bounded by the curves.

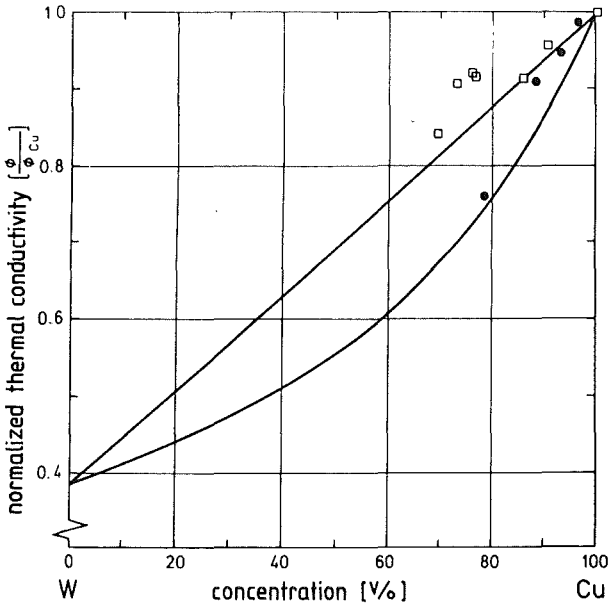

Fig. 39: Thermal conductivity of Cu-W-metal (□ ●)at room temperature [73, 120] and I. order bounds (——).

In figs. 40, 41 and 42 some measured values are placed below the lower bound. Assuming bonding exists then the same reasons may explain it as given for fig. 39. But taking into account nonbonding between the phases the I. order bounds in fig. 40, for example, then have to refer to either (quasi-) porous bismuth or (quasi-porous) tin (hatched regions). These bounds are superimposed in fig. 40 to the I. order bounds for the Bi-Sn-system. Since all measured values fit into the hatched region for porous materials it is reasonable to assume a lack of bonding between the phases as a possible explanation.

As the example demonstrates microstructure-property correlations may also be a tool to investigate indirectly the bonding behaviour between different phases.

Knowing that the material is two-phased and isotropic II. order bounds (equ. 2) apply to describe experimental field properties. Obviously these bounds will come closer with decreasing difference in the field properties of the pure phases, as the comparison for the electrical and thermal conductivity of two-phase isotropic

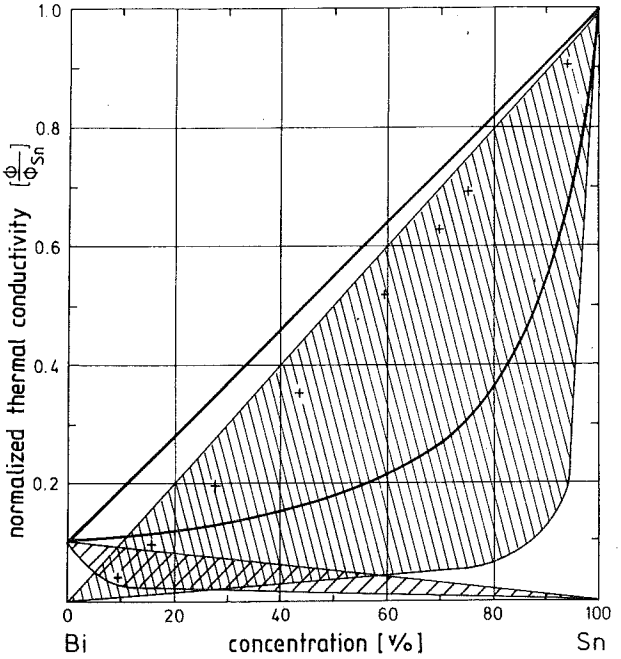

Fig. 40: Thermal conductivity of Bi-Sn metal (+) at room temperature [150], respective I. order bounds (—) and I. order bounds for porous bismuth and porous tin (hatched region).

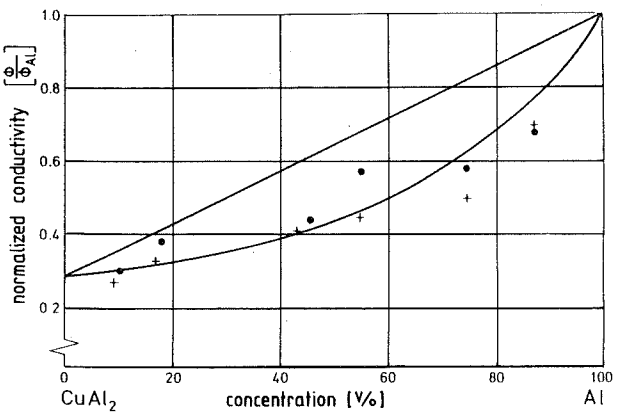

Fig. 41: Electrical (+) and thermal (●) conductivity of Al-$CuAl_2$ metal at room temperature [5] and I. order bounds (—).

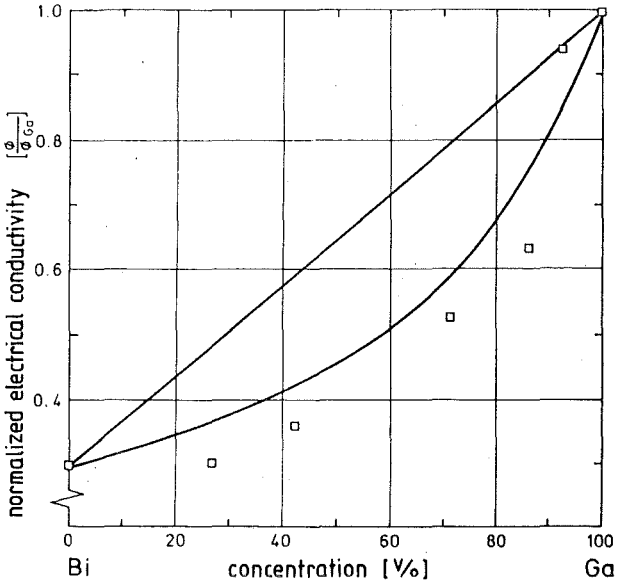

Fig. 42: Electrical conductivity of Bi-Ga metal (□) at room temperature [166] and I. order bounds (—).

metals with II. order bounds in fig. 43, 44, 45 and 46 demonstrates [201] and also for steel and cast iron considered later (fig. 80) together with the composites due to their carbide phase.

Bounds come closer and closer by increasing microstructural information ending up finally in "singular" curves of field properties versus phase concentration. The measured values in fig. 47, for instance, refer to Ag-Fe specimens, in which the matrix phase changes but spherical geometry of the inclusion phase particles remains. In that case equ. (40) provides a lower bound if iron forms the matrix but delivers upper bound values for the silver matrix phase.

Additionally one part of these Ag-Fe specimens has been cold worked by drawing which led to a fibre-like microstructure, where the fibres are parallel oriented with the drawing direction. Measuring electrical conductivities in this direction the respective theoretical curve follows from equ. (43). - Summarizing both the non-coldworked and coldworked Ag-Fe specimens in one diagram, all measured values should be bounded by the upper curve following from equ. (43) and the lower curve given by equ. (40) for Fe matrix phase [201]. As fig. 47 brings out, this - indeed - is the case.

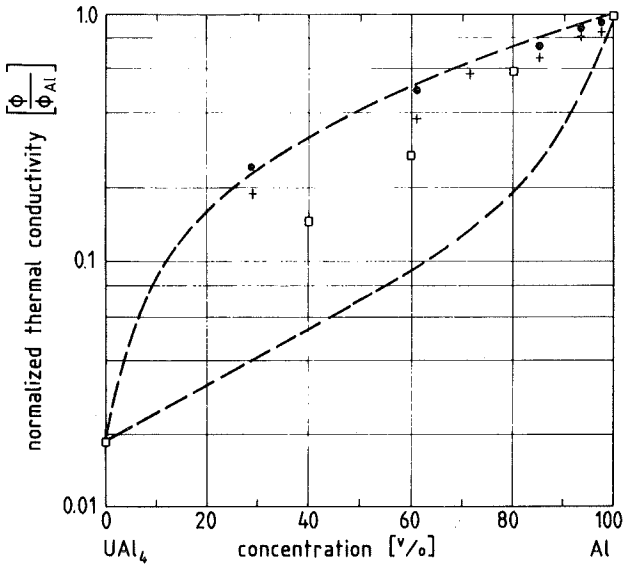

Fig. 43: Thermal conductivity of Al-UAl_4 metal (●+□) at 366 K [124,125] and II. order bounds (----).

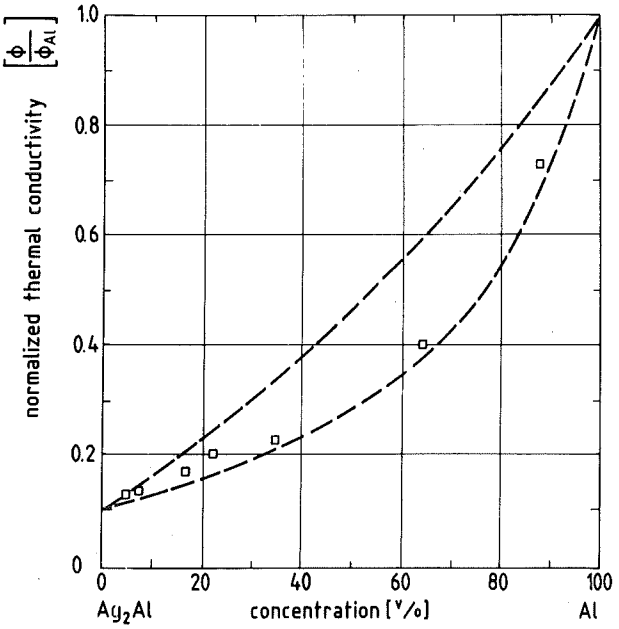

Fig. 44: Thermal conductivity of Ag_2Al-Al metal (□) at room temperature [150] and II. order bounds (----).

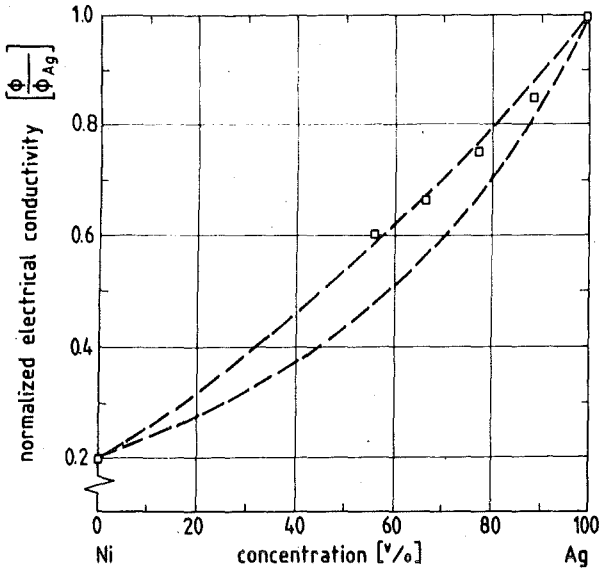

Fig. 45: Electrical conductivity of Ag-Ni metal (□) at room temperature [242] and II. order bounds (-----).

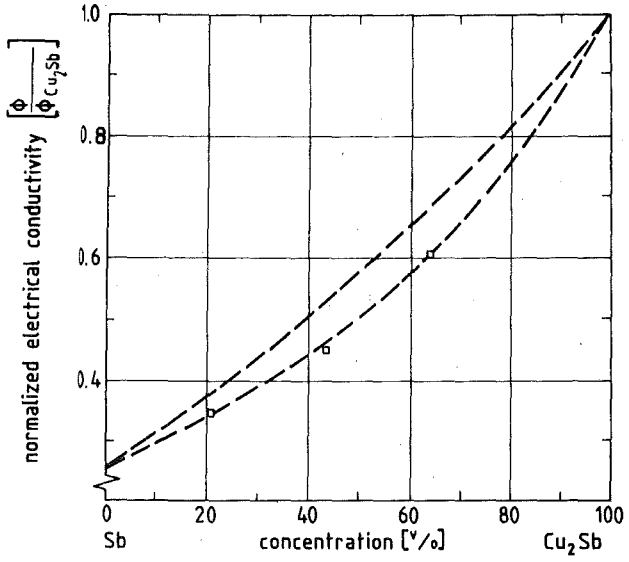

Fig. 46: Electrical conductivity of Cu_2Sb-Sb metal (□) at 289 K [150] and II. order bounds (-----).

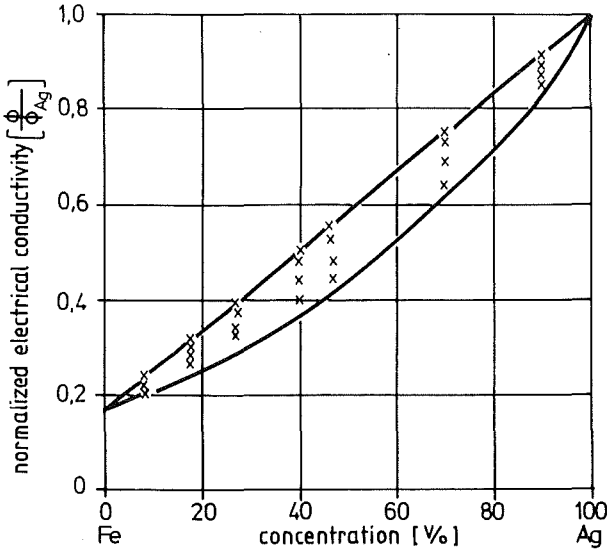

Fig. 47: Electrical conductivity of Ag-Fe metal (x) at 289 K [150] and respective bounds for spheres or directionally oriented fibres as inclusion phase (–).

Fig. 48 refers to spherical copper inclusions in a Zn-matrix phase, where the respective curve was calculated according to equ. (40) and fig. 49 shows the comparison of experimental data with a calculated curve for Bi-Cu-metal: In order to

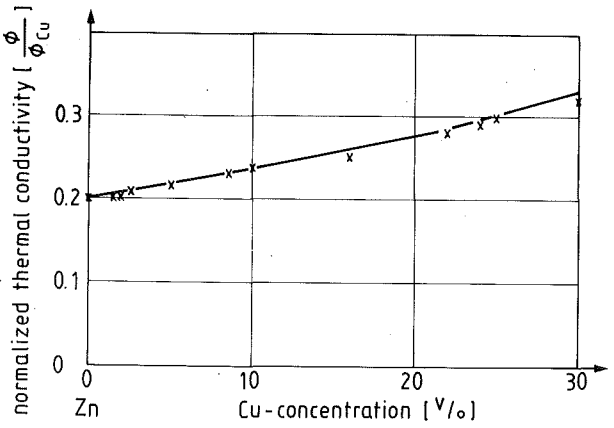

Fig. 48: Thermal conductivity of Cu-Zn metal with Zn-matrix phase and spherical Cu inclusions (x) at room temperature [156] and calculated curve (–).

simulate directionally solidified eutectics a network of Cu-fibres ($F_{\parallel} = 0.5$) has been included into a Bi-matrix phase. The orientation of the fibre-network was perpendicular to the current direction ($\alpha_{\parallel} = 90°$) as drawn in fig. 49. This microstructural arrangement refers to equ. (41) which, in fact, describes the slope of the electrical conductivity values even bringing out the scattering more clearly by proper ordinate magnification (fig. 49) [201].

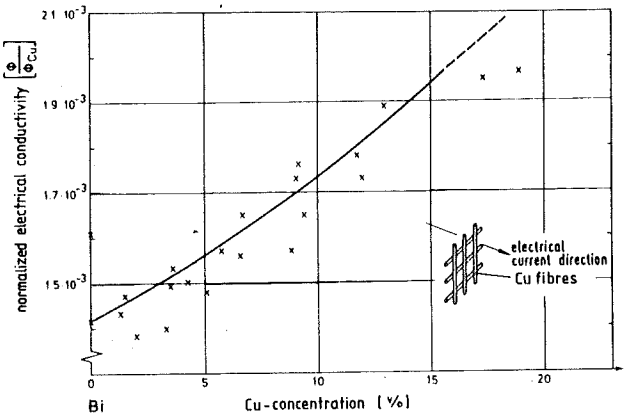

Fig. 49: Electrical conductivity of Bi-Cu metal (x) at room temperature [270] with a Cu fibre network oriented perpendicular to the direction of electrical current and calculated curve (—).

Finally in figs. 50 and 51 the measured electrical and thermal conductivities of Al-matrix phase metal materials containing oriented steel fibres ($F_{\parallel} = 0.5$) as a inclusion phase are compared with calculated curves [201]. The fibres have been oriented under different angles to the electrical current or heat flux direction (0°; 30°; 60°; 90°), for which the respective orientation factors have been introduced into equ. (32).

As pointed out in figs. 50 and 51 there is a clear reflection of the variation of the fibre orientation by the theoretical curves for electrical as well as for the thermal conductivity. It might be worthwhile in this context to mention that short fibres of small diameter as the inclusion phase being oriented in field direction cause almost the same effect on the effective field property as long fibres due to the same shape factor approach ($F_{\parallel} = 0.5$). Keeping in mind with respect to technology

that long fibres are usually more complicated to handle, this result is also of practical interest.

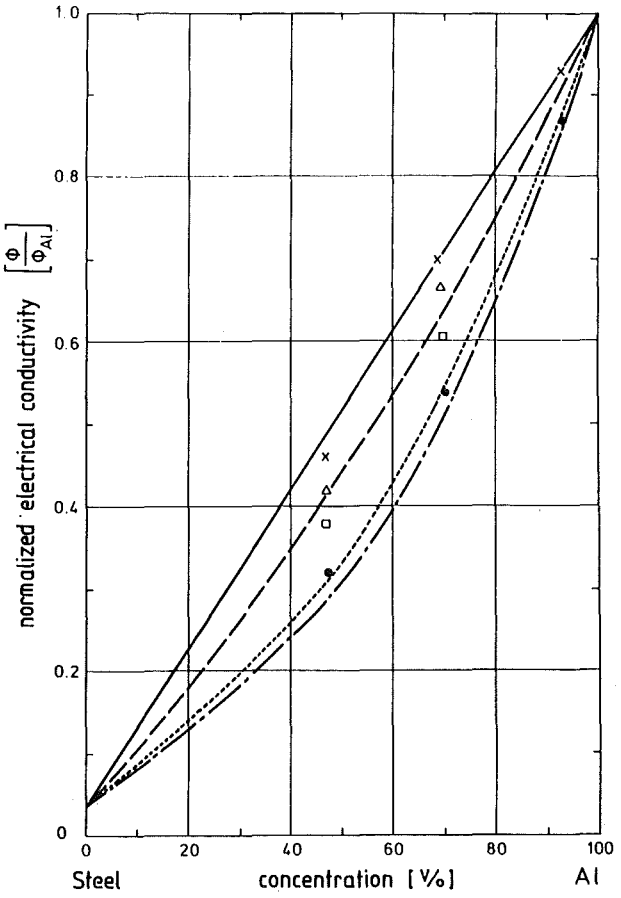

Fig. 50: Electrical conductivity of Al-SS metal with Al-matrix phase and oriented steel fibres (x 0°; Δ 30°; □ 60°; ● 90° inclination of the fibre axis towards the direction of electrical current) as inclusion phase at room temperature [129] and theoretical curves for the respective inclinations (—— 0°; ---- 30°; ····· 60°; –·– 90°).

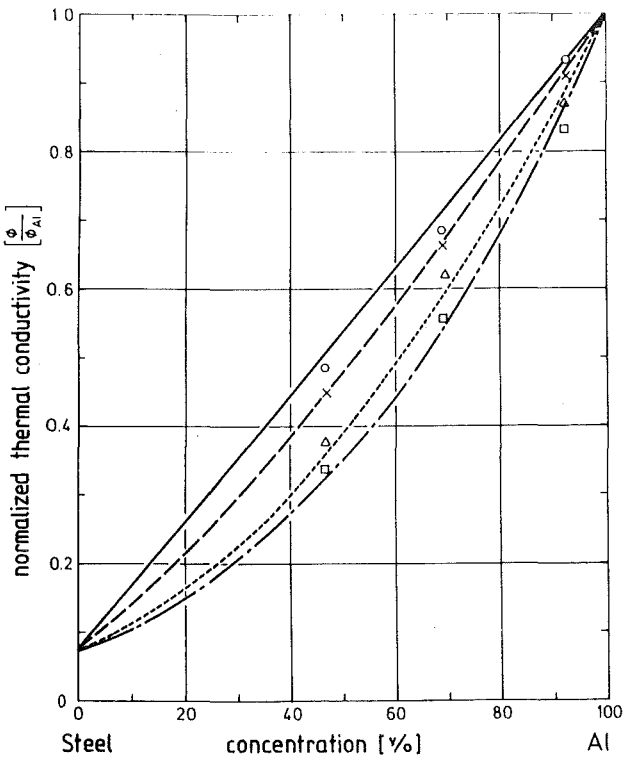

Fig. 51: Thermal conductivity of Al-SS metal with Al-matrix phase and oriented steel fibres (o 0°; x 30°; Δ 60°; □ 90° inclination of the fibre axis towards the direction of heat flux) as inclusion phase at room temperature [129] and theoretical curves for the respective inclinations (—— 0°; ---- 30°; ····· 60°; -·- 90°).

4.2 Two-phase Ceramics

Reported electrical conductivities of two-phase ceramics [197] are compared in fig. 52 with the respective I. order bounds demonstrating clearly, that bounding in that case is not a sufficient engineering approach to describe the effect of phase concentration on the selected field property. - For the thermal conductivity of BeO-MgO-ceramics (fig. 53) as well as of the very "practical" clay-technical zirconia system (fig. 54), however, already I. order bounds offer useful restrictions of the variational region with phase concentration, which is even more true for the case of isotropic "Bamica"-Al_2O_3 matrix phase ceramics and the respective III. order bounds (fig. 55).

And although special conditions have to be observed when treating magnetic properties, which are still under consideration, literature data of the magnetic permeability of isotropic "Nizifer"-$BaTiO_3$ fit well with II. order bounds (Fig. 56).

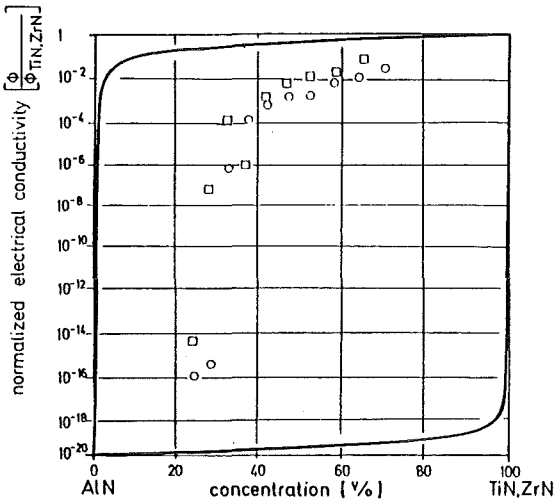

Fig. 52: Electrical conductivity of AlN-TiN (□) and AlN-ZrN ceramic (o) at room temperature [34] and I. order bounds (——).

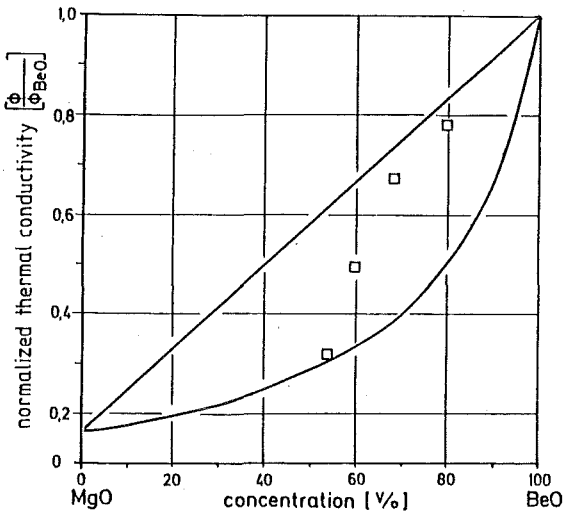

Fig. 53: Thermal conductivity of MgO-BeO ceramic (□) at 473 K [136] and I. order bounds (——).

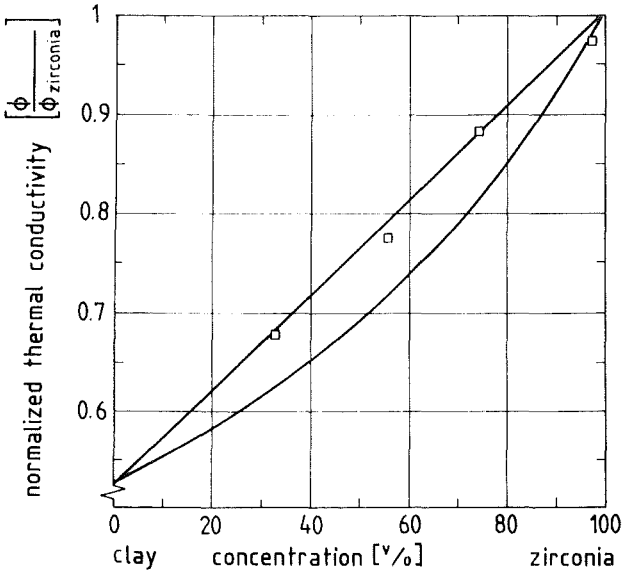

Fig. 54: Thermal conductivity of clay-technical zirconia ceramic (□) at 673 K [110] and I. order bounds (——).

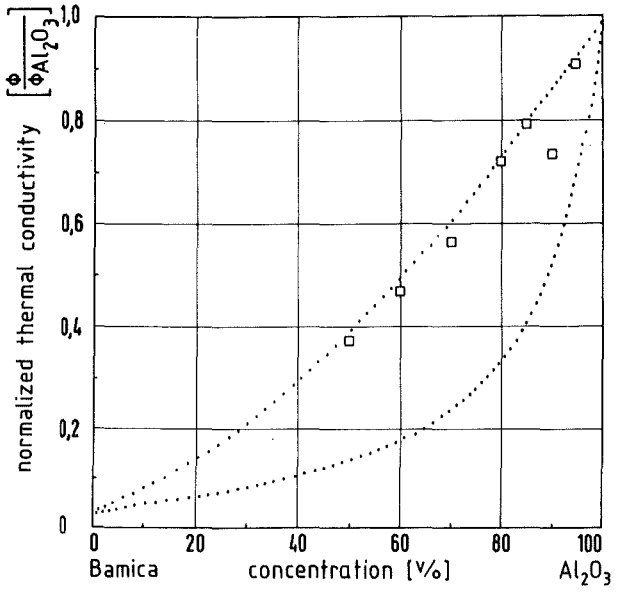

Fig. 55: Thermal conductivity of $BaMg_3Al_2Si_2O_{10}F_2$ ("Bamica")-Al_2O_3 ceramic with Al_2O_3 matrix phase (□) at 673 K [264] and III. order bounds (·····).

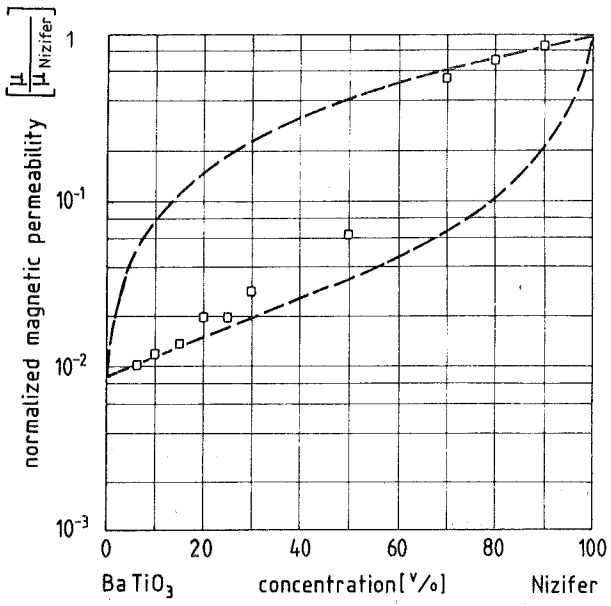

Fig. 56: Magnetic permeability of "Nizifer" (49.3 wt.% Fe_2O_3 + 17.5 wt.% NiO + 33.2 wt.% ZnO)-$BaTiO_3$ ceramic (□) at room temperature [34] and II. order bounds (----).

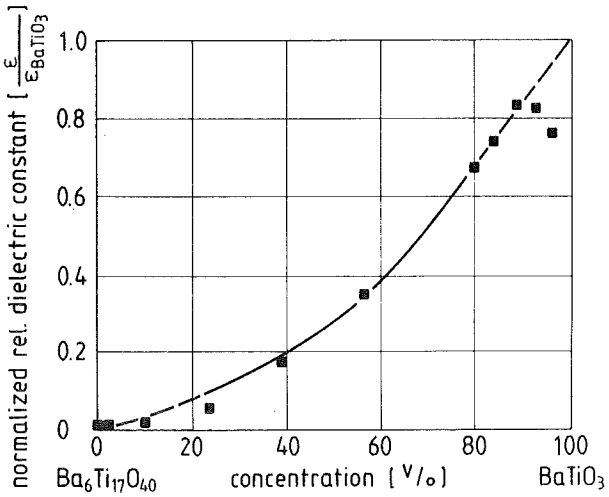

Fig. 57: Relative dielectric constant of $Ba_6Ti_{17}O_{40}$ - $BaTiO_3$ ceramic (▮) with interconnecting phase microstructure at room temperature [17,21] and calculated curve (——).

If the available information about the microstructure permits the use of a microstructure-field property equation instead of bounds, a single curve follows correlating the field property and the phase concentration. This is the case for a two-phase ceramic in fig. 57, where the two phases form an interconnecting microstructure ($F_{\parallel} = 0.5$; $\cos^2 a_{m,k} = 0.33$) over a wide range of phase concentrations (15 vol.% < c < 85 vol.%) [17,21]. The measured field property concerns the relative dielectric constant, the calculated curve refers to equ. (36) taking into account the above mentioned shape and orientation factors [17,21].

4.3 Two-phase carbon-polymer materials

With respect to fig. 2 carbon - or graphite - is difficult to coordinate but it is a non-metal-containing material and a basic element for polymers. This is why carbon-polymer materials are considered separately in this chapter [197].

In figs. 58 and 59 electrical conductivities of carbon-polymer matrix phase combinations are compared with the respective III. order bounds. In fig. 60 the same

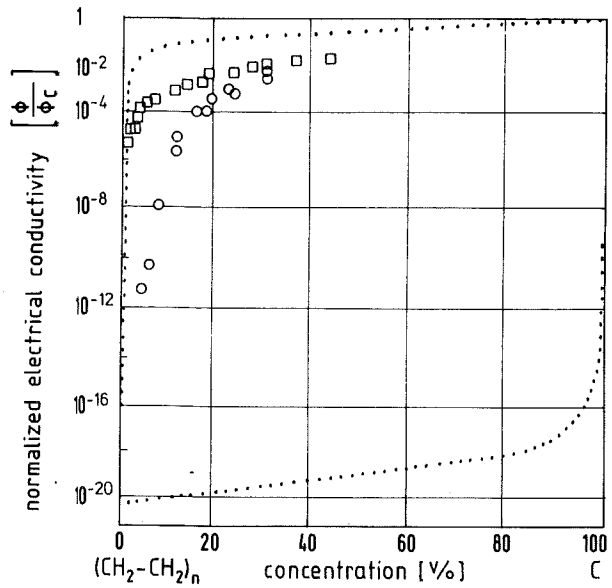

Fig. 58: Electrical conductivity of $(CH_2\text{-}CH_2)_n$-C two-phase material with polyethylen matrix phase (□ o) at room temperature [238] and III. order bounds (⋯).

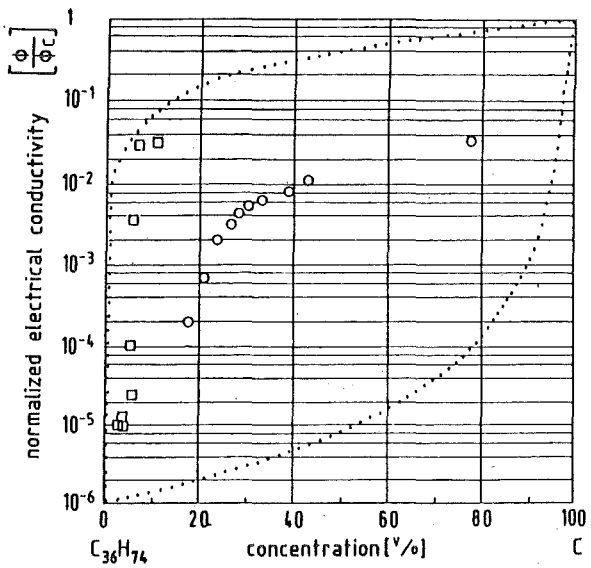

Fig. 59: Electrical conductivity of $C_{36}H_{74}$-C two-phase material with wax matrix phase (□ o) at room temperature [104,225] and III. order bounds (····).

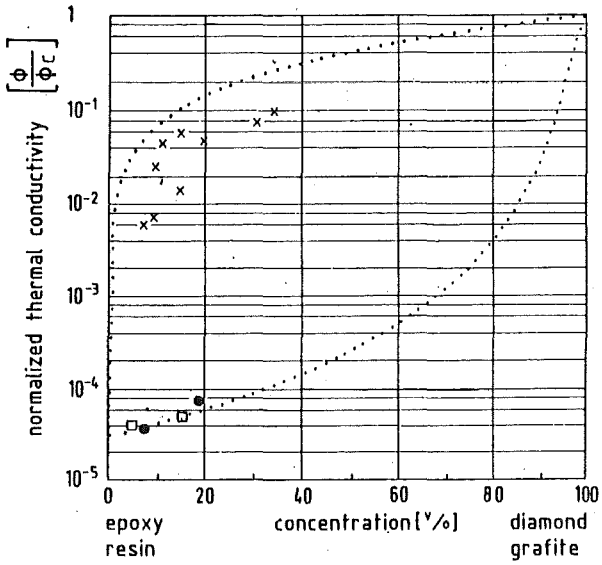

Fig. 60: Thermal conductivity of epoxy-diamond (□) and epoxy-grafite as well as resin-grafite (x) two-phase materials at room temperature [90,104,106] and III. order bounds (····).

has been done for the thermal conductivitiy of a diamond-polymer matrix phase and graphite-polymer matrix phase combinations. For graphite fibres ($F_D = 0.5$) included in a phenolformaldehyde matrix phase and oriented perpendicularly to the temperature gradient ($\cos^2\alpha_D = 0$) the measured thermal conductivities are compared with the respective theoretical curve according to equ. (41) in fig. 61. Combinations of carbon with other than polymer phases are treated amongst composites.

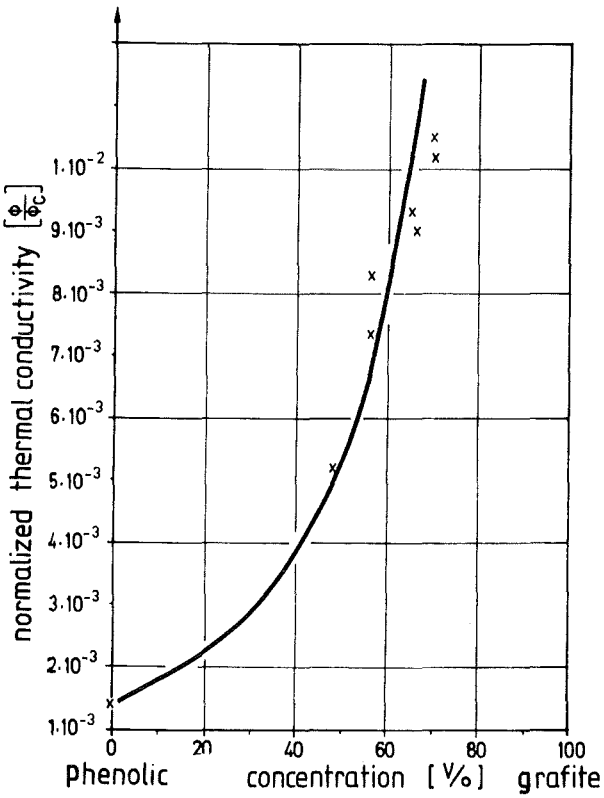

Fig. 61: Thermal conductivity of phenolic SC 1008 (phenolformaldehyd)-grafite material with phenolic matrix phase and included grafite fibres oriented perpendicularly to the temperature gradient (x) at room temperature [258] and theoretical curve (—).

4.4 Two-phase composites

If, according to nomenclature and fig. 2, the phases of a multiphase material belong to different main groups of materials as either metallic and ceramic mate-

rials, ceramic and non-metal-containing materials (e.g. polymers) or polymeric and metallic materials then one is dealing with composites [202,206]. More than that the structure of composites has to be macroscopically homogeneous and microscopically quasihomogeneous. Macroscopically inhomogeneous phase combinations as sandwich materials or plated materials are "composed materials" but not composites in the sense of this definition. And also combinations such as carbon fibres in a carbon matrix (CFC) are not composites but carbon- based materials with a technically produced, instead of in-situ formed, ("fibre-reinforced") microstructure.

Composites, thus defined, are especially appropriate to test theoretical predictions since due to the difference in the field properties of their phases, which is usually big, their effective properties reflect microstructural alterations particularly sensitively [196,203,204].

In figs. 7 and 20 the measured electrical conductivities of a number of two-phase, isotropic composites have been compared with the respective bounds which process is now continued by figs. 62 - 85. The sequence of the figures follows the decreasing difference in the field properties of the pure phases, which results in closer bounds of any order. Electrical (fig. 62 - 67, 69, 70, 72, 80, 82, 84, 85) as well as thermal conductivities (figs. 68, 71, 79, 81, 83) of cermets (figs. 7, 20, 62 - 67, 71, 74, 77 - 82, 84, 85) including steel as an exception (fig. 80), metal-polymer (figs. 7, 68, 73) and polymer-ceramic composites (figs. 75, 76, 83) are included in the comparison between measured data and bounds. Amongst them those with glasses (figs. 65, 83) or carbon (figs. 69, 70, 72) occur. Apart from a few exceptions, amongst them those for resin-Al [106,138], resin-Cu [106,246] and UO_2-Mo [128], the comparison between experimental values and theoretical bounds for field properties confirms the practical reliability of bound predictions in the frame of their restricted accuracy. If, however, the information about the microstructure is sufficient, the more definite microstructure-field property equations based on model microstructure assumptions should be used. This was possible and has been done for the composites mentioned in figs. 86 to 96. The computed curves in figs. 86, 87 ($F_D = 0{,}33$; $\cos^2\alpha_D = 0.33$) refer to equation (44), whilst equation (45) ($F_D = 0{,}33$; $\cos^2\alpha_D = 0.33$) holds true for the calculated slope in figs. 88 and 89. In figs. 90 to 93 the theoretical calculation of the slope of the field properties versus phase concentration was based on equation (40) (spherical inclusions). As expected and demonstrated in fig. 94 the calculation with equation (43) (oriented

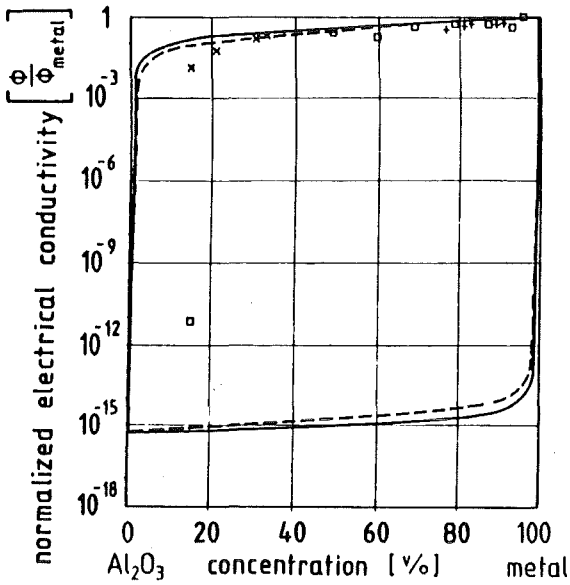

Fig. 62: Electrical conductivity of Al_2O_3-cermets with Cr (+) at 300 K [77], Ni_3Al_2 (□) at 300 K [123] and W (x) at 1373 K [83] and I. (——) and II. (---) order bounds.

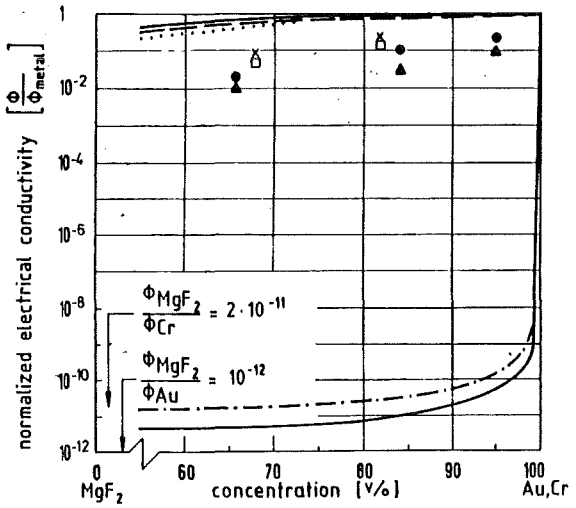

Fig. 63: Electrical conductivity of MgF_2-cermets with Au matrix phase at 323 K (□) and 598 K (x) and with Cr matrix phase at 313 K (▲) and 693 K (●) and I. (——), II. (---) and III. (····) order bounds.

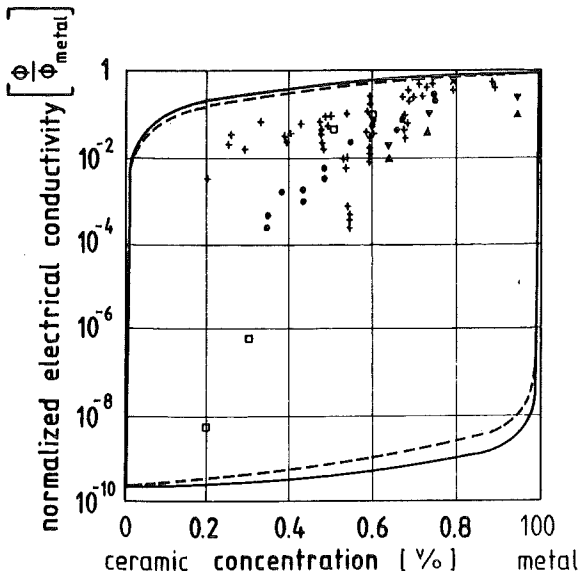

Fig. 64: Electrical conductivity of Al_2O_3-Fe cermets (+) [71,82,247], Al_2O_3-Ni-cermets (●) [247], UO_2-Cu cermets (x) [40], U_3O_8-Al cermets (□) [207] at room temperature and I. (——) and II. (---) order bounds.

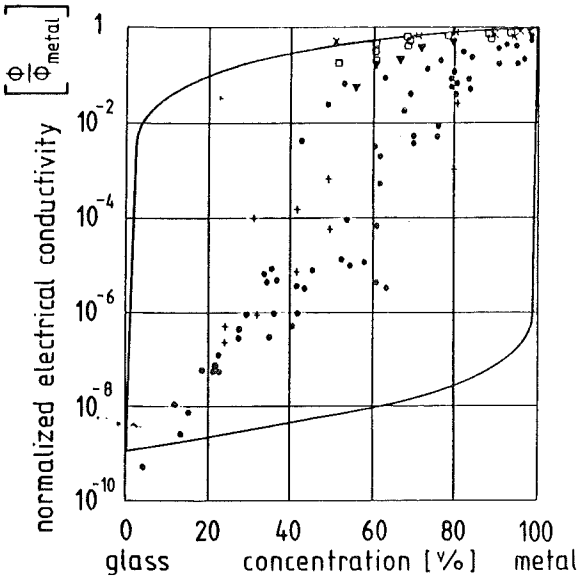

Fig. 65: Electrical conductivity of glass cermets with Au (+) [18], Cr (●) [18,179,212], Cu (x) [29], Fe (□) [89] and Ni (▼) [133] at room temperature and I. (——) order bounds.

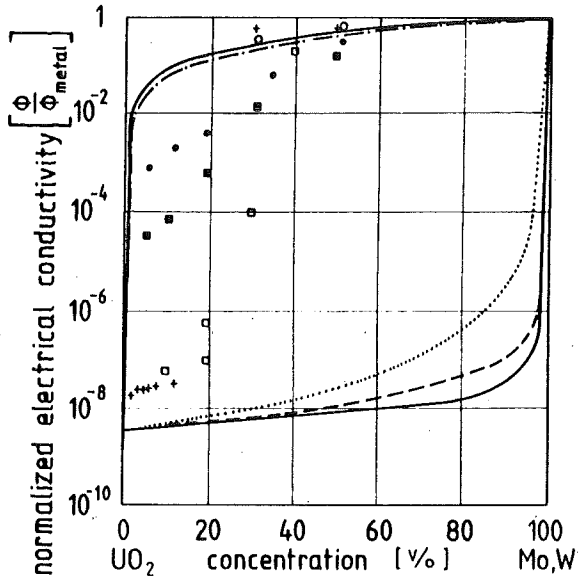

Fig. 66: Electrical conductivity of UO_2-Mo cermets at 300 K (□) and 1573 K (■) [116,6,250], UO_2-W cermets at 300 K (o) and 1573 K (●) [6,250] and polypropylene ($CH_2 = C_2H_4$)-Al composites at 873 K (+) [90] as well as I. (——), II. (---) and III. order bounds (····; UO_2 and polypropylen matrix phases, resp.).

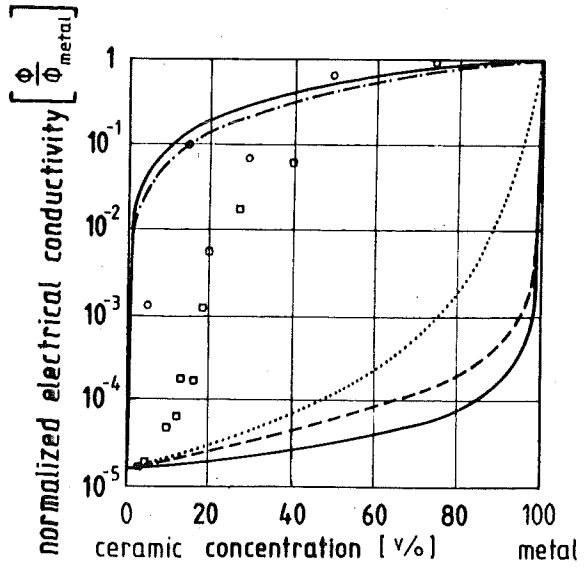

Fig. 67: Electrical conductivity of UO_2 Mo cermets at 300 K (o) [92] and ZrO_2-Mo cermets at 1923 K (□) [82] and I. (——), II. (---) as well as III. order (·····; ceramic matrix phases) bounds.

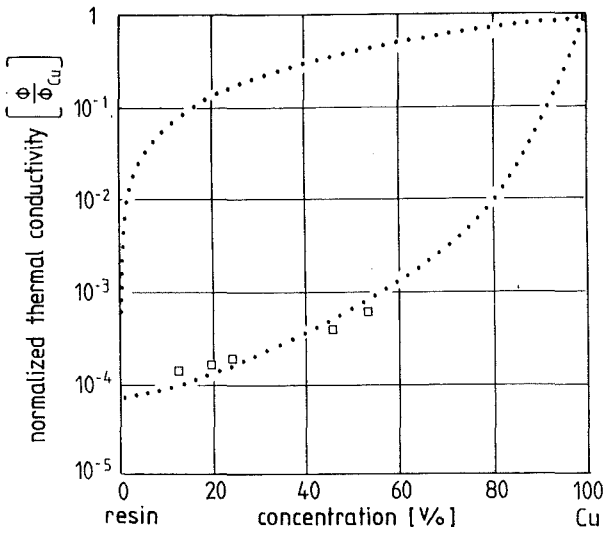

Fig. 68: Thermal conductivity of resin matrix phase - copper composites (□) at 20 K [240] and III. order bound (·····).

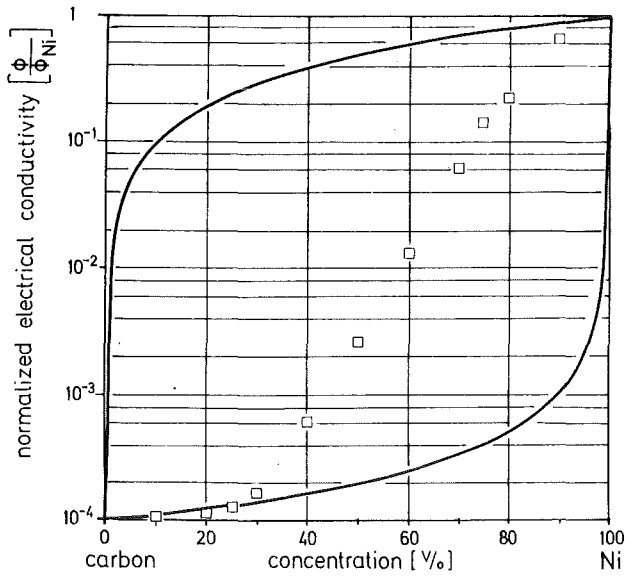

Fig. 69: Electrical conductivity of carbon-nickel composites (□) at room tempera ture [239] and I. (——) order bounds.

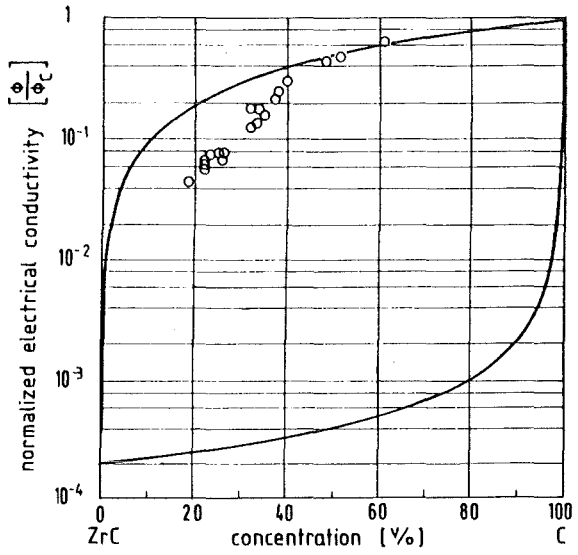

Fig. 70: Electrical conductivity of ZrC-C composites (o) at room temperature [89] and I. (——) order bounds.

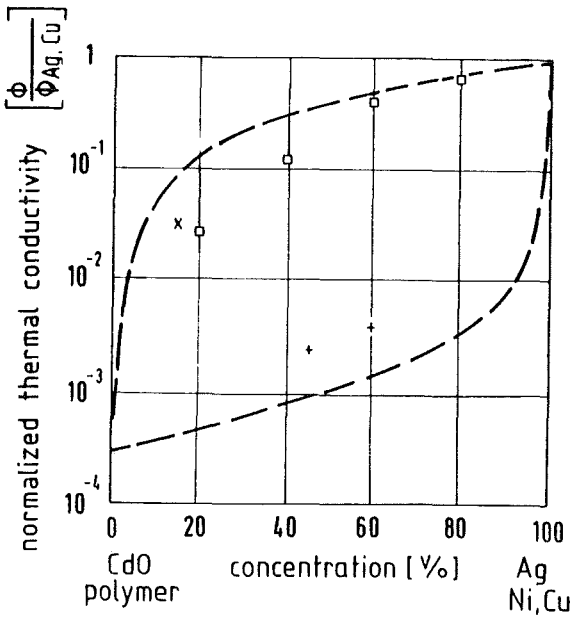

Fig. 71: Thermal conductivity of CdO-Ag cermets in (□) [31], epoxy-Cu (+) [59,192] and polyvinylchloride-Cu composites (x) [148] at room temperature and II. order bounds (----).

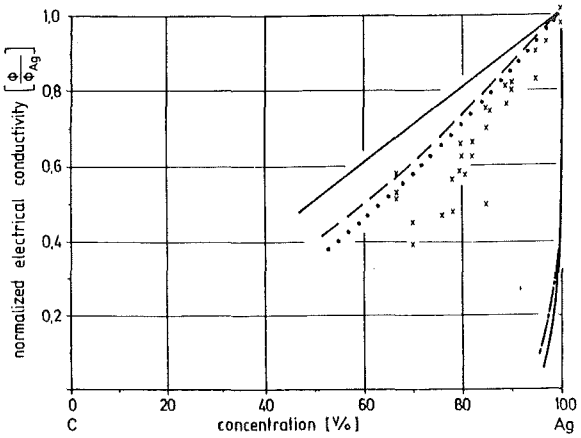

Fig. 72: Electrical conductivity of graphite-Ag matrix phase composites (x) at room temperature [36,74,94,97,115,242] and I. order (——), II. order (- - - -), III. order bounds (···).

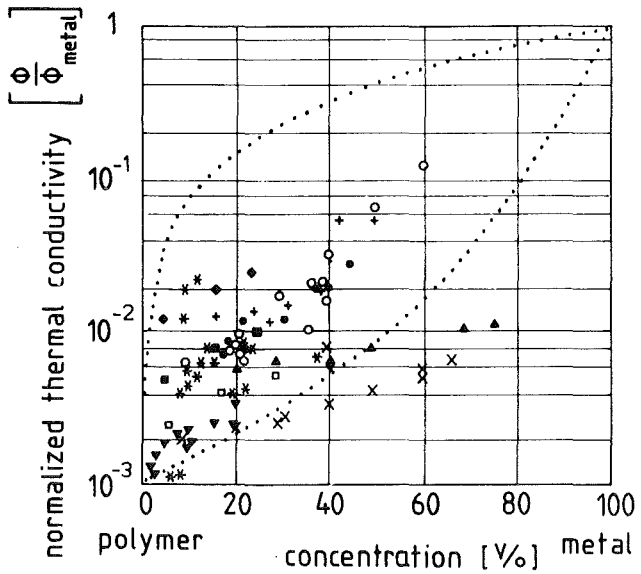

Fig. 73: Thermal conductivity of polyethylene-Al (x) [9], polyethylene-Cu (▼) [9], polyethylene-Fe (Δ) [9], resin-Al (o) [8,55], resin-Al/Ti (●) [8], resin-Cu (*) [8], resin-Cu/Ti (+) [8], silicon-Al (□) [53], silicon-Ni (▮) [53], silicon-Pb (▪) [53] composites with polymer matrix phases at room temperature and III. order bound approach (·····; matrix phase normalized thermal conductivities averaged).

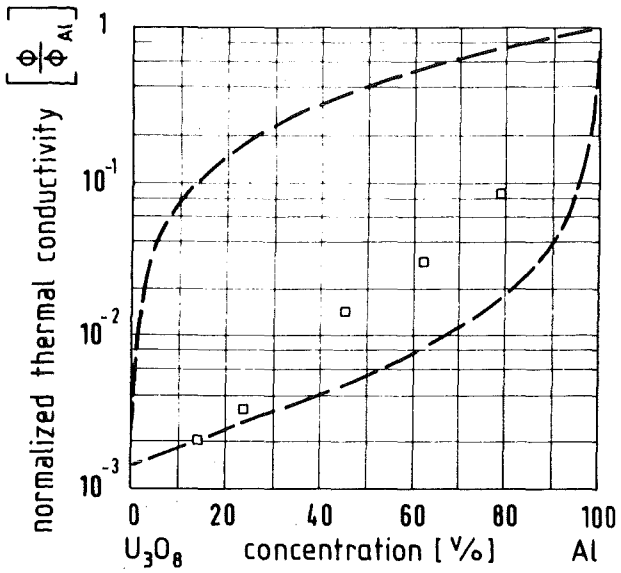

Fig. 74: Thermal conductivity of U_3O_8-Al cermets ([]) at room temperature [244] and II. order bounds (----).

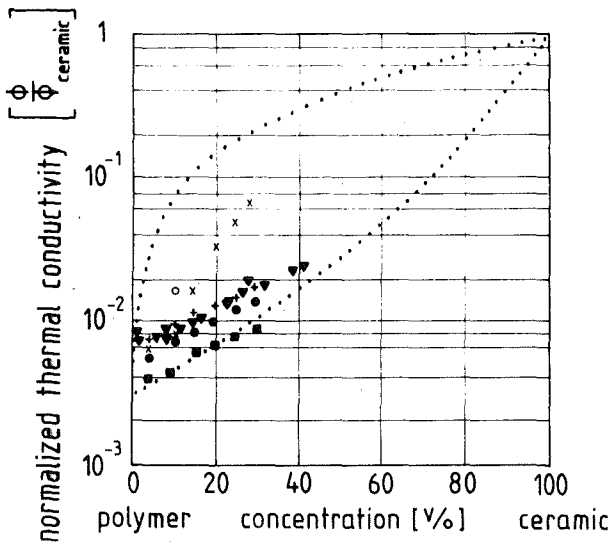

Fig. 75: Thermal conductivity of polyethylene $(CH_2 = CH_2)_n$-MgO (x +) [252,253], polystyrol $(C_6H_5\text{-}CH = CH_2)_n$-$Al_2O_3$ (●) [252], polystyrol-MgO (▮) [252], polyvinylchloride-Ni (o) [246], resin-Al_2O_3 (∇) [90,106] composites with polymer matrix phases at room temperature and III. order bounds (·····; matrix phase normalized thermal conductivities averaged).

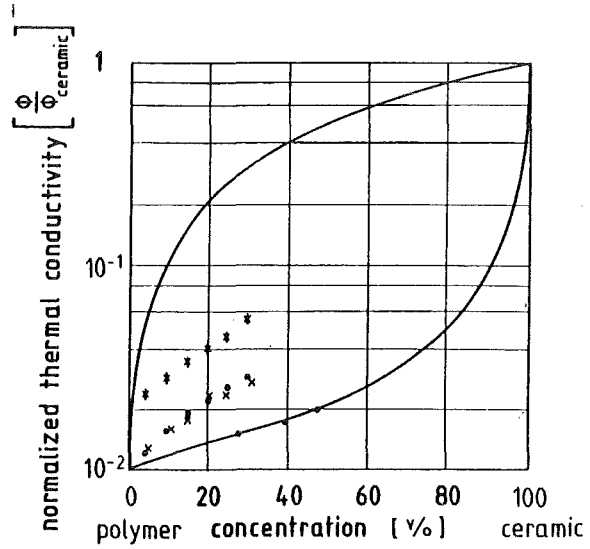

Fig. 76: Thermal conductivity of polyethylene $(CH_2 = CH_2)_n$-Al_2O_3 (■) [113], polyethylene-CaO (*) [252], polystyrol $(C_6H_5{\cdot}CH = CH_2)_n$-$Al_2O_3$ (●) [252], polystyrol-CaO (x) [252] composites and I. order bounds (——; matrix phase normalized thermal conductivities averaged).

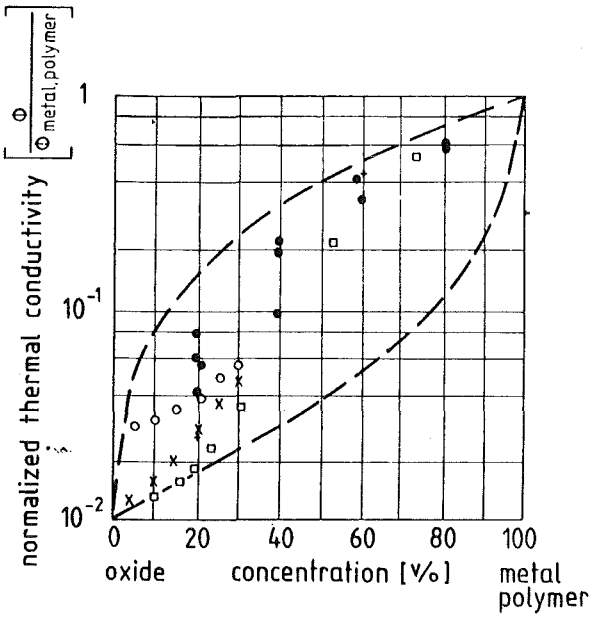

Fig. 77: Thermal conductivity of Al_2O_3-Fe (□) [76], Al_2O_3-polyethylene (x) [253], CaO-polyethylene (o) [253], La_2O_3-W (●) [244,116] and UO_2-Cu (+) [244] composites at room temperature and II. order bounds (----; matrix phase normalized thermal conductivities averaged).

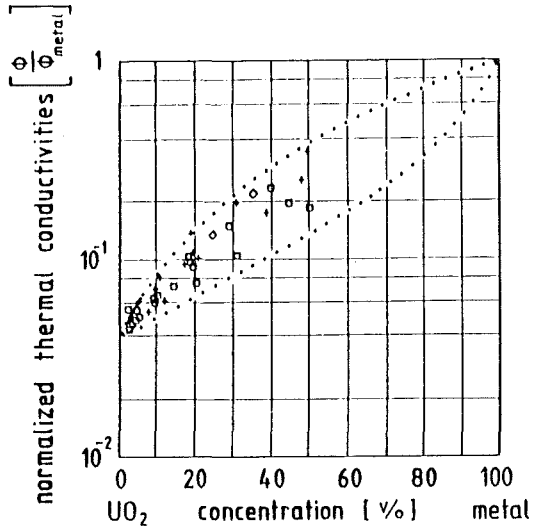

Fig. 78: Thermal conductivity of UO_2-Mo cermets (□) at 300 K and 473 K [95,128,250], UO_2-Ni cermets (◇) at 300 K]121] and UO_2-W cermets (+) at 300 K and 473 K [95,176,250] with metal matrix phase and III. order bounds (·····).

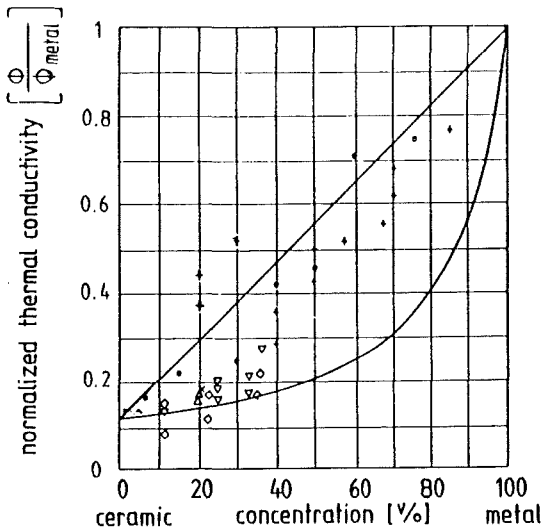

Fig. 79: Thermal conductivity of UO_2-Cr cermets (x) at 300 K [62], UO_2-Fe cermets (▽) at 473 K [92,176] and UO_2-Mo cermets (●) at 873 K [92], UO_2-Nb cermets (Δ) at 300 K [62], UO_2-Ni cermets (◇) at 473 K [92], UO_2-SS (stainless steel) cermets (+) at 773 K and 1073 K [12,62] and I. order bounds (——).

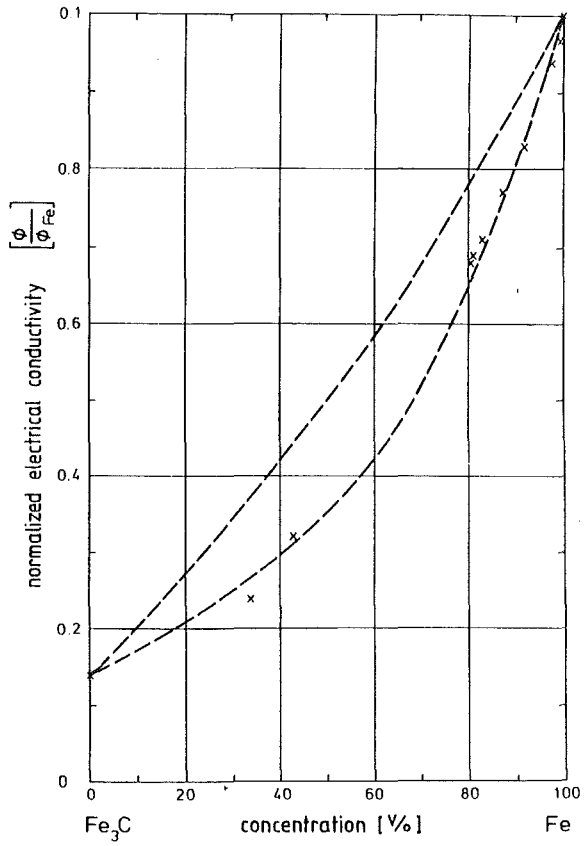

Fig. 80: Electrical conductivity of steel and cast iron (x) at room temperature[154] and II. order bounds (----).

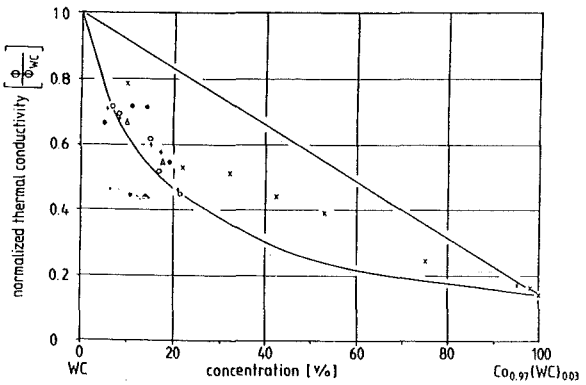

Fig. 81: Thermal conductivity of WC-Co hard metal (x + o ● Δ) at room temperature[7,231] and I. order bounds (——).

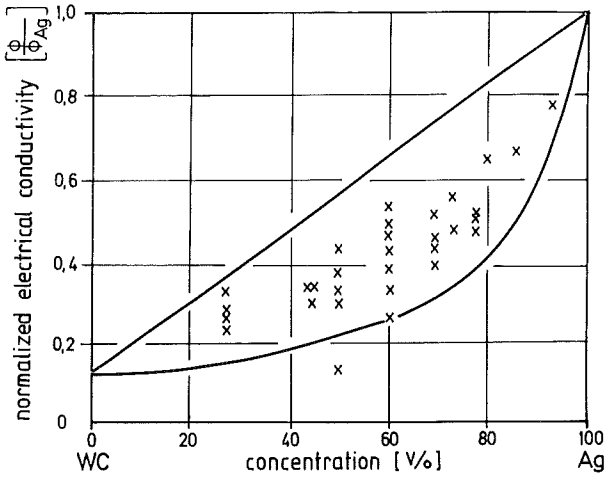

Fig. 82: Electrical conductivity of WC-Ag cermets (x) at room temperature [67,74,80,94,130,242] and I. order bounds (——).

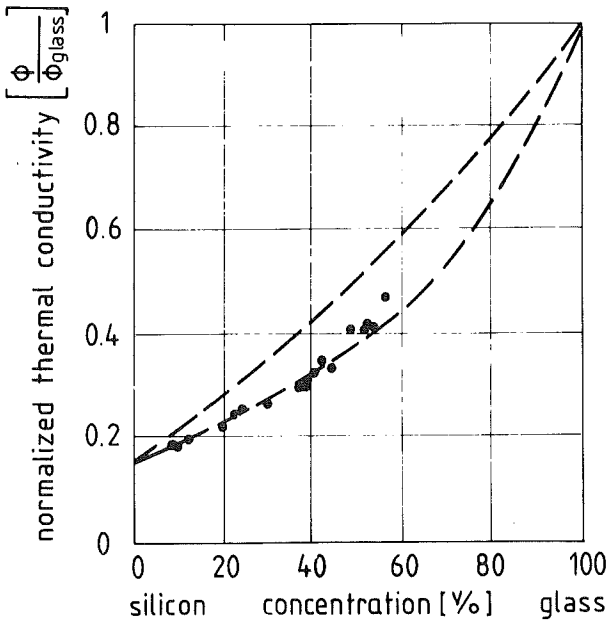

Fig. 83: Thermal conductivity of silicon-glass composites (●) with silicon matrix phase and irregular shaped glass inclusions at room temperature [109,203] and II. order bounds (----).

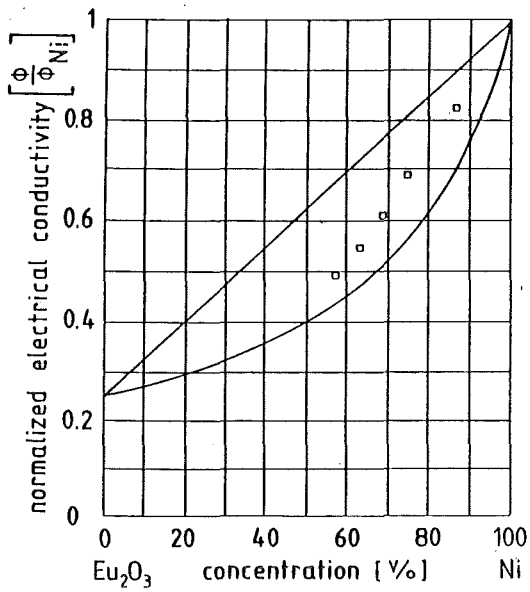

Fig. 84: Electrical conductivity of Eu_2O_3-Ni cermets (□) at room temperature [278] and I. order bounds (——).

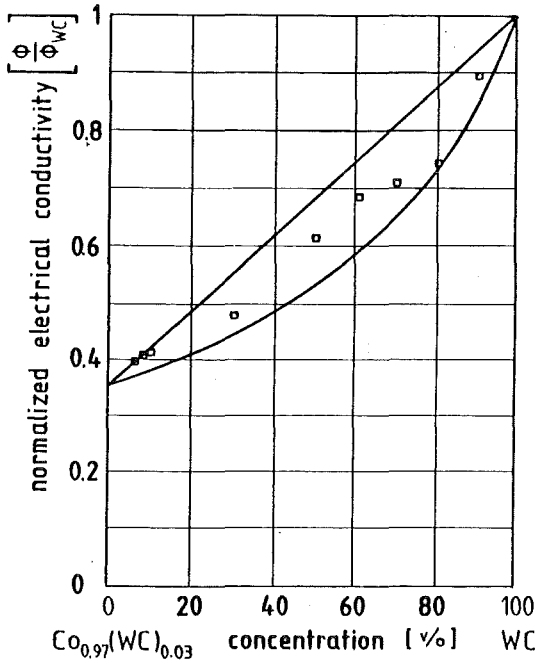

Fig. 85: Electrical conductivity of WC-Co hard metals (□) at room temperature [231] and I. order bounds (——).

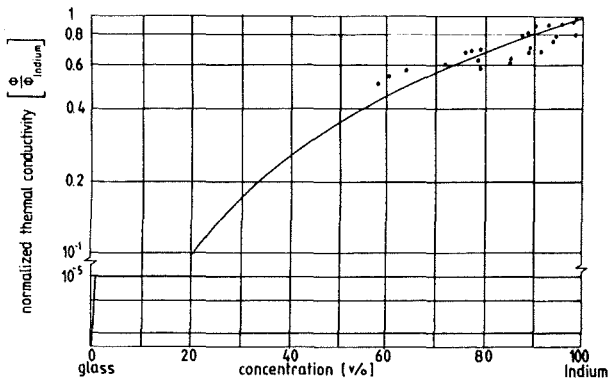

Fig. 86: Thermal conductivity of glass-indium cermets with indium metal matrix phase and included glass spheres (●) at room temperature [91] and calculated curve (——).

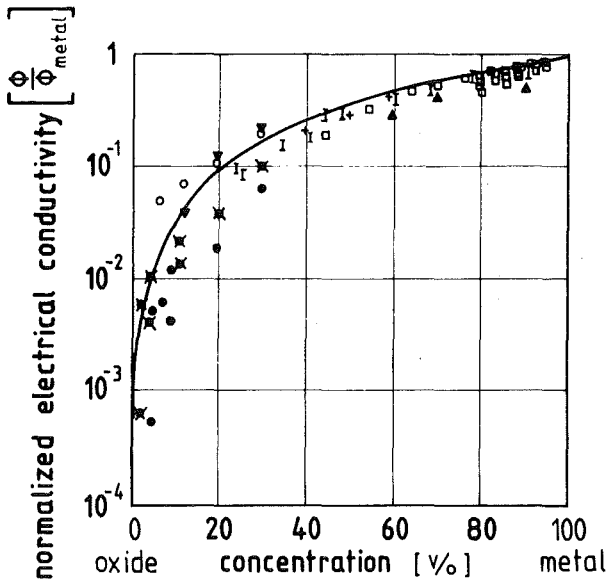

Fig. 87: Electrical conductivity of CdO-Ag cermets (□) at 300 K [31,242], UO_2-Cr cermets (▲▼) at 300 K and 873 K [195,255], UO_2-Cu cermets (I) at 300 K [124], UO_2-Mo cermets (o●) at 1273 K and 1573 K [6,124], UO_2-W cermets (+ x) at 300 K and 1573 K [6,195] with metal matrix phase and spherical ceramic inclusions and calculated curve (——).

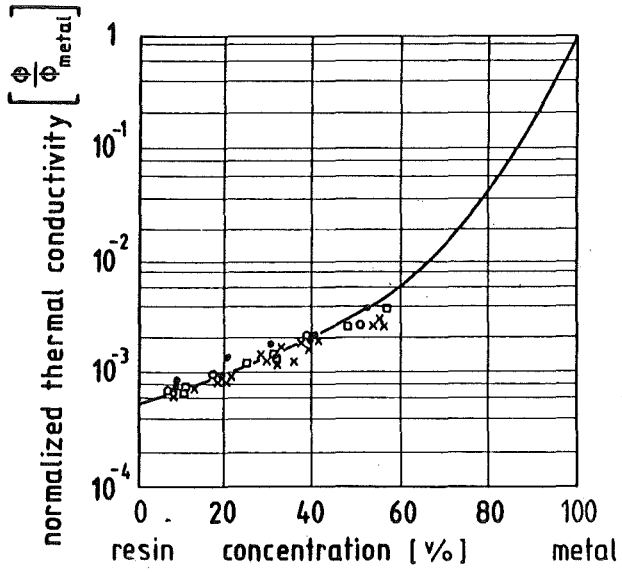

Fig. 88: Thermal conductivity of resin-Ag composites (□) at 300 K, resin-Au composites (o) at 300 K, resin-Cu composites (x) at 300 K, resin-Sn composites (●) at 10 K [151] with resin matrix phase and spherical metal inclusions and calculated curve (——).

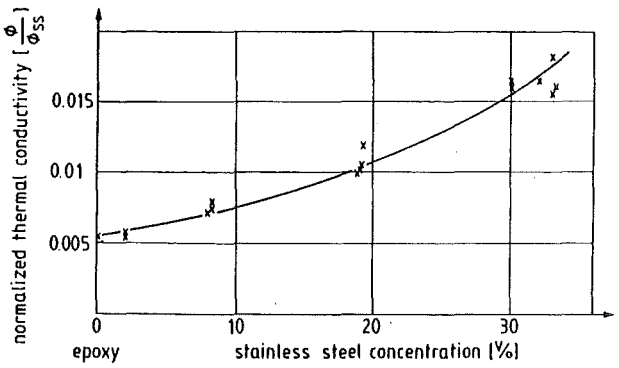

Fig. 89: Thermal conductivity of epoxy-stainless steel composites with epoxy-matrix phase and spherical stainless steel inclusions (x) at room temperature [257] and calculated curve (——).

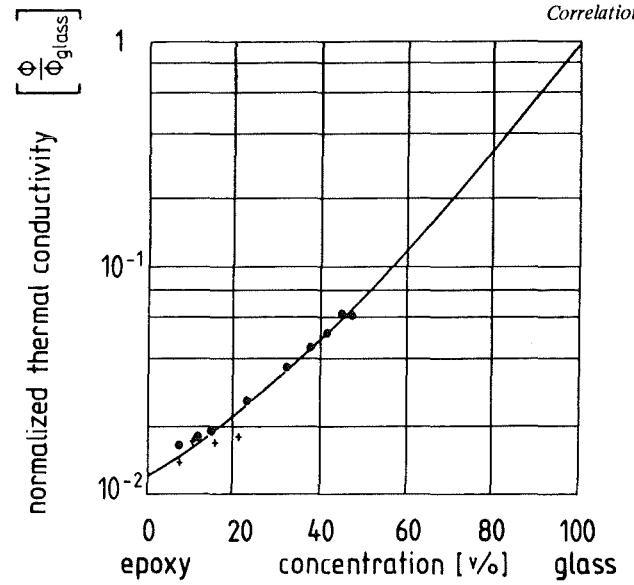

Fig. 90: Thermal conductivity of epoxy-glass composites with polymer matrix phase (+) [227] and with polymer matrix phase and spherical inclusions (●) [90] at room temperature and calculated curve for spherical inclusions (——).

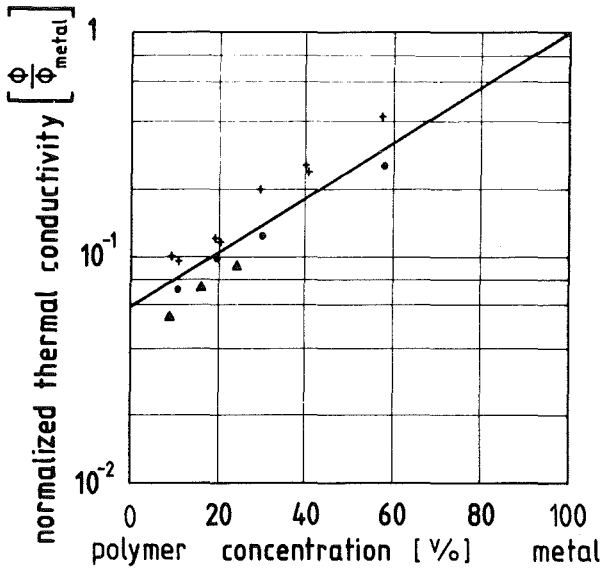

Fig. 91: Thermal conductivity of silicon-Bi composites (Δ) at 300 K [53], resin-Sn composites (+) at 200 K [11], resin-stainless steel composites (●) at 300 K [11] with polymer matrix phases and spherical metal inclusions and calculated curve (——).

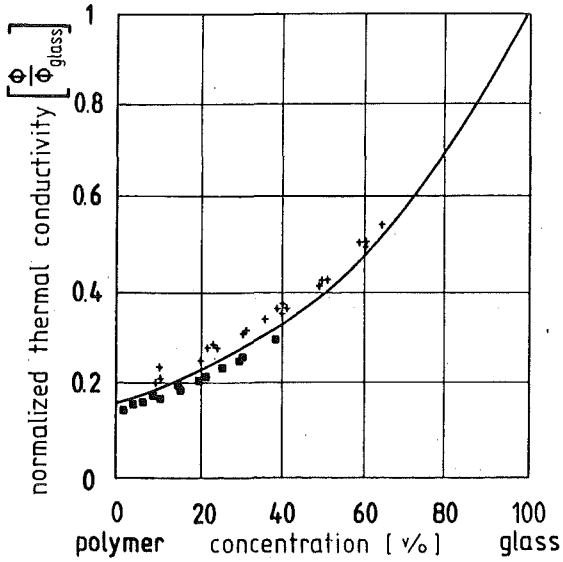

Fig. 92: Thermal conductivity of polystyrol glass (■) [252,253] and silicon-glass composites (+) [108] with polymer matrix phases and spherical glass inclusions at room temperature and calculated curve (——).

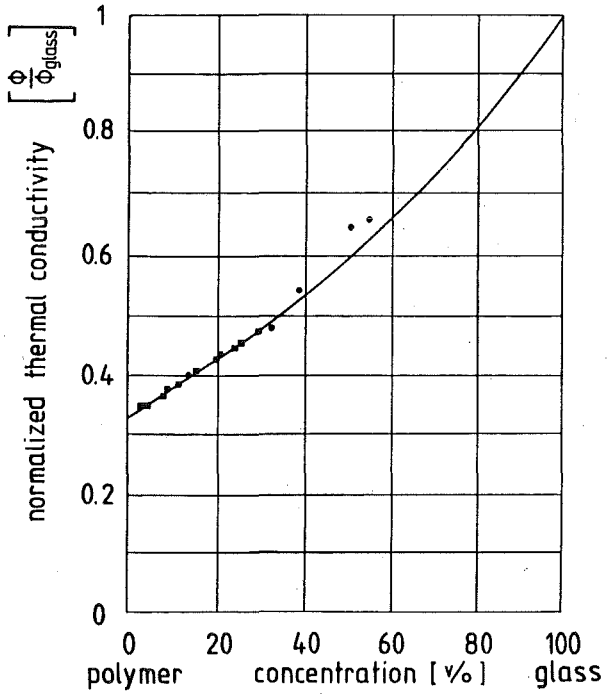

Fig. 93: Thermal conductivity of polyethylene-glass (▮) [253] and epoxy-glass composites (●) [90] with polymer matrix phases and spherical glass inclusions at room temperature and calculated curve (——).

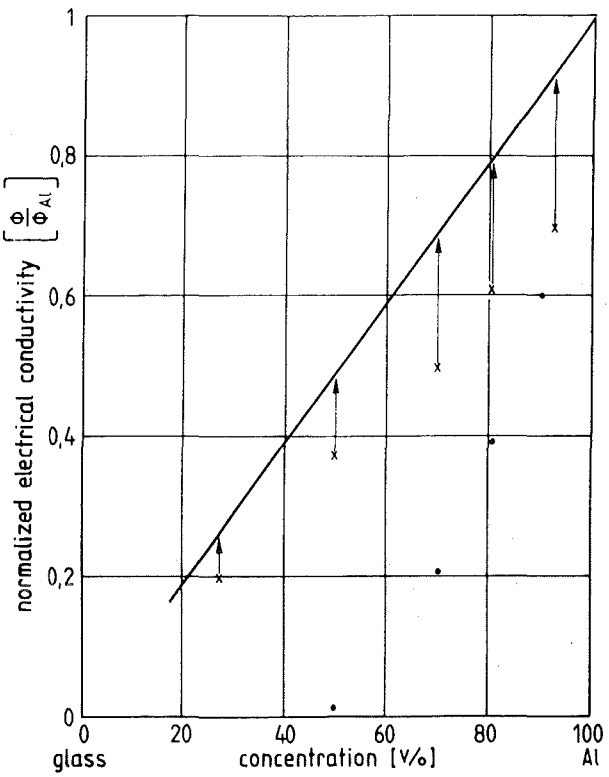

Fig. 94: Electrical conductivity of coextruded (x) and forged (•) glass-Al cermets at room temperature [37] and calculated curve for unidirectional oriented fibres parallel to the electrical current flux (——).

fibres) approaches the measured electrical conductivities for extruded glass-Al cermets more than those for hot forged glass-Al cermets and the variation of orientation according to equations (41) and (43) (oriented fibres) in the case of fig. 95 and according to equation (44) (oriented platelets) in the case of fig. 96 reflects fairly well the measured orientation effect for polymer-glass composites in fig. 95 and for wood metal-bakelite composites in fig. 96.

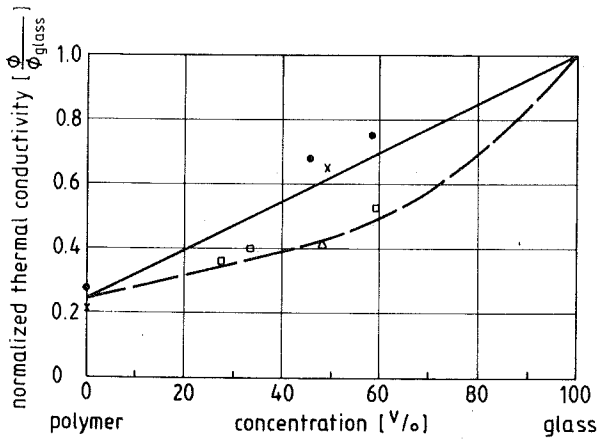

Fig. 95: Thermal conductivity of epoxy-glass (●) [253] and polyester-glass composites (x) with polymer matrix phase and glass fiber inclusions oriented parallel to the heat flux at room temperature and calculated curve (——) as well as epoxy-glass (□) and polyester-glass composites (Δ) with polymer matrix phase and glass fiber inclusions oriented perpendicular to the heat flux at room temperature [213] and calculated curve (----).

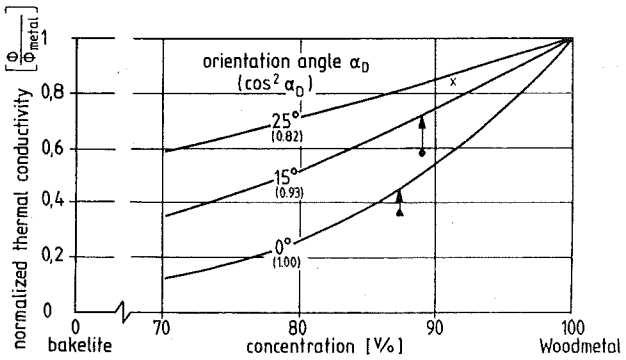

Fig. 96: Thermal conductivity of bakelite-Wood metal composites with Wood metal matrix phase and bakelite platelet inclusions of various orientation (x ● ▲) at room temperature [246] and calculated curves (——).

4.5 Two-phase solid-liquid systems

For a few solid-liquid systems measured data of thermal and electrical conductivities are available to be compared with calculated values. In fig. 97 measured thermal conductivities of sand-water mixtures are compared with calculated curves versus phase concentration. Assuming interconnection of the phases equation (36) (F_1) $\approx$ 0.5; $\cos^2\alpha \approx 0.33$) [244,246] provides the respective curve, which, however, does not meet the experimental data sufficiently, probably due to the assumed microstructural parameters. The less definite II. order bounds, however, include the measured values as expected.

Changing density and electrical conductivity of an NaCl solution (liquid matrix phase) by variable dissolution with pending polymer spheres in it the measured effective electrical conductivities of the liquid-solid system vary as shown in fig. 98. Curves calculated according to equation 40 fit sufficiently well with the experimental data.

4.6 Porous and multiphase materials

The same procedure as used for the comparison of measured and calculated field properties of two phase materials shall now be applied to compare theoretical and experimental values for the field properties of porous materials.

Electrical and thermal conductivities as well as magnetic permeabilities of porous metals and ceramics are compared with I. order bounds according to equs. (56) in figs. 99 - 101. The same has been done in Fig. 102 for carbon and grafite. -

II. and III. order bounds according to equ. (57) and (58) are compared with measured electrical and thermal conductivities of isotropic porous sintered metals and measured thermal conductivities of isotropic sintered porous ceramics in figs. 103 - 105 and III. order bounds according to equ. (58) are compared with experimentally determined electrical and thermal conductivities of isotropic sintered porous oxide and nonoxide ceramics as well as isotropic porous carbon and graphite in figs. 106 - 109.

Turning to two-phase isotropic and nonisotropic sintered porous systems, in which non-spherical pores form one phase, the shape and orientation of which is

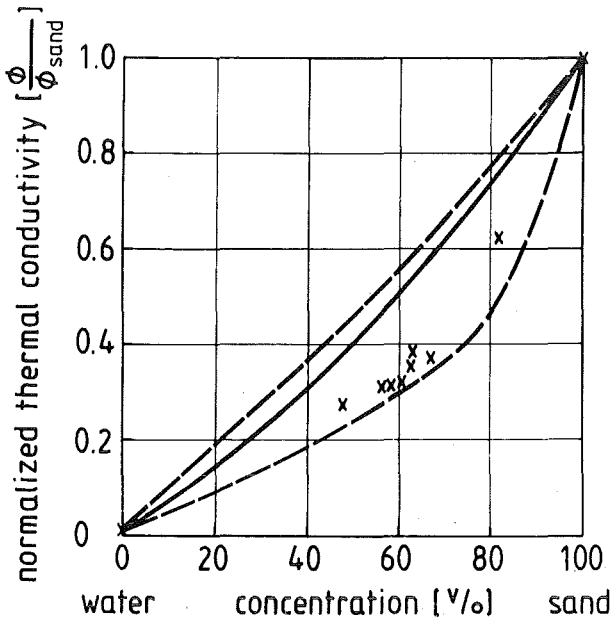

Fig. 97: Thermal conductivity of solid-liquid suspensions with interconnecting sand and water phases (x) at room temperature [275] and calculated II. order bounds (----) as well as the curve for interconnection phase microstructure (——).

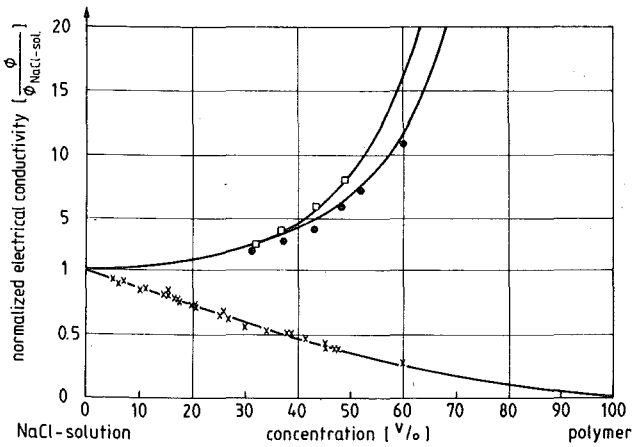

Fig. 98: Thermal conductivity of solid-liquid suspensions with aqueous NaCl-solution as matrix phase and polymer spheres included (Φ_D/Φ_M = 14400: □; Φ_D/Φ_M = 160: ●; $\Phi_D/\Phi_M \approx 0$: x) at room temperature [263] and calculated curves (——).

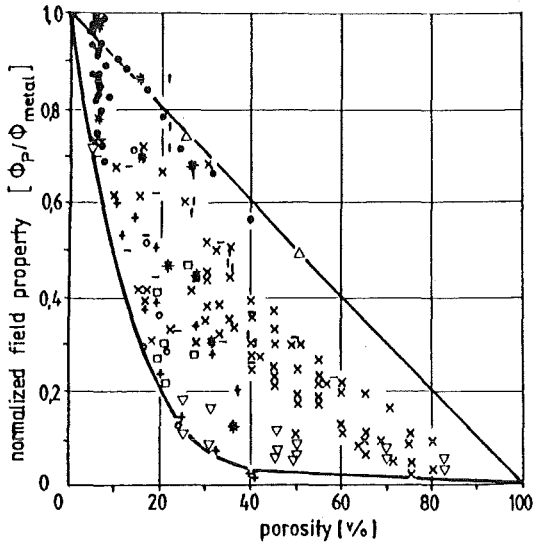

Fig. 99: Field properties of nonisotropic porous metals at room temperature: thermal conducitivity of bronze (□) [99], Cu (o) [272], Ni (Δ) [83], stainless steel (∇) [158]; electrical conductivity of Cu (*) [107], Fe (+) [63,237], Ni (ı) [168], Ni-alloy (x) [142], stainless steel (–) [142]; magnetic permeability of Fe (●) [63,215]; I. order bounds (——).

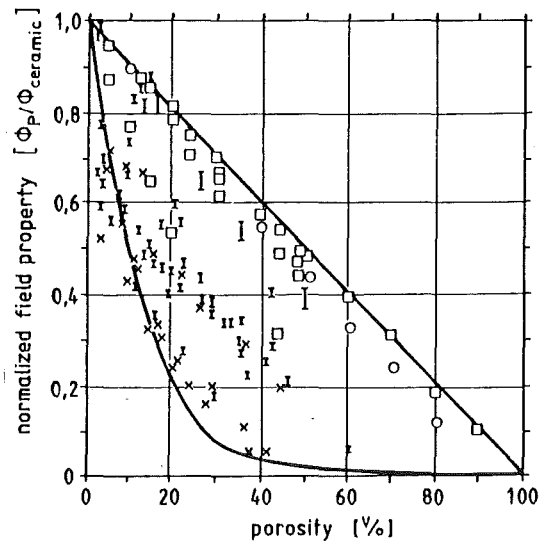

Fig. 100: Field properties of nonisotropic porous sintered ceramics at room temperature: thermal conducitivity of Al_2O_3 (□) [16,83], BeO (o) [16], and various minerals (I) [56,116,229,235,275]; magnetic permeability of $Ni_{0.4}Zn_{0.6}Fe_2O_4$ (x) [118]; I. order bounds (——).

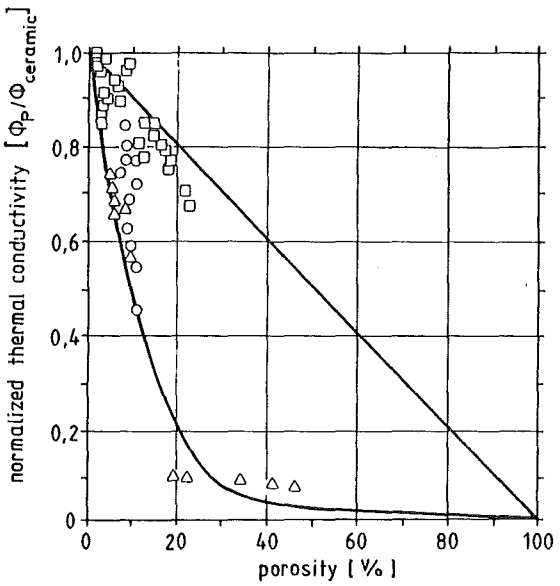

Fig. 101: Thermal conductivity of UO_2 (□) [22,230] $(UP_4)O_2$ (o) [93] and ThO_2 (Δ) [78,184] porous nuclear sintered oxide ceramics at room temperature and I. order bounds (——).

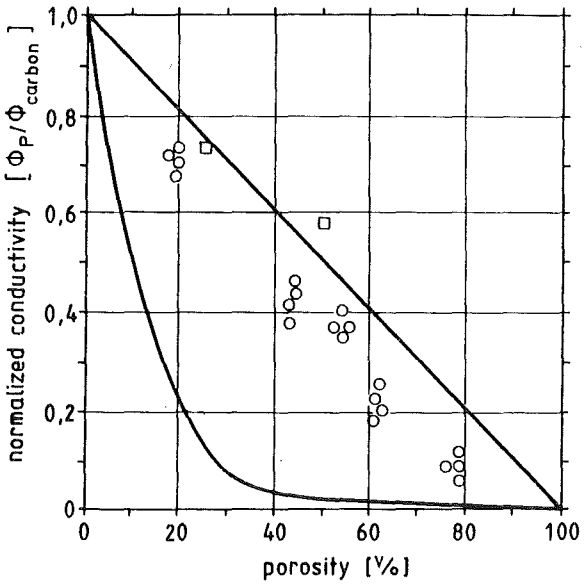

Fig. 102: Thermal (□) and electrical (o) conductivity of porous carbon and grafite at room temperature [23,83] and I. order bounds (——).

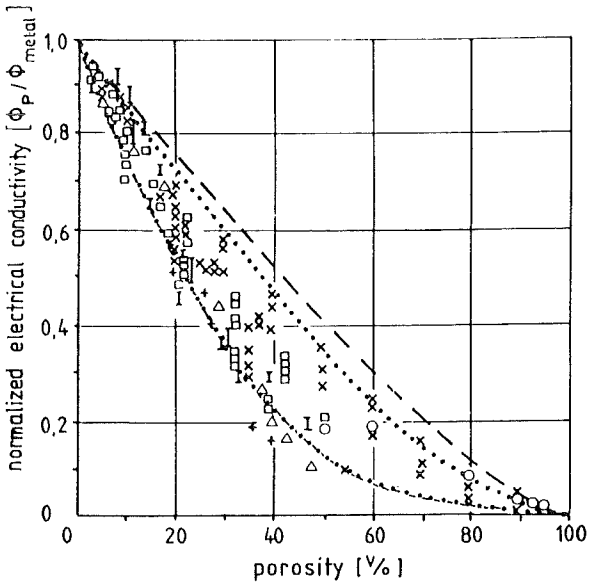

Fig. 103: Electrical conductivity of isotropic porous sintered metals as bronze (+) [99], Cu (I) [140,237,256], Fe/steel (□) [140,157,168,215], Mo (o) [48], Ni (Δ) [100], W (x) [84] at room temperature and II. order bounds (---) as well as III. order bounds (····).

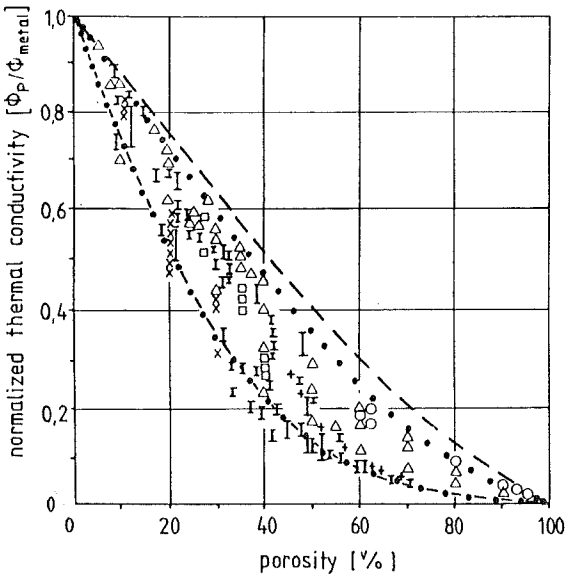

Fig. 104: Thermal conductivity of isotropic porous sintered metals as Fe/steel (I) [4,33,121,140,141,168,276], Cu (x) [140], Mo (o) [10,49], W (Δ) [84,147,162,165], Ni (□) [168], Be (+) [48] at room temperature and II. order bounds (---) as well as III. order bounds (····).

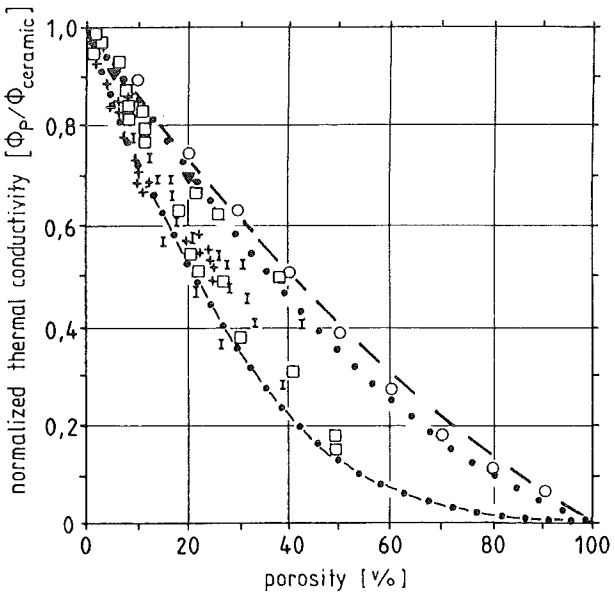

Fig. 105: Thermal conductivity of isotropic porous sintered ceramics as Al_2O_3 (□) [172,235], ZrO_2 (o) [16], B_4C (+) 119,167], TiN (∇) [3] and various minerals (I) [251] at room temperature and II. order bounds (---) as well as III. order bounds (·····).

known, one may calculate singular values and compare them with measured data. This is done in figs. 110 and 111 for sintered porous iron. The calculation was based for both fig. 110 (isotropic sintered porous iron; $\cos^2\alpha_1 = 0.33$) and fig. 111 (non-isotropic sintered porous iron) on equ. (44). It is noteworthy, that all shape factors of the pores in sintered iron in fig. 110 and 111 refer to those axial ratios (≥ 0.1) according to fig. 13, which, for industrially sintered materials, have been predicted before.

Finally measured values of multiphase materials have been compared with theoretical data calculated as described in chapter 2.8

In fig. 112 measured thermal conductivities for fire-resistant bricks (multiphase ceramic) are related to curves, which have been calculated referring to the schematic sketch (fig. 112). For the alumina based and quartz based bricks consisting of single-phase alumina and quartz with microporosity as an "effective" matrix phase, in which, then, macroporosity is included, the thermal conductivities for the microporous alumina and microporous quartz have been

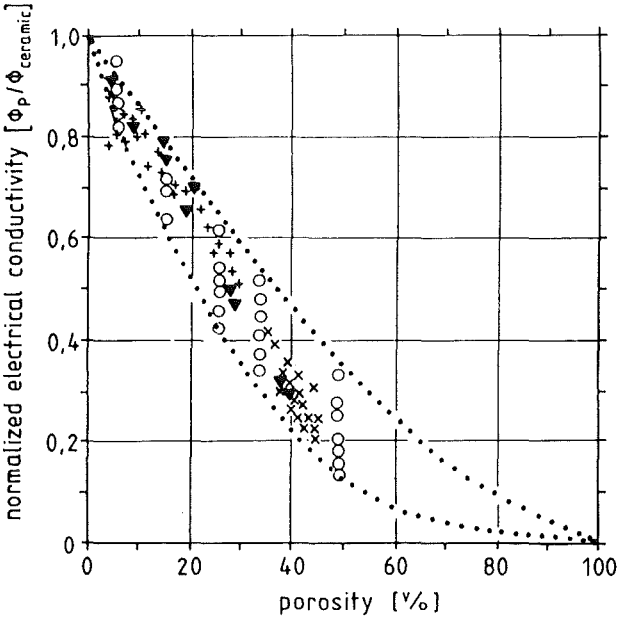

Fig. 106: Electrical conductivity of isotropic porous sintered ceramics as ZrO_2 (o) [234], TiC (+) [236], Ca_xMo_yC (x) [218], TiN (▼) [3] at room temperature and III. order bounds (····).

calculated in a first step followed by calculating the (macro-) porosity influence in a second step. The calculation was based on equ. (32) and (36) and concerns, in this case, three phase materials: a single-phase ceramic, microporosity and macroporosity, the latter one being either closed (in quartz based bricks) or interconnected (in corund-based bricks). Since in the silica-based fire resistant ceramic the silica solid constituent itself is already three-phased composed by cristobalite (50 Vol.%), tridymite (36 Vol.%) and glassy phase (14 Vol.%) the system with microporosity and macroporosity is five-phased in total. But, as fig. 112 brings out, also for this complex ceramic as well as for the two three-phase brick materials satisfying agreement exists between the calculated overall thermal conductivities versus macroporosity and the measured data.

The same result has been obtained by the same procedure for non-porous three-phase ZrO_2-based ceramic and non-porous three-phase polymer-metal-composites with polymer matrix phase (fig. 113) as well as for porous glass-iron cermets (fig. 114). Even for microstructurally complex four-phase "gas concrete" [21] and five-phase mining materials [75] promising results are reported in the literature. - This is why, summarizing, the following conclusions may be drawn:

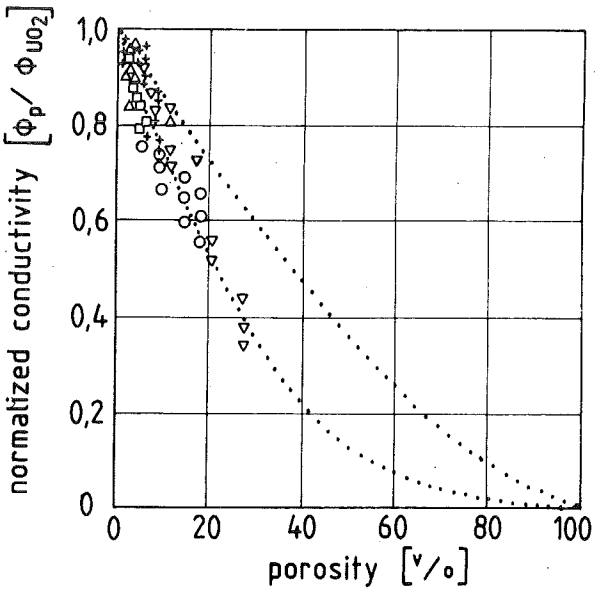

Fig. 107: Electrical and thermal conductivity of isotropic porous UO_2 nuclear ceramic (o) [13], (∇ +) [360,98], (□) [173], (Δ) [266] at room temperature and III. order bounds (····).

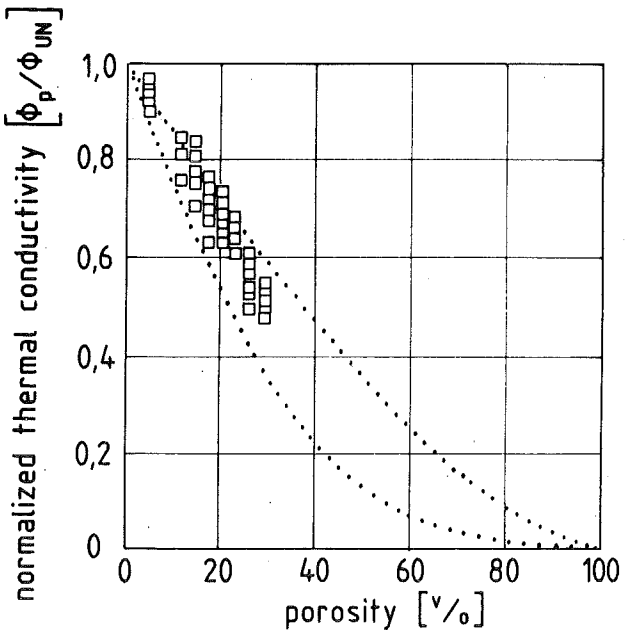

Fig. 108: Thermal conductivity of isotropic porous UN nuclear ceramic (□) at room temperature [135] and III. order bounds (····).

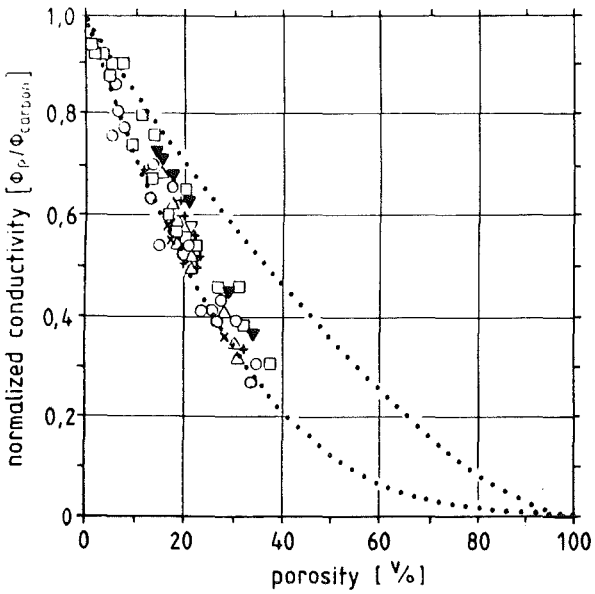

Fig. 109: Thermal ([] o Δ + x) and electrical conductivity (∇) of isotropic porous carbon and grafite at room temperature [39,117,170,228,269] and III. order bounds (····).

4.7 Conclusions

Microstructure-field property correlations open a better scientific insight into multi-phase materials behaviour including even phase bonding studies holding true for all types of multi-phase materials (e.g. metals, ceramics, carbon, polymers and composites) including porous materials and all field properties (e.g. electrical and thermal conductivities, dielectric constants, magnetic permeabilities).

They are reliable and may be used as an engineering tool to predict desired properties by precalculated microstructures in order to construct taylor-made materials as for example to satisfy the increasing technical demands towards engineering materials as well as economical and ecological expectations by substituting rare and biosuspicious components without quality losses. Thus direct property measurements may be substituted by quantitative microstructural analysis, where these property measurements are difficult, inaccurate, expensive or even impossible as under certain conditions (e.g. high temperature, irradiation) and quality control may be extended by field property data calculated via microstructure field property equations.

Porosity [%]	Shape factor (F_P)	normalized electrical conductivity (ϕ_P/ϕ_{Fe})	
		measured	calculated
0	-	1.0 ($\doteq 8.7 \cdot 10^6\ \Omega^{-1}m^{-1}$)	1.0 ($\doteq 8.7 \cdot 10^6\ \Omega^{-1}m^{-1}$)
3.7	0.225	0.97	0.94
3.9	0.219	0.94	0.93
3.9	0.208	0.96	0.93
4.3	0.240	0.97	0.93
4.5	0.190	0.93	0.93
4.8	0.185	0.97	0.92
5.1	0.137	0.87	0.90
5.3	0.174	0.88	0.91
5.3	0.232	0.94	0.93
5.4	0.246	0.97	0.95
5.5	0.200	0.97	0.91
5.6	0.153	0.92	0.90
5.5	0.150	0.93	0.90
5.6	0.169	0.97	0.91
5.8	0.165	0.93	0.90
5.8	0.180	0.91	0.90
5.9	0.169	0.97	0.90
6.0	0.170	0.97	0.90
6.0	0.148	0.91	0.89
6.1	0.173	0.91	0.90
6.2	0.160	0.94	0.89
6.2	0.298	0.93	0.93
6.2	0.303	0.97	0.97
6.6	0.187	0.95	0.89
6.7	0.140	0.93	0.87
6.8	0.160	0.87	0.88
7.1	0.311	0.97	0.97
7.2	0.181	0.87	0.88
7.8	0.192	0.86	0.87

Fig. 110: Measured and calculated electrical conductivities of isotropic ($\cos^2\alpha_P = 0.33$) sintered iron with different porosity and pore shape at room temperature [215].

Porosity P [%]	Shape factor F_P	Orientation factor $\cos^2\alpha_P$	normalized electrical conductivity (ϕ_P/ϕ_{Fe})	
			measured	calculated
0	-	-	1.0 ($\doteq 8.7 \cdot 10^6$ $\Omega^{-1}m^{-1}$)	1.0 ($\doteq 8.7 \cdot 10^6$ $\Omega^{-1}m^{-1}$)
2.61	0.177	0.10 0.13 0.77	0.83 0.83 0.83	0.97 0.96 0.94
7.14	0.177	0.25 0.29 0.46	0.86 0.86 0.85	0.89 0.88 0.86
10.7	0.165	0.20 0.38 0.42	0.79 0.78 0.76	0.84 0.81 0.80
14.5	0.153	0.10 0.28 0.62	0.70 0.67 0.60	0.81 0.76 0.68

Fig. 111: Measured and calculated electrical conductivities of porous sintered iron with different porosity, pore shape and orientation at room temperature [215].

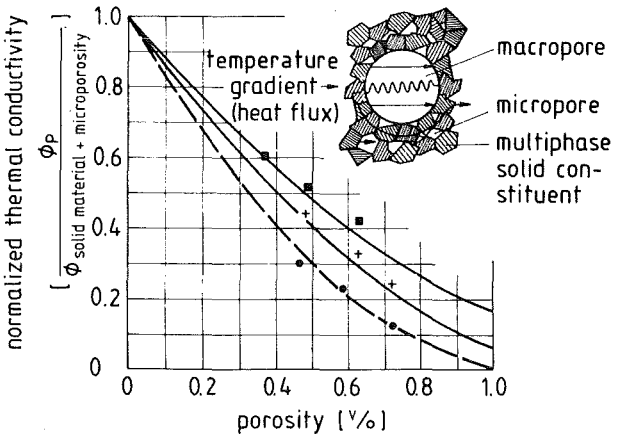

Fig. 112: Thermal conductivity of quartz (two-phased) with airfilled (macro-) porosity (▮), corund (two-phased) with airfilled (macro-) porosity (●) and silica (four-phased: cristobalite + trydymite + glassy phase + microporosity) with airfilled (macro-) porosity (+) at 873 K [187] and calculated curves (— closed porosity; --- interconnected porosity).

Since field properties cover just one type of property, microstructure-property relationships are now under investigation with respect to the elastic and complex technical behaviour of materials [205].

Phases	phase concentration [vol.%]	effective thermal conductivity [$Wm^{-1}K^{-1}$]	
		measured	calculated
silicon rubber Al Ni	90 6 4	0.559	0.525
silicon rubber Al Ni	78 13 9	0.804	0.802
silicon rubber Al Bi	88 4 8	0.637	0.542
silicon rubber Al Bi	82 15 3	0.770	0.682
silicon rubber Bi Pb	88 4 8	0.592	0.547
silicon rubber Bi Pb	82 10 8	0.692	0.652
MgO-stabilized ZrO_2:			
ZrO2 monoclinic inclusions monoclinic matrix phase	55 27 18	0.75 - 0.77	0.77
ZrO2 monoclinic inclusions monoclinic matrix phase	35 25 40	0.91 - 0.93	0.93
ZrO2 monoclinic inclusions monoclinic matrix phase	20 25 55	1.02 - 1.05	1.07

Fig. 113: Measured and calculated thermal conductivity of isotropic three phase composites [21,53] and magnesia stabilized ceramic [21,47] at room temperature.

porosity [%]	glass content [vol.%]	porosity related to iron [%]	eff. electrical conductivity of porous iron [ϕ_P/ϕ_{Fe}]	effective electrical conductivity of porous iron with glass [ϕ_P/ϕ_{Fe}]	
				measured	calculated
0	0	0	1 ($\doteq 8.7 \cdot 10^6\ \Omega^{-1}m^{-1}$)	1	1
8.9	-	8.9	0.87	0.68	0.87
16.66	8.33	18.2	0.74	0.54	0.65
20.35	7.96	22.1	0.69	0.55	0.61
11.38	8.86	12.5	0.82	0.64	0.71
14.75	8.52	16.1	0.77	0.68	0.67
14.48	8.55	15.8	0.77	0.59	0.67
15.43	8.45	16.8	0.76	0.55	0.67
12.94	17.41	15.7	0.77	0.48	0.58
14.7	25.59	19.8	0.72	0.48	0.46

Fig. 114: Measured and calculated electrical conductivity of isotropic ($F_P \approx F_{glass} \approx 0.33$; $\cos^2\alpha_P \approx \cos^2\alpha_{glass} \approx 0.33$) (three phase) porous glass-iron cermets at room temperature.

5. References

[1] Abeles B., Gittleman J.J., Appl. Opt. 15 (1976) 2328

[2] Aharoni S.M., J. Appl. Phys. 43 (1972) 2463

[3] Aivazov M.I., Domshnev I.A., Sov. Powder Met. Metal. Ceram. 7 (1968) 708

[4] Aksenov G.I., Zabbarov R., Sov. Powder Met. Metal. Ceram. 54-6 (1967) 458

[5] Allev N.A., Trudy Inst. Fiz. i. Mat., Akad. Nauk. Azerbeidzhan SSR, Ser. Fiz 8 (1956) 101

[6] Amato J., Colombo R.L., Polin F., Rev. Hautes Temper. et Refract. t3 (1966) 189

[7] Amman E., Hinnüber G., Z. Eisenhüttenwesen 71-21 (1951) 1081

[8] Andrea D., Ling Thesis, Renss. Polytechn. Inst. Troy, N.Y. (1969)

[9] Andreeva, N.G., Mekhanika Polimerov 2 (1973) 259

[10] Anishenko L.M., Brekhovskikh V.F., Sov. Powder Met. Metal. Ceram. 13 (1974) 298

[11] Araujo De F.F.T., Rosenberg H.M., J. Phys. D: Appl. Phys. 9 (1976) 665

[12] Arthur G., Coulson J.A., J. Nucl. Mat. 13 (1964) 242

[13] Asamoto R.R., Anselin F.L., Conti A.E., J. Nucl. Mat. 29 (1969) 67

[14] Avgustinik A.J., Gandelsman I.L., Gorfunkel L.F., Zhurnal Prikladnoi Khimii 40 (1967) 2566

[15] Bahr U., Diener G., Schöpf H.G., Wiss Z. der TU Dresden 23-2 (1974) 319

[16] Bahunov V.S., Balkevich V.L., Vlasov A.S., Guzman I.Y., Lukin E.S. Pouboyarinov D.N., Moscow. Metall. 2 (1977) 232

[17] Bast U., Dissertation Technische Fakultät, Universität Erlangen (1986)

[18] Beckermann M., Thun R.E., Transact. 8th Vacuum Symp. (1961) 905

[19] Beer A., Einleitung in die höhere Optik, S. 35, Verlag Vieweg & Sohn, Braunschweig 1853

[20] Behrens E., J. Comp. Mat. 2 (1968) 1

[21] Beie H.J., Dissertation Technische Fakultät, Universität Erlangen (1986)

[22] Belle J., "Uraniumdioxide" US AEC Naval Reactors (1961)

[23] Belskaya E.A., Tarabanov A.S., J. Eng. Phys. 20-4 (1970) 472

[24] Beran M., Molyneux J., Q. Appl. Math. 24 (1966) 107

[25] Beran M.J., in J.W. Provan, H.H.E. Leipholz, Continuum Models of discrete systems, University of Waterloo Press, 2 (1978) 217

[26] Bergmann D.J., Phys. Rep. 43 (1978) 377

[27] Bergmann D.J., J. Phys. C12 (1979) 4947

[28] Bergmann D.J., Phys. Rev. Lett. 44 (1980) 1285

[29] Bergmann W., Frommeyer G., Z. Metallkde 68 (1977) 590

[30] Behrens E., J. Comp. Mat. 2 (1968) 1

[31] Bevington R.C., Kim H.J., IEEE Trans. on Comp., Hybrids and Manufact. Techn., CHMT 2-1 (1979) 46

[32] Bhattacharyya S.K., Basu S., De S.K., pal A.D., Chowdhury S., J. Appl. Phys. 49 (1978) 3001

[33] Biceroglu L., Mujumdar N., Heinigen N. van, Douglas C., Int. J. Heat and Mass Transfer 3 (1976) 183

[34] Bielska-Lewandowska H., Acta Physica Polonica A 39 Fasc. 6 (1971) 687

[35] Blakeley T.H., White A.E.S., in F. Benesovsky, Proc. 2nd Plansee-Seminar, Springer-Verlag Wien (1956) 335.

[36] Blum G., Elektrie 13 (1959) 201

[37] Bocchini G.F., Reviews on Powder Metallurgy and Physical Ceramics 2-4 (1985) 313

[38] Böttcher C.J.F., Rev. trav. chim. 64 (1945) 47

[39] Brocklehurst E., Brown R.G., Gilchrist K.E., Labaton V.Y., J. Nucl. Mat. 35-2 (1970) 183

[40] Bronstein J., Semendjajew K., Taschenbuch der Mathematik, Teubner Verlagsgesellschaft Leipzig (1963) 110

[41] Brown W.F., J. Chem. Phys. 23 (1958) Nr. 8, 1514

[42] Bruggeman D.A.G., Ann. Phys. 24 (1935) 636

[43] Bruggeman D.A.G., Ann. Phys. 25 (1936) 645

[44] Budiansky B., J. Comp. Mater. 4 (1970) 286-295

[45] Bueche F., J. Appl. Phys. 44-1 (1973) 532

[46] Burger H.C., Phys. Z. 20 (1919) 73; 22 (1921) 28

[47] Buykx W.J., Swain M.V., Advances in Ceramics Vol. 12, Science and Technology of Zirconia II (1984) 518-527

[48] Bykovskii V.F., Dubinin R.M., Nichkov C.V., Sov. Atomic Energy 45 (1978) 793

[49] Chaparova I.N., Chruyavski R., Agababova S.T., Vsova U.S., Nachn. Trudy Vses. Nauch. Issled. Proekt. Inst. 13 (1973) 50

[50] Chaurasia P.B.L., Chaudhary D.R., Bhandari R:C., Indian J. Pure Appl. Phys. 16 (1978) 963-967

[51] Chaurasia P.B.L., Indian J. Pure Appl. Phys.20 (1982) 145-147

[52] Cheng S.C., Vachon R.I., Int. J. Heat Mass Transfer 12 (1969) 249-264

[53] Cheng S.C., Law Y.S., Kwan C.C.Y., Int. J. Heat Mass Transfer 15 (1972) 355-358

[54] Chiew Y.C., Glandt E.D., J. Colloid Interface Sci. 94 (1983) 90-104

[55] Chistov S.F., Belyaev A.A., Burtsev Y.N., Zavadskaya Laboratoriya 38 (1972) 954

[56] Clark H., Trans. Am. Geophys. Union 3 (1941) 543

[57] Clausius R., Die mechanische Wärmetheorie, Bd. 11. S. 62. Verlag F. Vieweg & Sohn, Braunschweig (1879)

[58] Cohen M.H., Jortner J., Webmann J., AIP COnf. Proc. 40 (1977) 63

[59] Colletti W., Rebori L., Insulation 27 (1965)

[60] Craeynest J.C. van, Stora J.P., J. Nucl. Mat. 37 (1970) 153

[61] Crane R.A., Vachon R.I., Int. J. Heat Mass Transfer 20 (1977) 711-723

[62] Cunningham G.W., Kizer D.E., Paprocki S.J., in F. Benesovsky (ed.), 4th Plansee Seminar, Springer-Verlag Wien (1962) 483

[63] Danilenko V.A., Zyrin A.V., Sov. Powder Met. and Met. Ceram. 50 (1966) 44

[64] Das D., Basu S., Paul A., J. Mat. Sci. 15 (1980) 1719

[65] Davies H.T., Valencourt L.R., Johnson C.E., J. Am. Ceram. Soc. 58 (1975) 446

[66] Dawson D.M., Briggs A., J. Mater. Sci. 16 (1981) 3346-3356

[67] Degussa-Firmenschrift, Liste K 110 (1961) 14

[68] Diener G., Weissbarth J., in O. Brulin, R.K.T. Hsieh, Continuum models of discrete systems, North Holland Publ. Co. Amsterdam-New York-Oxford 4 (1981) 349

[69] Doebke W., Z. Techn. Phys. 11 (1930) 12

[70] Donea J., J. Comp. Mater 6 (1972) 262-266

[71] Dörre E., Ziegele W., Ber. DKG 47 (1970) 622

[72] Doyle W.T., AIP Conf. Proc. 40 (1977) 300

[73] Dulnev G.N., Zarichnyak Y.P., Machavariani E.S., Teplofizika Vysoki Temperatura II-4 (1973) 887

[74] Dürrwächter KG, "Elektrische Kontakte aus Sinterwerkstoffen", Firmenschrift, 5.12 (1956) 14

[75] Ebel B., Jeulin D., Ondracek G., Proc. MRS-Europe (1985) 187

[76] Eisenkolb F., Richter W., Wiss. Z. TH Dresden 3 (1953/54) 71

[77] Eisenkolb F., Schatt W., Neue Hütte 2 (1957) 471

[78] El-Fekey S.A., El-Manoan Jehia M., El-Hakim M.N.A., Powder Met. Int. 10-2 (1978) 90

[79] Eucken A., VDI Forschungsheft 353B, Bd. 3 (1932)

[80] Farnham F.R., Iron Age Nov. (1954)

[81] Feldtkeller E., Dielektrische und magnetische Materialeigenschaften I BI-Hochschultaschenbuch, Band 485, Mannheim 1973

[82] Fischer W.A., Pieper C., Arch. Eisenhüttenwesen 44 (1973) 483

[83] Francl J., Kingergy W.D., J. Amer. Ceram. Soc. 37 (1954) 99

[84] Francois D., Terraz C., Mayer R., Pastor H., Planseeber. 20 (1972) 185

[85] Frey G.S., Z. Elektrochemie 38 (1932) 260

[86] Fricke H., Phys. Rev. 24 (1931) 575

[87] Fugitsu M., Hasatani M., Sugiyama S., J. Chem. Eng. Japan 10 (1977) 242

[88] Gaal I., Proc. VII. Int. Pulvermet. Tagung Dresden, Bd. 2 (1985) 15

[89] Gaisnayuk N., Phys. Stat. Solidi 48 (1978) K 131

[90] Garett K.W., Rosenberg H.M., J. Phys. D: Appl. Phys. 7 (1974) 1247

[91] Garett K.W., Rosenberg H.M., J. of Physics D: Appl. Phys. 8 (1975) 1882

[92] Gebhardt E., Ondracek G., Thümmler, J. Nucl. Mat. 13 (1964) 229

[93] Gibby H., Lawrence G., Proc. Am. Ceram. Soc. winter meeting (1971)

[94] Gibson-Electric Seales Corp. TB 5064- (62)

[95] Giuliani S., Mustacchi C., Amato I., Colombo R.L., Coselli R., Rev. Int. Hautes Temper. et Refract. t4 (1967) 77

[96] Gladstone J.H., Dale T.P., Phil. Trans. London 153 (1863) 317

[97] Goetzel C.G., Treatise on Powder Metallurgy, Interscience Publ., New York, Vol. II (1950) 216

[98] Goldsmith L.A., Douglas J.A.M., J. Nucl. Mat. 47 (1973) 31

[99] Grootenhuis S., Powell N.T., Tye M.A., Proc. of the Phys. Soc. 65 (1952) 502

[100] Grube N., Schlecht R., Z. Elektrochemie 44 (1938) 367

[101] Gurland J., in F. Benesovsky (ed.), 4th Plansee-Seminar, Springer-Verlag, Wien (1962) 507

[102] Hamilton R.L., Dissertation, University of Oklahoma, 1960

[103] Hamilton R.L., Crosser O.K., Ind. Eng. Chem. Fund. 1 (1962) 187-191

[104] Hansen D., Tomkiewicz R., Polymer Eng. and Sci. 15 (1975) 353

[105] Hashin Z., Shtrikman S., J. Appl. Phys. 33 (1962) 3125

[106] Hattori M., Tanaka M., Kamiike E., Oyo butsuri 34 (1965) 356

[107] Hausner H.H., Powder Met. Bull. 3 (1948) 4

[108] Hayashi K., Fukui M., Uei I., Yogyo-Kyohai-Shi 82 (1974) 21, 202

[109] Hayashi K., Uei I., Yogyo-Kyohai-Shi 82/7 (1974) 382/40

[110] Hayashi K., Kasai J., Fukui M., Nishikawa T., Yogyo-Kyohai-Shi 86-3 (1978) 115

[111] Hengst G., Dissertation TH München (1934)

[112] Herring C., J. Appl. Phys. 31 (1960) 1939

[113] Higuchi W.I., J. Phys. Chem. 62 (1958) 649

[114] Hoff R.T. De, Rhines F.N., Trans. Met. Soc. AIME 221 (1961) 975

[115] Holzmann H., Metall 12 (1958) 630

[116] Huang J.H., J. Geophys. Res. 76-26 (1971) 6420

[117] Hutcheon J.M., Price M.S.T., Proc. 4th Conf on Carbon, Pergoman New York (1960)

[118] Igarashi H., Okazaki K., J. Am. Ceram. Soc. 60-1/2 (1977) 51

[119] Iseki T., Ito M., Suzuki H., Honda T., J. Nucl. Sci. Technol. 10-6 (1973) 360

[120] Ivan J., Sebo P., Taborsky L., Havalda A., Kovove Materialy 3-XI (1973) 228

[121] Januszewski C., Khokar L., Mujumdar N., Int. J. Heat and Mass Transfer 4 (1977) 417

[122] Jefferson T.B., Witzell O.W., Sibbit O.W., Ind. Eng. Chem. 50 (1958) 1589-1592

[123] Jellinghaus W., Forschungsbericht des Landes Nordrhein-Westfalen Nr. 1015, Westdeutscher Verlag, Köln-Opladen (1961)

[124] Jesse A., Dissertation, Universität Karlsruhe, Fakultät Maschinenbau (1970)

[125] Jones T.J., Street K.N., Scoberg J.A., Baird J., Canadium Metallurgical Quarterly Vol. 2, Nr. 1 (1963)

[126] Joos G., Lehrbuch der theoretischen Physik, Akad. Verlagsges. Frankfurt (1959) 262

[127] Kainer K.U., Dissertation TU Clausthal, Fakultät für Bergbau, Hüttenwesen und Maschinenwesen (1985)

[128] Kane M., MND-SF-1770 (1973) 58

[129] Karpinos D.M., Klimenko V.S., Kadyrov V.H., High Temp.-High Pressure 5 (1973) 13

[130] Keil A., Werkstoffe f. elektrische Kontakte, Springer-Verlag, Berlin-Stuttgart-Heidelberg (1960) 186

[131] Kerner E.H., Proc. Phys. Soc. 69B (1956) 802

[132] Kharadly M.M.Z., Jackson W., Proc. Inst. Electron. Engng. 100 (1953) 199

[133] Kharitonov E.V., Khanin S.D., Sov. Phys. Semicond. 11-2 (1977) 240

[134] Kieffer R., Hotop W., Pulvermetallurgie und Sinterwerkstoffe, Springerverlag Berlin-Göttingen-Heidelberg (1943) 324

[135] Kikuchi T., Takahashi T., Nasu S., J. Nucl. Mat. 45 (1972/73) 284

[136] Kingery W.D., J. Am. Ceram. Soc. 42-12 (1969) 617

[137] Kirkpatrick S., Rev. Mod. Phys. 45 (1973) 574-588

[138] Kline D.E., J. Polymer Sci. L (1961) 441

[139] Knappe W., Ott H.-H., Wagner G., Kunststoffe 68 (1978) 426-429

[140] Koh J.C., Fortini A., Int. J. Heat and Mass Transfer 16 (1973) 2013

[141] Kononenko V.I., Baranovski V.M., Dushecheniko V.P., Sov. Powder Met. Metall. Ceram. 63-3 (1968) 175

[142] Kostornov A.G., Shevchuk M.S., Lezehin F.F., Fedorchenko I.M., Sov. Powder Met. and Ceram. 169 (1977) 383

[143] Krischer O., Kast W., Die wissenschaftlichen Grundlagen der Trockungstechnik, Springer Verlag Berlin-Heidelberg-New York (1978) 100

[144] Kröner E., Koch H., SM Archives 1-2/3 (1976) 183

[145] Kröner E., J. Mech. Phys. Solids 25 (1977) 137

[146] Kröner E., J. Phys. F.: Metal Phys. 8-11 (1978) 2261

[147] Kulcinski R., Wagner P., J. Less Common Met. 6 (1964) 383

[148] Kusy R.P., Corneliussen R.D., Polymer Eng. and Sci. 15-2 (1975) 107

[149] Landau L.D., Livsic I.M., in I.M. Fedortschenko, P.A. Andrievski, Osnowie Poroschkowoi Metallurgy. Isd. Akad. Nauk USSR 1961

[150] Landauer R., J. Appl. Phys. 23-7 (1952) 779

[151] Landauer R., J. Appl. Phys. 33 (1962) 779

[152] Landauer R., AIP Conf. Proc. 40 (1977) 2

[153] Landolt H., Pogg. Ann. 123 (1864) 595

[154] Landolt-Börnstein, Zahlenwerte und Funktionen aus Naturwissenschaft und Technik, Springer Verlag, Berlin-Heidelberg-New York, Bd. IV-2a (1963) 234

[155] Lauchon H., Mirgaux A., Cioranescu D., Saint Jean Paulin J., Bourgat J., in O. Brulin, R.K.T. Shieh, Continuum models of discrete systems, North Holland Publ. Co., Amsterdam-New York-Oxford 4 (1981) 75

[156] Lee H.J., Tylor R.E., J. Appl. Phys. 47 (1976) 148

[157] Leheup E.R., Moon J.R., Powder Metall. 21 (1978) 1

[158] Lezhenin F.F., Shurgay I.N., Kostornov A.G., Shevchuk M.S., Heat Transfer 9 (1977) 144

[159] Lichtenecker K., Phys. Z. 27 (1926) 115 and 833

[160] Lichtenecker K., Rother K., Phys. Z. (1931) 255

[161] Loeb A.L., J. Am. Ceram. Soc. 37 (1954) 96

[162] Logunov A.V., Chevela O.B., Silaev A.F., Sov. Powder Met. Metal. Ceram. 13 (1974) 304

[163] Lorenz L., Wied. Ann. II (1869) 70

[164] Lorentz H.A., Wied. Ann. 9 (1880) 641

[165] Lvov S.N., Malko P.I., Nevskaya L.V., Nemchenko V.F., Sov. Powder Met. Metal. Ceram. 41-5 (1966) 416

[166] Magomedov A.M.A., Ismailov M.A., Pashaev B.P., Teplofizika Vysokich Temperatura 13-5 (1975) 1106

[167] Mahagin D.E., Baker D.E., Bates J.L., Am. Ceram. Soc. Bull. 52-9 (1973) 718

[168] Malko P.I., Nemchenko V.F., Lvov S.N., Pugin V.S., Sov. Powder Met. and Met. Ceram. 73 (1969) 49

[169] Malliarias A., Turner D.T., J. Appl. Phys. 42 (1971) 614

[170] Matsuo H., J. Nucl. Mat. 89-1 (1980) 9

[171] Maxwell J.C., Treatise on Electricity and Magnetism, Oxford Vol. I (1904) 435

[172] McClelland J.D., Petersen L.O., USAEC-NAA-SR-6473 (1961) 9

[173] McEwan J.R., Stonte R.L., Notley M.I.F., J. Nucl. Mat. 24 (1967) 109

[174] McKenzie D.R., McPhedran R.C., Derrick G.H., Proc. Royal Soc. London A362 (1978) 211

[175] McPhedran R.C., McKenzie D.R., Proc. Royal Soc. London A359 (1978) 45

[176] Meny L., Buffet J., Sauve C., in F. Benesovsky (ed.), 4th Plansee Seminar, Springer-Verlag, Wien (1962) 566

[177] Meredith R.E., Tobias C.W., J. Appl. Phys. 31 (1960), 1270 (UCRL-8667)

[178] Meredith R.E., Tobias C.W., J. Electrochem. Soc. 108 (1961) 286

[179] Milgram A.A., Chih-Shu Lu, J. Appl. Phys. 39 (1968) 4219

[180] Miller J.V., NASA-TN-D-3898, 1967

[181] Milton G.W., Appl. Phys. Lett. 37 (1980) 300

[182] Milton G.W., J. Appl. Phys. 52-8 (1981) 5296, 5294

[183] Mosotti O.F., Mem. de mathem. et di fisica della società italiana delle science residente in Modena 24 II (1850) 49

[184] Murabayashi M., Takahashi Y., Nasu J., J. Nucl. Science and Techn. 6 (1969) 47

[185] Neale G.H., Nader W.K., AIChE Journal 19 (1973) 112-119

[186] Nedoluha A., Z. Phys. 148 (1957) 248

[187] Neuenburg M., Dissertation, TU Clausthal, Fakultät für Bergbau, Hüttenwesen und Maschinenwesen (1984)

[188] Niesel W., Ann. Phys. 6-10 (1952) 336

[189] Nikolopoulos P., Ondracek G., J. Am. Ceram. Soc. 66-4 (1983) 238

[190] Nikolopoulos P., Ondracek G., Z. Metallkde 74 (1983) 49

[191] Odelewsky W.I., J. Techn. Fis. (USSR) 21 (1951) Nr. 6

[192] Oelmonte J., Metal filled plastics, Reinhold Publ. Co. New York (1961)

[193] Ollendorf F., Arch. Elektrotechnik 25 (1931) 436

[194] Ondracek G., in Science in Ceramics Vol. 6 (1973) III/1 und Bericht des Kernforschungszentrums Karlsruhe KfK Ext. 6/73-2 (1973) 40

[195] Ondracek G., Z. Werkstofftechnik 5-8 (1974) 416

[196] Ondracek G., Z. Werkstofftechnik 8 (1977) 220, 280

[197] Ondracek G., VII. Int. Pulvermet. Tagung, Dresden Bd. 2 (1981) 241

[198] Ondracek G., Metall 36-5 (1982) 523

[199] Ondracek G., Metall 36-12 (1982) 1288

[200] Ondracek G., Acta Stereologica 1-1 (1982) 5

[201] Ondracek G., Metall 37-10 (1983) 1016

[202] Ondracek G., Umschau 7 (1985) 400

[203] Ondracek G., VIII. Int. Pulvermet. Tagung, Dresden Bd. 2 (1985) 191

[204] Ondracek G., Z. Metallkde. 77-9 (1986) 603

[205] Ondracek G., Materials Physics and Chemistry 15 (1986) 281

[206] Ondracek G., Werkstoffkunde - Leitfaden für Studium und Praxis, expert-Verlag Sindelfingen 2. Auflage (1986)

[207] Ondracek G., Patrassi E., Ber. DKG 45 (1968) 617

[208] Ondracek G., Schulz B., Ber. DKG 48-10 (1971) 427, 525

[209] Ondracek G., Schulz B., in J.W. Provan, H.H.E. Leipholz "Continuum Models of Discrete Systems" SM-Study Nr. 12 University of Waterloo Press (1978) 223

[210] Ondracek G., Schulz B., in E. Kröner, K.H. Anthony, H.H.E. Leipholz "Continuum Models of Discrete Systems" SM-Study Nr. 15 University of Waterloo Press (1980) 499

[211] Ondracek G., Schulz B., Thümmler F., High Temp.-High Press. 1 (1969) 439

[212] Ostrander W.J., Lewis C.W., Trans. 8th Nat. Vacuum Symp. Vol. 2 (1961) 881

[213] Ott H.J., Plastics and Rubber Proc. and Appl. 1 (1981) 9

[214] Pearce C.A.R., British J. of Appl. Phys. 6 (1955) 113

[215] Pejsa R., Dissertation, Universität Karlsruhe, Fakultät Maschinenbau (1981)

[216] Perrins W.T., McKenzie D.R., McPhedran R.C., Proc. Royal Soc. London A369 (1979) 207

[217] Peterson J.M., Hermans J.J., J. Comp. Mat. 3 (1969) 338

[218] Petrova E.M., Tekhuol. Poluch. Novykh. Mater. 24 (1973) 30

[219] Pohl R.W., Elektrizitätslehre, Springer-Verlag Berlin-Göttingen-Heidelberg (1964) 156

[220] Poisson S.D., Mem. Acad. Roy. Sc. Inst. France 5 (1826) 247 and 488

[221] Polder D., Sanden J.H. van, Phisica 12 (1946) 257

[222] Progelhof R.C., Throne J.L., Ruetsch R.R., Polym. Eng. Sci. 16 (1976) 615-625

[223] Provirin V.I., Savitskii A.I., Mekhanika Polimerov 2 (1971) 323

[224] Pustogarov A.V., Melniko G.N., Kolesnichenko A.N., Daragan V.D., Chepiga D.D., Poroshk. Metall. 13 (1974) 52

[225] Rajagopaö C., Satyam M., J. Appl. Phys. 49-11 (1978) 5536

[226] Raleigh J.W., Phil. Mag. 5-34 (1892) 481

[227] Ratcliffe E.H., Trans. Inst. Rubber Ind. 38 (1962) T181

[228] Rhee S.K., J. Am. Ceram. Soc. 55-11 (1972) 580

[229] Robertson E.C., Peck D.L., J. Geophys. Res. 79-32 (1974) 4875

[230] Ross S.K., AECL 1096 (1960)

[231] Rüdiger O., Winkelmann A., Techn. Mitt. Krupp 18-1 (1960) 19

[232] Runge J., Z. Techn. Phys. 5 (1925) 61

[233] Russel H.W., J. Am. Ceram. Soc. 18 (1935) 1

[234] Rutmann D.S., Maurin A.F., Taksis G.A., Torpov Y.S., J. Refract 6 (1970) 371

[235] Saegusa T., Iida Y., Wakao N., Kamata K., J. Heat Transfer 3-2 (1974) 47

[236] Samsonov G.V., Matsera V.E., SOv. Powder Met. Metal. Ceram. 11-9 (1972) 719

[237] Sauerwald F., Kubik J., Z. für Elektrochemie 38 (1932) 5

[238] Scarisbrick J., J. Phys. D: Appl. Phys. 6 (1973) 2098

[239] Schäfer A., Hieber K., Politycki A., Z. Metallkunde 63-11 (1972) 720

[240] Schmidt C., Cryogenics 15 (1975) 17

[241] Schmidt D., DFVLR-Forschungsbericht 69-96 (1969)

[242] Schreiner H., Pulvermetallurgie elektrischer Kontakte, Springer-Verlag Berlin-Göttingen-Heidelberg (1964) 122

[243] Schulz B., Bericht des Kernforschungszentrums Karlsruhe, KfK Ext. 6/74-4 (1974) 128

[244] Schulz B., Bericht des Kernforschungszentrums Karlsruhe, KfK 1988 (1974) 29ff

[245] Schulz B., High Temperatures-High Pressures 13 (1981) 649

[246] Schulz B., in T. Ashworth, D.R. Smith, Thermal Conductivity, Plenum Publ. Corp. New York (1985) 33

[247] Seith W., Schmeken H., in K. Ruthardt, Heraeus-Festschrift (1951) 218

[248] Silberstein L., Ann. Phys. u. Chem. N.F. 56 (1895) 661

[249] Stille U., Arch. Elektrotechnik 38-314 (1944) 91

[250] Stoltz D.L., Kizer D.E., Keller D.L., BMI 1619, Section D (1963) D1

[251] Sugawara A., Yoshizawa Y., J. Appl. Phys. 33-10 (1962) 3135

[252] Sundstrom D.W., Chen S.Y. J. Comp. Mat. 4 (1970) 113

[253] Sundstrom D.W., Lee Y.D., J. Appl. Polymer Sci. 16 (1972) 3159

[254] Sutherland W., Phil Mag. 27 (1889) Nr. 5, 27

[255] Swamy C.S., Weimar P., Powder Metall. Int. 2-4 (1970) 134

[256] Taubenblatt P.W., Int. J. Powder Met. 5 (1969) 89

[257] Taylor R., High Temperature-High Pressure 15 (1983) 299

[258] Thornburg J.D., Pears C.D., ASME Paper 65-WA/HT-4 (1965)

[259] Topper L., Ind. Engng. Chem. 47 (1955) 1377

[260] Torkar K., Chem.Ing.-Techn. 25 (1953) 308

[261] Transtel S., Panda J., Jacob P., Tonindustrie-Zeitung 85 (1961) 565

[262] Tsao G.T., Ind. Eng. Chem. 53 (1961) 395

[263] Turner J.C.R., Chem. Eng. Sci. 31 (1976) 487

[264] Tye R.P., McCauley J.W., Rev. Int. Htes. Temp. et Refract. 12 (1975) 100

[265] Underwood E.E., Quantitative Stereology, Addison-Wesley Publ. Co. Inc. Reading, Mass. (1970) 83

[266] Vogt J., Grandell L., Runfors U., AB Atomenergie (Sweden) Int. Rep. RMB-527 (1964)

[267] Vries D.A. de, Disseration Universität Leiden; Anhang 1952-1 an Bull. Inst. Int. Froid 1952, 115

[268] Wagner K.W., Arch. Elektronik 2 (1914) 371; 3 (1914) 100

[269] Wagner P., O'Rourke J.A., Armstrong P.E., J. Am. Ceram. Soc. 55-4 (1972) 214

[270] Wahl H.P., Wassermann G., Z. Metallkunde 61 (1970) 326

[271] Walpole L.J., in O. Brulin, R.K.T. Hsieh, Continuum models of discrete systems, North Holland Publ. Co. Amsterdam-New York-Oxford 4 (1981) 467

[272] Walter A.G., Trowell A.R., J. of Mat. Sci. 6 (1971) 1044

[273] Westphal W.H., Physikalisches Wörterbuch, Springer-Verlag Berlin-Göttingen-Heidelberg (1952) 351

[274] Wiener O., Abh. math.-phys. Kl. königl.-sächs. Ges. d. Wiss. 32-6 (1912) 509

[275] Woodside W., Messmer J.H., J. Appl. Phys. 32 (1961) 1688

[276] Zabbarov R., Inzh. Fiz. Zh. 13 (1967) 373

[277] Zehner P., Dissertation, TH Karlsruhe (1972)

[278] Zhorov G.A., Arabel B.G., Kozhukhov V.M., Roshchina I.N., Teplofizika Vysokihh Temperatur 14 (1976) 648

Acknowlegement

Prof. J. Grolier, who recently applied quantitative microstructure-property correlations in geology (compare Grolier J., Hucher M., Pouliquen J.M., Riss J., C.R. Acad Sci. Paris, t. 305 - II (1987) 1499) and Dr. Brigitte Schulz have given valuable comments. Prof. Waldron and Mr. Sippli thoroughly read the manuscript, which was typed and corrected by Mrs. Jutta Howell. The figures have been prepared by Mrs. Vera Karcher. The author gratefully appreciates this outstanding cooperation.